2015

Optimized Aperiodic Multilayer Structures for Absorbers and Thermal Emitters

Christopher H. Granier
Louisiana State University and Agricultural and Mechanical College

OPTIMIZED APERIODIC MULTILAYER STRUCTURES FOR ABSORBERS AND THERMAL EMITTERS

A Dissertation

Submitted to the Graduate Faculty of the
Louisiana State University and
Agricultural and Mechanical College
in partial fulfillment of the
requirements for the degree of
Doctor of Philosophy

in

The Department of Physics and Astronomy

by
Christopher H. Granier
M.S.,Louisiana State University, 2014
August 2015

Acknowledgments

I would like to express my gratitude to my co-advisors Dr. Jonathan P. Dowling and Dr. Georgios Veronis for their constant guidance and unwavering support throughout part of my undergraduate and my entire graduate-school career. Jon's enthusiasm, innovativeness, and imagination, all well-grounded in the principles of meaningful research and a deep understanding of physics and its applications allow him to generate interesting research topics which will undoubtedly lead to discoveries useful in everyday life. Dr. Veronis's painstakingly methodical approach to research coupled with his extreme attention to detail and countless hours of consultation were invaluable during my graduate career. Dr. Veronis provided his assistance and experience in debugging computer codes as well as his uncanny ability to anticipate and carefully craft counter arguments to would-be reviewers. Words cannot serve as a medium to adequately express my gratitude to both Jon and Dr. Veronis.

I would also like to thank Dr. Lee, who was always willing to help with any questions I might have had throughout my graduate career and Dr. Corbitt, who has provided an experimental insight into my work in nanophotonics.

Over the past five years, I have had the opportunity to work with two incredibly bright undergraduates. Francis Afzal assisted with some of the computational work associated with Chapter 2 and some of the work presented in Chapter 3 over the course of two summers spent at LSU as a REU student. Simón Lorenzo recently started working with us and has assisted in streamlining the computer codes as well as research associated with the Dual-Angle Absorber found in Chapter 3 and the lighhtbulb work in Chapter 4. I want to thank both of them for their contributions to the work as well as their friendship and support.

Special thanks to my peers, past and present, in the QST group, who provided helpful discussion and good company: Ashkan Balouchi, Bryan Gard, Manish Gupt, Kaushik Seshadreesan, Todd Moulder, Siddhartha Das, Bhaskar Roy Bardhan, Robinjeet Singh, Zhihao

Xiao, Kebei Jiang, Nick Lanning, and Jonny Olson. I would especially like to thank the person who will be moving forward with some of the work presented here and someone who has become a close friend, Chenglong You.

I also want to thank my entire family; each person has a special place in my life and has played a pivotal role in making me who I am today. Finally, and most importantly, I would like to thank my mother and grandmother, whose love and self-sacrifice have known no bounds over the past 28 years. Words cannot express my gratitude.

Table of Contents

Abstract

In this dissertation, we begin with a brief introduction to nanophotonics. In particular, we will focus on the theory of computational electricity and magnetism, specifically, the method used for this research, the transfer-matrix method. We will also provide discussions of the principles which motivate the analysis of the multilayer structures: Planck's blackbody distribution, Kirchoff's law, and thermodynamics. Finally, we will provide a brief discussion of computer-based optimization algorithms, specifically NLOPT (a library which provides computational packages for nonlinear optimization) and genetic algorithms. This background information is necessary to understand discussions which occur in later chapters.

Chapter 2 will discuss multilayer structures which are optimized by a genetic algorithm to provide both narrowband and narrow-angle thermal emission for selected wavelengths in the infrared wavelength range. This chapter will compare the performance of aperiodic multilayer structures with more widely researched periodic multilayer structures. It will also provide a detailed analysis of how this emission profile is achieved via an electromagnetic field analysis. Finally, Chapter 2 will present a concrete application for such optimized structures as a carbon monoxide detector via absorption spectroscopy.

Chapter 3 will focus on the development of aperiodic multilayer structures for use as narrow-angle absorbers. Both the layer thicknesses and materials used are optimized by a genetic optimization algorithm coupled to a transfer matrix code. We find that utilizing silicon and silica above a thick tungsten substrate provides a structure capable of near unity absorptance at a single wavelength. Finally we show that structures with almost perfect absorptance at multiple wavelengths for normally incident light can be achieved.

Chapter 4 presents optimized aperiodic structures for use as broadband, broad-angle thermal emitters. These structures are capable of increasing the thermal emittance by nearly a factor of two when compared to bulk tungsten. We utilize a hybrid optimization algorithm

coupled to a transfer matrix code to maximize the power emitted in the visible wavelength range in the normal direction. Chapter 4 also discusses the mechanisms present which allow these structures to possess properties, which could lead to a decrease in incandescent lightbulb power consumption by nearly 50%.

Chapter 1
Introduction and Theory

Photonic crystals are a widely known field of ongoing research which involves fabricating or simulating structures in one, two, or three dimensions for some specific use from solar thermophotovoltaics to antireflective coatings. Photonic crystals, by nature, exhibit periodicity; photonic nanostructures, however, do not. These nanostructures may be fabricated or computationally explored in one, two, or three dimensions and seek to affect the motion of photons in such a way that a specific use is achieved – high absorptivity, high reflectivity, angular selectivity, etcetera. Some of the most common applications kept in mind when designing these structures are: coherent emitters, solar themophotovoltaics, and filters. Research in these areas is done largely computationally. Electromagnetic codes implementing Transfer Matrix, FDFD (finite difference frequency domain), FDTD [1] (finite difference time domain), and plane wave expansion methods are among some of the most frequently used.

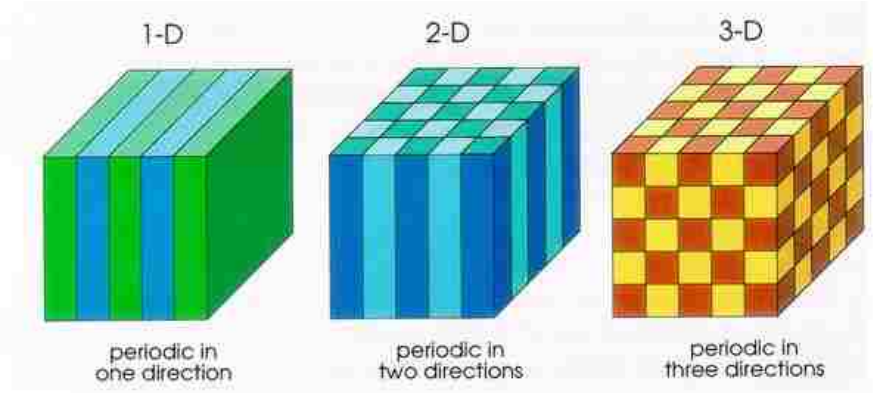

FIGURE 1.1: Schematic [2] of photonic crystals of one, two, and three dimensions. Figure 1.1 shows that a one dimensional photonic crystal only has one degree of freedom; while the other directions are considered infinite or periodic (depending upon the boundary conditions used). Two dimensional photonic crystals have two variable widths (a checkerboard); while, three dimensional photonic crystals have three variable sides (such as the sides of stacked cubes). The source of this figure is *Photonic Crystals: Molding the Flow of Light*, by Joannopoulos, Meade, and Winn.

As such, nanophotonics is an interdisciplinary field, which combines thermodynamics, electricity and magnetism, and computational methods to achieve structures suitable for many possible applications. These structures may vary in complexity, and, due to the difficulty and expense in fabricating and modeling more complex structures (two- and three-dimensional structures), we choose to focus on one-dimensional, aperiodic structures. We computationally model these structures and implement the transfer matrix formalism, which is coupled to either a genetic or hybrid optimization algorithm.

1.1 Computational Electricity and Magnetism

To fully investigate the properties of these nanophotonic structures, we will first begin with a detailed analysis of their electromagnetic properties. Starting with Maxwell's equations, we will develop a transfer-matrix formalism which we can use to analyze a one dimensional, aperiodic structure's absorption, transmission, and reflection properties.

Electromagnetic waves in free space obey Maxwell's equations:

$$\nabla \cdot \mathbf{E} = 0, \tag{1.1}$$

$$\nabla \cdot \mathbf{B} = 0, \tag{1.2}$$

$$\nabla \times \mathbf{E} = -\frac{\partial \mathbf{B}}{\partial t}, \tag{1.3}$$

$$\nabla \times \mathbf{B} = \mu_0 \epsilon_0 \frac{\partial \mathbf{E}}{\partial t}, \tag{1.4}$$

where ϵ_0 and μ_0 are the free space permittivity and permeability, respectively. Additionally we identify the propagation velocity, c is the speed of light such that $\mu_0 \epsilon_0 = c^{-2}$. By taking the curl of Equation 1.3 and 1.4, making use of the vector identity,

$$\nabla \times \nabla \times \mathbf{A} = \nabla(\nabla \cdot \mathbf{A}) - \nabla^2 \mathbf{A}, \tag{1.5}$$

we find,

$$\nabla(\nabla \cdot \mathbf{E}) - \nabla^2 \mathbf{E} = -\frac{\partial \nabla \times \mathbf{B}}{\partial t} = -\mu_0 \epsilon_0 \frac{\partial^2 \mathbf{E}}{\partial t^2}, \tag{1.6}$$

$$\nabla(\nabla \cdot \mathbf{B}) - \nabla^2 \mathbf{B} = \mu_0 \epsilon_0 \frac{\partial \nabla \times \mathbf{E}}{\partial t} = -\mu_0 \epsilon_0 \frac{\partial^2 \mathbf{B}}{\partial t^2}, \tag{1.7}$$

as well as Equations 1.1 and 1.2, we arrive at the free-space equation for electromagnetic waves:

$$\nabla^2\mathbf{E} - \frac{1}{c^2}\frac{\partial^2\mathbf{E}}{\partial^2 t} = 0, \tag{1.8}$$

$$\nabla^2\mathbf{B} - \frac{1}{c^2}\frac{\partial^2\mathbf{B}}{\partial^2 t} = 0. \tag{1.9}$$

1.1.1 Transfer Matrix Formalism

We consider light incident on an aperiodic, one-dimensional, multilayer structure composed of multiple materials with different indexes of refraction and thicknesses. Here, we restrict ourselves to materials where $\mu = \mu_0$, but $\epsilon \neq \epsilon_0$, and is, in fact, the relative permittivity of the material. Additionally, we consider structures which are infinite in both the x- and y-directions. Under these conditions, Maxwell's equations change slightly. Most notably, we

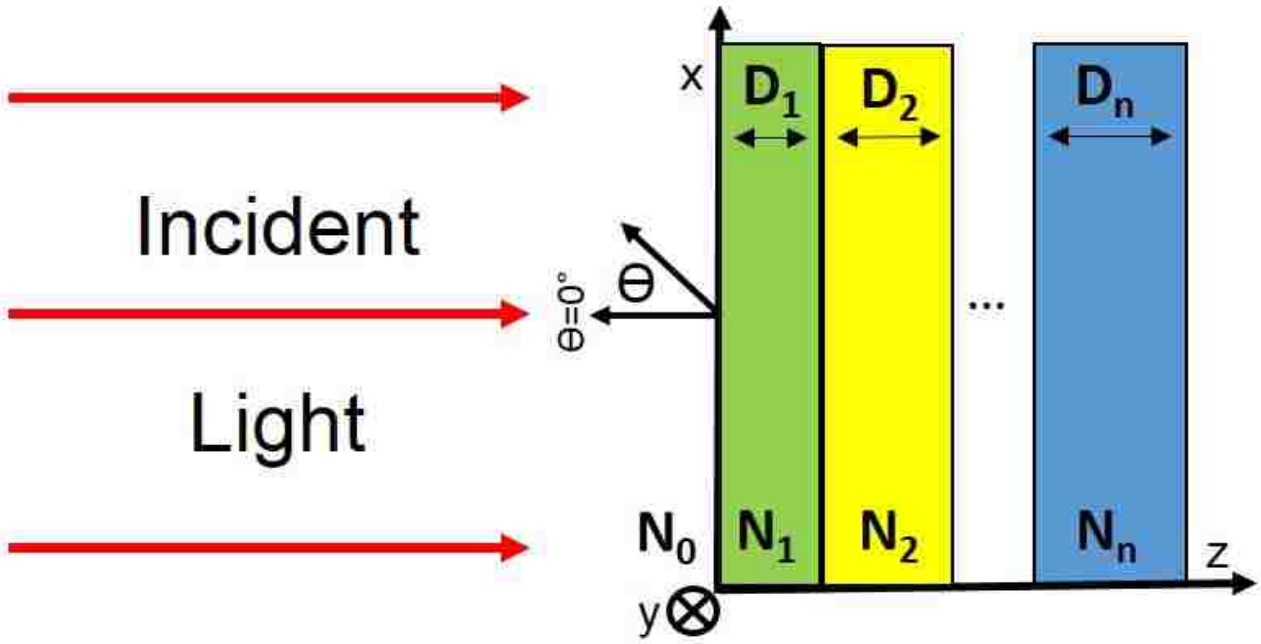

FIGURE 1.2: Light is incident from vacuum on an aperiodic n-layer structure composed of multiple materials with indexes of refraction $N_1, N_2, ..., N_n$ and thicknesses $D_1,\ D_2,\ D_3, ..., D_n$.

replace ϵ_0 with ϵ and c is no longer the speed of light in vacuum, but the speed of light in

the i^{th} layer is given by $c_i = c/N_i$, such that:

$$\nabla \cdot \mathbf{D} = \rho, \tag{1.10}$$

$$\nabla \cdot \mathbf{B} = 0, \tag{1.11}$$

$$\nabla \times \mathbf{E} = -\frac{\partial \mathbf{B}}{\partial t}, \tag{1.12}$$

$$\nabla \times \mathbf{H} = \mathbf{J} + \frac{\partial \mathbf{D}}{\partial t}, \tag{1.13}$$

where $\mathbf{J}$ is the electric current density and ρ is the free charge density present [3, 4]. In the cases we consider here, there is no free charge or electric current density, so Equations 1.10 and 1.13 simplify, yielding:

$$\nabla \cdot \mathbf{D} = 0, \tag{1.14}$$

$$\nabla \times \mathbf{H} = \frac{\partial \mathbf{D}}{\partial t}, \tag{1.15}$$

where $\mathbf{D} = \epsilon \mathbf{E}$.

To analyze the properties of such a structure, we must first consider the solutions to the electric field wave equation. By examining Maxwell's equations in the frequency domain and assuming an $e^{-j\omega t}$ harmonic time dependence for all field quantities, and, to avoid confusion, $j = \sqrt{-1}$, we can write Maxwell's equations in the following way:

$$\nabla \cdot \mathbf{D} = \rho, \tag{1.16}$$

$$\nabla \cdot \mathbf{B} = 0, \tag{1.17}$$

$$\nabla \times \mathbf{E} = j\omega \mathbf{B}, \tag{1.18}$$

$$\nabla \times \mathbf{B} = \mathbf{J} - j\omega \mathbf{D}. \tag{1.19}$$

A full solution is then just the superposition of solutions found for each individual frequency. Solutions will then have the form:

$$A e^{j(\mathbf{k}_i \cdot \mathbf{r})}, \tag{1.20}$$

where, for example, the wave vector $k_{x,i}$ in the i^{th} layer is given by:

$$k_{x,i} = \frac{2\pi N_i \sin\theta_i}{\lambda_0}, \tag{1.21}$$

N_i is the index of refraction in the i^{th} layer, θ_i is the angle of propagation in the i^{th} layer and λ_0 is the wavelength in free-space. Additionally, we can now suppress the time dependence of the solution. More specifically, in the presence of a multilayer structure which reflects some portion of incident radiation, the field to the left of the multilayer structure is given by:

$$E(x,y,z) = 1e^{j(k_{x,i}x + k_{z,i}z)} + re^{-j(k_{x,i}x - k_{z,i}z)}, \tag{1.22}$$

where we have normalized the incident field amplitude to be 1 and r is the reflection coefficient of the structure. As such, we have shown how electromagnetic radiation propagates in free space, and by extension inside the layers of our multilayer structure. Now, we must discern the effects that the interfaces between the layers have on the electromagnetic fields.

First, we begin by examining light incident at an angle θ_i as in Equation 1.21. To achieve this, we take a closer look at Figure 1.3 and examine the boundary conditions.

We consider monochromatic light propagating in the $+z$-direction and incident upon the boundary between two materials which possess indexes of refraction N_0 and N_1. We are interested in the angle of propagation of light reflected from the boundary, θ_r, and the angle of propagation of light which is transmitted into the second medium, θ_t. We consider harmonic plane waves which result from the interaction with the interface of the form:

$$Ae^{j(\mathbf{k}_i \cdot \mathbf{r})}, \tag{1.23}$$

$$Ae^{-j(\mathbf{k}_r \cdot \mathbf{r})}, \tag{1.24}$$

$$Ae^{j(\mathbf{k}_t \cdot \mathbf{r})}, \tag{1.25}$$

for each the incident, reflected, and transmitted wave. For there to be a constant relation which exists for all points of the interface, the phase, $\phi = \mathbf{k} \cdot \mathbf{r}$ of each the incident, reflected, and transmitted waves must be equal at the interface. Thus, we apply the boundary

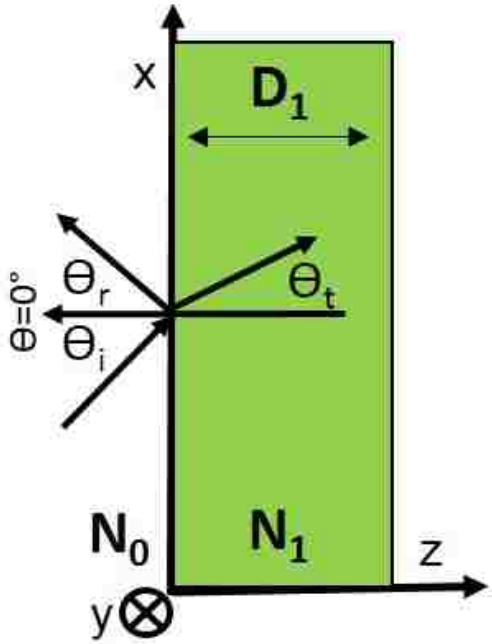

FIGURE 1.3: Light is incident at an angle θ_i on an interface between two materials with indexes of refraction N_0 and N_1 respectively.

conditions at $z = 0$, the interface between N_0 and N_1 such that:

$$\mathbf{k}_i \cdot \mathbf{r}|_{z=0} = \mathbf{k}_r \cdot \mathbf{r}|_{z=0} = \mathbf{k}_t \cdot \mathbf{r}|_{z=0}. \tag{1.26}$$

For $z = 0$, this leads to the relation:

$$k_{x,i}x = k_{x,r}x = k_{x,y}x, \tag{1.27}$$

which must be true for all values of x; therefore, we have:

$$k_{x,i} = k_{x,r} = k_{x,t}, \tag{1.28}$$

Finally, with $k_0 = \frac{2\pi N_0}{\lambda_0}$ and $k_1 = \frac{2\pi N_1}{\lambda_0}$ we can rewrite these using their constituent angles:

$k_{x,i} = k_0 \sin\theta_i,\ k_{x,r} = k_0 \sin\theta_r,\ k_{x,t} = k_1 \sin\theta_t,\ k_{z,i} = k_0 \cos\theta_i,\ k_{z,r} = k_0 \cos\theta_r,$

$k_{z,t} = k_1 \cos\theta_t, \text{and, finally, } k_{y,i} = k_{y,r} = k_{y,t} = 0$ and with $k_{x,i} = k_{x,r}$, we recover: $\theta_i = \theta_r$.

Making use of the relation derived from Equation 1.28, $k_{x,i} = k_{x,t}$, we recover Snell's Law:

$$N_0 \sin\theta_i = N_1 \sin\theta_t. \tag{1.29}$$

While Snell's law determines the direction of propagation for both the reflected and transmitted waves at the interface between two materials with difference indexes of refraction, it gives no information about the amplitude of the two waves. To establish a relationship between the incident, transmitted, and reflected amplitudes, we must further investigate the boundary conditions which apply. To achieve this, we will, once again, make use of Maxwell's equations, this time, in integral form, adjusted for electric current density, $\mathbf{J} = 0$ and free charge, $\rho = 0$:

$$\oint \mathbf{D} \cdot d\mathbf{S} = 0, \tag{1.30}$$

$$\oint \mathbf{B} \cdot d\mathbf{S} = 0, \tag{1.31}$$

$$\oint \mathbf{E} \cdot d\mathbf{l} = -\frac{\partial}{\partial t} \int_S \mathbf{B} \cdot d\mathbf{S}, \tag{1.32}$$

$$\oint \mathbf{H} \cdot d\mathbf{l} = \frac{\partial}{\partial t} \int_S \mathbf{D} \cdot d\mathbf{S}. \tag{1.33}$$

First, we will apply the boundary conditions; then, we will apply these boundary conditions to both TE (Transverse-Electric), also known as s-Polarized, and TM (Transverse-Magnetic), also known as p-Polarized, light.

We first consider the two closed surface integrals, and, as depicted in Figure 1.4 (a), we assume that the interface is surrounded by a cylinder. From Equations 1.30 and 1.31, we find that in region N_0, $d\mathbf{S} = -\hat{\mathbf{q}} dA$ and in region N_1, $d\mathbf{S} = \hat{\mathbf{q}} dA$, so these equations yield:

$$\mathbf{D}_{N_0} \cdot \hat{\mathbf{q}} = \mathbf{D}_{N_1} \cdot \hat{\mathbf{q}}, \tag{1.34}$$

$$\mathbf{B}_{N_0} \cdot \hat{\mathbf{q}} = \mathbf{B}_{N_1} \cdot \hat{\mathbf{q}}. \tag{1.35}$$

This implies that the components of $\mathbf{B}$ and $\mathbf{D}$ in the normal direction are continuous across the boundary between N_0 and N_1. Now, we consider the line integrals in Equations 1.32 and 1.33, which, as depicted in Figure 1.4 (b) involve constructing a loop across the boundary between N_0 and N_1. We note that as we let $dh \to 0$, the fluxes of both $\mathbf{B}$ and $\mathbf{H}$ across the

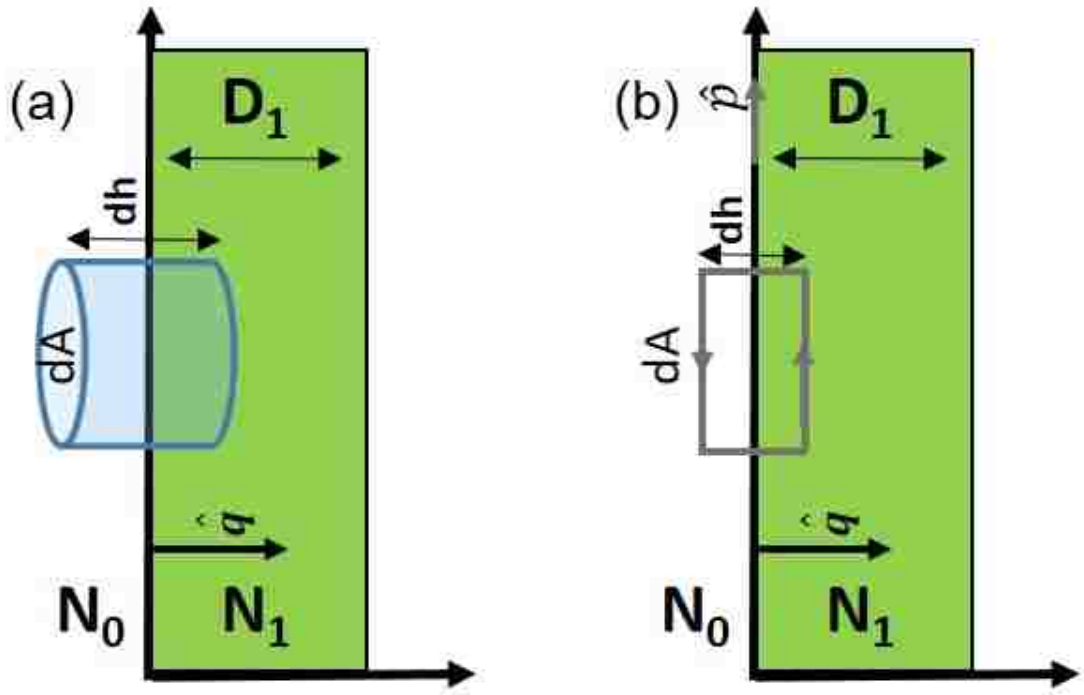

FIGURE 1.4: (a) We enclose the boundary between N_0 and N_1 with a cylinder of height dh, surface area dA whose sides are perpendicular to the surface of the interface, and $\hat{\mathbf{q}}$ is the unit vector from medium N_0 to medium N_1. (b) We enclose the boundary between N_0 and N_1 with a loop of height dh and surface area dA whose short sides are perpendicular to the surface of the interface and $\hat{\mathbf{q}}$ is the unit vector from medium N_0 to medium N_1. Here, $\hat{\mathbf{p}}$ is the unit vector which is parallel to the surface of the interface between N_0 and N_1.

boundary go to zero; therefore,

$$\mathbf{E}_{N_0} \cdot \hat{\mathbf{p}} = \mathbf{E}_{N_1} \cdot \hat{\mathbf{p}}, \tag{1.36}$$

$$\mathbf{H}_{N_0} \cdot \hat{\mathbf{p}} = \mathbf{H}_{N_1} \cdot \hat{\mathbf{p}}. \tag{1.37}$$

From this, we can surmise that $\mathbf{E}$ and $\mathbf{H}$'s tangential components are continuous across the boundary between N_0 and N_1. Now, we will apply this to the s-Polarization of light as depicted in Figure 1.5.

We begin by considering incident light at an angle θ_i to the surface of an interface between two materials:

$$\mathbf{E}_i = E_i e^{j(-\mathbf{k}_i \cdot \mathbf{r})} \hat{\mathbf{y}}, \tag{1.38}$$

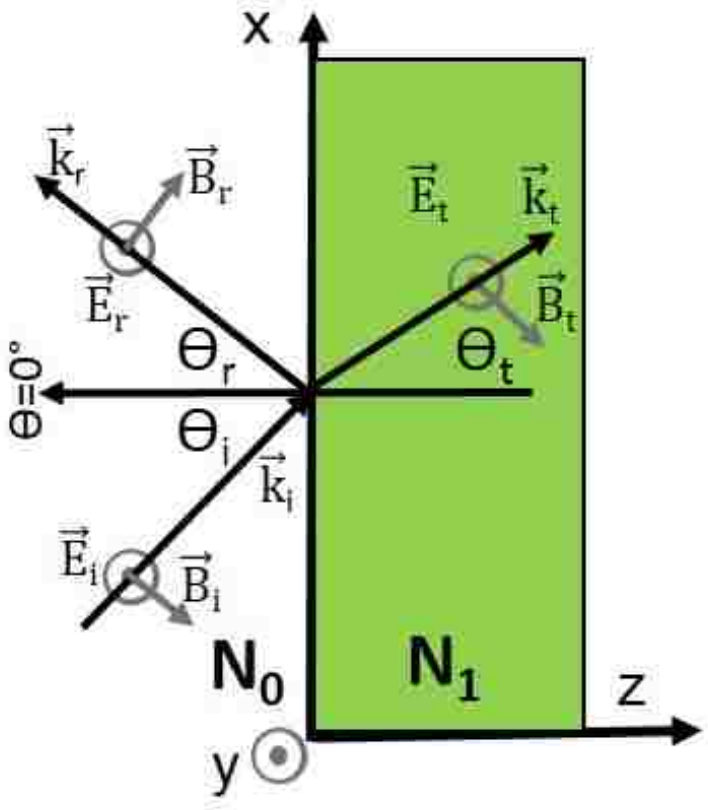

FIGURE 1.5: For Transverse Electric (s) polarized light, the electric field is perpendicular to the plane of incidence, and the magnetic field is parallel.

where, here,

$$\mathbf{k}_i = \frac{\omega N_0}{c}(\sin\theta_i \hat{\mathbf{x}} + \cos\theta_i \hat{\mathbf{z}}). \tag{1.39}$$

Similar relations exist for $\mathbf{B}_i,\ \mathbf{E}_r,\ \mathbf{B}_r,\ \mathbf{E}_t,$ and $\mathbf{B}_t$. Due to the fact that there is no normal component of the electric field for transverse electric polarized light, the condition of continuity of the $\mathbf{D}$ field is satisfied by construction. We are left with the boundary conditions that the normal (z-direction) component of $\mathbf{B}$ and the tangential (x-direction) component of $\mathbf{H}$ be continuous:

$$N_0 \sin\theta_i(\mathbf{E}_i + \mathbf{E}_r) = N_1 \sin\theta_t \mathbf{E}_t, \tag{1.40}$$

$$N_0 \cos\theta_i(\mathbf{E}_i - \mathbf{E}_r) = N_1 \cos\theta_t \mathbf{E}_t. \tag{1.41}$$

Here, we have suppressed the μ which would come from the magnetic field equations due to the fact that we only consider materials where $\mu = \mu_0$. Thus, we can normalize the incident

field such that $|\mathbf{E}_i| = 1$, rearrange Equations 1.40 and 1.41, and find that the reflection and transmission coefficients are:

$$r_{\mathrm{TE}} = \frac{N_0 \cos\theta_i - N_1 \cos\theta_t}{N_0 \cos\theta_i + N_1 \cos\theta_t}, \tag{1.42}$$

$$t_{\mathrm{TE}} = \frac{2N_0 \cos\theta_i}{N_0 \cos\theta_i + N_1 \cos\theta_t}. \tag{1.43}$$

We then can calculate the reflection and transmission coefficients for transverse magnetic polarized light by a similar process and by taking into account the difference in the electric and magnetic field directions as depicted in Figure 1.6.

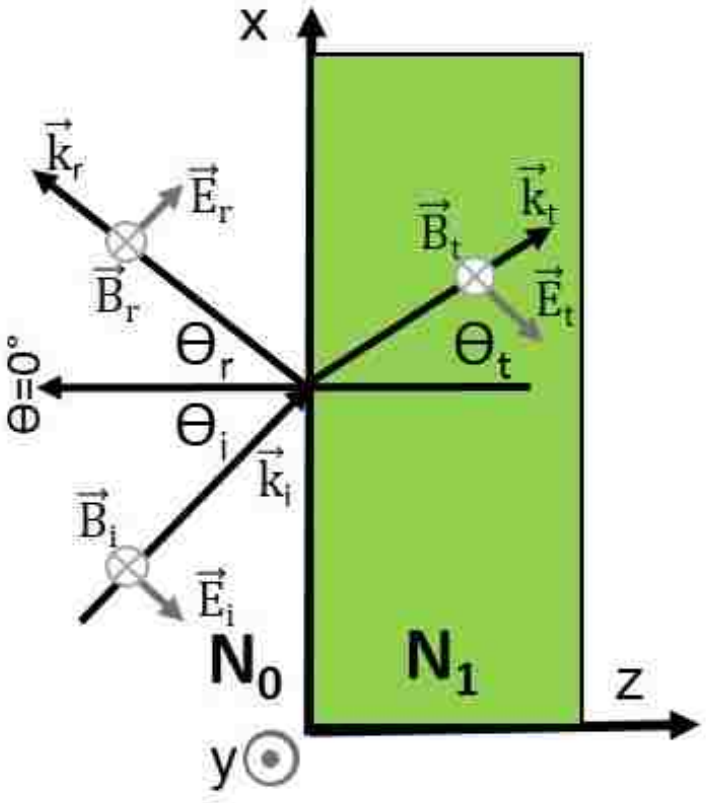

FIGURE 1.6: For Transverse Magnetic (p) polarized light, the electric field is parallel to the plane of incidence, and the magnetic field is perpendicular.

The continuity equations are:

$$\cos\theta_i(\mathbf{E}_i - \mathbf{E}_r) = \cos\theta_t \mathbf{E}_t, \tag{1.44}$$

$$\mathbf{B}_i + \mathbf{B}_r = \mathbf{B}_t, \tag{1.45}$$

which then, by relating $\mathbf{E}$ and $\mathbf{B}$ in the following way, $\mathbf{B} = \frac{N}{c}\mathbf{E}$, where N is the index of refraction in the first or second medium, leads to the transverse magnetic reflection and transmission coefficients,

$$r_{\mathrm{TM}} = \frac{-N_0 \cos\theta_t + N_1 \cos\theta_i}{N_0 \cos\theta_t + N_1 \cos\theta_i}, \tag{1.46}$$

$$t_{\mathrm{TM}} = \frac{2N_0 \cos\theta_i}{N_0 \cos\theta_t + N_1 \cos\theta_i}. \tag{1.47}$$

As expected, for $\theta_i = 0$, we recover:

$$r_{\mathrm{TE}} = r_{\mathrm{TM}} = \frac{N_1 - N_0}{N_0 + N_1}, \tag{1.48}$$

$$t_{\mathrm{TE}} = t_{\mathrm{TM}} = \frac{2N_0}{N_0 + N_1}, \tag{1.49}$$

under the Fresnel equation symmetry relations [5], which allow us to equate the following coefficients:

$$r_{N_0,N_1} = -r_{N_1,N_0}, \tag{1.50}$$

$$t_{N_0,N_1} t_{N_1,N_0} + r_{N_0,N_1} r_{N_1,N_0} = 1. \tag{1.51}$$

Now, we must consider how to approach both the boundary conditions and free propagation in tandem. For this, we return to Figure 1.2 and Equations 1.20 and 1.21 to formulate the transfer matrix method. We consider the field to the left (and in principle in the i^{th} layer) of the multilayer structure for $z < 0$, which now, is composed of both a forward-propagating (in the positive z-direction of amplitude $\mathbf{E}^i_+$) and a reflected wave (traveling in the negative z-direction of amplitude $\mathbf{E}^i_+$) of the i^{th} layer.

$$\mathbf{E}(x, y, z) = \mathbf{E}^i_+ e^{j(k_{z,i} z)} e^{j(k_{x,i} x)} + \mathbf{E}^i_- e^{-j(k_{z,i} z)} e^{j(k_{x,i} x)}, \tag{1.52}$$

where k is as defined in Equation 1.21. Henceforth, we will suppress the variation in the x-direction, as it only serves to keep track of phase in that direction. Now, we can discern

a matrix which will propagate the changes in the electromagnetic field (phase accumulation and attenuation of the field) across a layer. That is, we will compose a matrix equation for E_+^{i+1} and E_-^{i+1} from E_+^i and E_+^i, and we have dropped the vector form of the electric field due to the fact that the fields which are not in the direction of propagation do not contribute to this analysis:

$$\begin{pmatrix} E_+^{i+1} \\ E_-^{i+1} \end{pmatrix} = \begin{pmatrix} e^{j\phi} & 0 \\ 0 & e^{-j\phi} \end{pmatrix} \begin{pmatrix} E_+^i \\ E_-^i \end{pmatrix}, \tag{1.53}$$

where $\phi = \dfrac{2\pi N_i D_i \cos\theta_i}{\lambda}$, and, again, N_i and θ_i are the index of refraction and angle of propagation in the i^{th} layer, D_i is the thickness of the i^{th} layer. That is, we account for the phase change and, in principle, loss in the following way:

$$E_+^{i+1} = e^{j\phi} E_+^i, \tag{1.54}$$

$$E_-^{i+1} = e^{-j\phi} E_-^i, \tag{1.55}$$

which means that the forward (rightward) propagating wave accumulates a phase $e^{j\phi}$, and the backward (leftward) propagating wave gains a phase $e^{-j\phi}$.

Finally, let us consider writing the boundary conditions in matrix form. Due to internal reflection and transmission, we could, in principle, have both forward and backward propagating waves for both $E_-^{i+1}$and E_+^{i+1}, so, we desire a matrix which will operate in the following manner:

$$E_+^{i+1} = t_{i,i+1} E_+^i + r_{i+1,i} E_-^{i+1}, \tag{1.56}$$

$$E_-^i = r_{i,i+1} E_+^i + t_{i+1,i} E_-^{i+1}. \tag{1.57}$$

Now, Equations 1.56 and 1.57 form a system of equations which we can solve and isolate E_+^i and E_-^i from $E_+^{i+1}$and E_-^{i+1}, which will allow us to combine the boundary conditions with the propagation matrix shown in Equation 1.53. Solving the system of equations and

using the symmetry relations of the Fresnel coefficients, found in Equations 1.50 and 1.51, we can accomplish this:

$$\begin{pmatrix} E_+^i \\ E_-^i \end{pmatrix} = \begin{pmatrix} \frac{1}{t_{i,i+1}} & \frac{r_{i,i+1}}{t_{i,i+1}} \\ \frac{r_{i,i+1}}{t_{i,i+1}} & \frac{1}{t_{i,i+1}} \end{pmatrix} \begin{pmatrix} E_+^{i+1} \\ E_-^{i+1} \end{pmatrix}. \tag{1.58}$$

Thus, we have established a transfer-matrix formalism for the boundary conditions, and need only to combine it with the propagation through a layer found in Equation 1.53; therefore, we define $\delta_{i,i+1}$, as the boundary condition matrix for the boundary between the i and $i+1$ layer, and, by solving Equation 1.53 for the fields in the i^{th} layer, we can recover the propagation matrix for the i^{th} layer, Π_i :

$$\delta_{i,i+1} = \begin{pmatrix} \frac{1}{t_{i,i+1}} & \frac{r_{i,i+1}}{t_{i,i+1}} \\ \frac{r_{i,i+1}}{t_{i,i+1}} & \frac{1}{t_{i,i+1}} \end{pmatrix}, \tag{1.59}$$

$$\Pi_i = \begin{pmatrix} e^{-j\phi} & 0 \\ 0 & e^{j\phi} \end{pmatrix}. \tag{1.60}$$

Thus, we have successfully related the fields on the left and right hand sides of the n-layer structure in Figure 1.2:

$$\begin{pmatrix} E_+^0 \\ E_-^0 \end{pmatrix} = \delta_{0,1} \prod_{i=1}^{n-1} \Pi_i \delta_{i,i+1} \Pi_n \begin{pmatrix} E_+^n \\ 0 \end{pmatrix}, \tag{1.61}$$

where E_-^n is identically zero because there is no incident field from the right side of the structure. This allows us to extract the overall reflection and transmission coefficients for the structure. By rewriting the product which corresponds to the boundary conditions and propagation matrices, we find:

$$\begin{pmatrix} E_+^0 \\ E_-^0 \end{pmatrix} = \begin{pmatrix} M_{1,1} & M_{1,2} \\ M_{2,1} & M_{2,2} \end{pmatrix} \begin{pmatrix} E_+^n \\ 0 \end{pmatrix}. \tag{1.62}$$

Solving the system of equations for the reflection, r, and transmission, t, coefficients of the structure yields:

$$\frac{E_-^0}{E_+^0} = r = \frac{M_{2,1}}{M_{1,1}}, \tag{1.63}$$

$$\frac{E_+^n}{E_+^0} = t = \frac{1}{M_{1,1}}. \tag{1.64}$$

In principle, if there were a semi-infinite substrate (as there is in many calculations presented in this dissertation), the calculation would end with $\delta_{n-1,n}$ and the transmission coefficient would be identically zero. We can then calculate the power reflected, R, transmitted, T, and absorbed, A, by the structure:

$$R = |r|^2 = \frac{M_{2,1}}{M_{1,1}} \frac{M_{2,1}^*}{M_{1,1}^*}, \tag{1.65}$$

$$T = |t|^2 = \frac{1}{M_{1,1}} \frac{1}{M_{1,1}^*}, \tag{1.66}$$

and, by conservation of energy,

$$A_{\mathrm{TE/TM}}(\lambda, \theta) = 1 - R_{\mathrm{TE/TM}}(\lambda, \theta) - T_{\mathrm{TE/TM}}(\lambda, \theta), \tag{1.67}$$

where the dependence of the absorptance, reflectance, and transmittance upon polarization, wavelength, and angle of incidence is explicitly shown.

We can go through a similar process, which will be outlined here, to reach a transfer-matrix formalism for the **E** and **H** fields which will give insight as to the physical mechanisms which drive the absorption and emission of the structures. The reflection and transmission coefficients for the structure, gotten by the previously outlined method, are necessary to compute the fields. We find that the electric and magnetic fields, as a function of z through the first layer of thickness D_1, again, as depicted in Figure 1.2, are:

$$\begin{pmatrix} E(z) \\ Z_0 H(z) \end{pmatrix} = \begin{pmatrix} \cos\left(\frac{2\pi N_i z}{\lambda}\right) & -\frac{j}{N_i}\sin\left(\frac{2\pi N_i z}{\lambda}\right) \\ -jN_i \sin\left(\frac{2\pi N_i z}{\lambda}\right) & \cos\left(\frac{2\pi N_i z}{\lambda}\right) \end{pmatrix} \begin{pmatrix} E(z = z_0) \\ Z_0 H(z = z_0) \end{pmatrix}, \tag{1.68}$$

where $E(z = z_0)$ is the field calculated by the method shown in Equations 1.61-1.64 and Z_0 is the free-space impedance. Thus, we are able to extract the field at each position z as the field moves from left to right in the structure. It is important to note that at the end of each layer, we multiply by an additional propagation matrix after accounting for the phase accumulated in that layer by setting $z = D_i$, where D_i is the thickness of the i^{th} layer. We

can also calculate the power as a function of z within the structure, and, as a result, locate areas of high and low loss within the structure.

Starting with the Poynting vector, which computes the rate of energy transfer per unit area,

$$\mathbf{S} = \mathbf{E} \times \mathbf{H}. \tag{1.69}$$

We can rewrite Equation 1.69 in a more useful form, assuming a sinusoidal field and computing the time-averaged value of the Poynting vector $\mathbf{S}$, by considering the integral over a time T:

$$< \mathbf{S} >= \frac{1}{T} \int_0^T \mathbf{S}(t)\, dt, \tag{1.70}$$

which then yields the time-averaged Poynting vector:

$$< \mathbf{S} >= \frac{1}{2} Re(\mathbf{E} \times \mathbf{H}^*). \tag{1.71}$$

Thus, we have established methods for calculating the absorption, transmission, and reflection coefficients for an n-layered one-dimensional structure. We have also outlined a method for extracting the exact fields within the layers of the structure and shown that the power (and therefore, the loss) can be calculated.

1.2 Thermodynamics

Many of the applications of nanophotonic structures are motivated by the laws of thermodynamics. These structures have clear applications as absorbing devices, useful for, among other things, light filters and solar energy conversion. We must investigate the process of the emission of light from heated objects, which will be useful in this end. While we have only explored a method for calculating the absorptance of multilayer structures, we make use of Kirchoff's law to equate absorption and emittance under the condition of thermal equilibrium. Using Kirchoff's law, in conjunction with Planck's theory of Blackbody radiation is necessary to explore the usefulness of these aperiodic multilayer structures as thermal

emitters, which have a wide variety of applications, including spectroscopic detectors and replacements for incandescent lightbulbs.

1.2.1 Blackbody Radiation

The theory of Blackbody radiation [6] is well-known. Under the condition of thermal equilibrium, we consider a cube with sides of length L. In each dimension, we note that the allowed momenta and wavelengths are:

$$\lambda = \frac{2L}{n} \text{ and } p = \frac{hn}{2L}, \tag{1.72}$$

where n is a positive integer used to label the specific oscillatory mode, h is Planck's constant, and c is the speed of light. Here, the energy associated with any photon is

$$E(n) = \frac{hcn}{2L}. \tag{1.73}$$

Thus, we consider these quantities in three-dimensions:

$$E(n) = c\sqrt{p_x^2 + p_y^2 + p_z^2} = \frac{hc}{2L}\sqrt{n_x^2 + n_y^2 + n_z^2}, \tag{1.74}$$

and use Equation 1.72 again, where we consider n as the magnitude of the $\{n_x, n_y, n_z\}$ three vector. Now, we make use of the partition function [7] in statistical mechanics, which is defined:

$$Z(\beta) = \sum_{n=0}^{\infty} e^{-\beta E(n)} = \frac{e^{-\frac{\beta E(n)}{2}}}{1 - e^{-\beta E(n)}}, \tag{1.75}$$

where $\beta = \frac{1}{k_B T}$, k_B is the Boltzmann constant, and T is the temperature. Finally, we can calculate the expected energy in each mode:

$$< E >= -\frac{\partial ln[Z(\beta)]}{\partial \beta} = \frac{E(n)}{2} + \frac{E(n)}{e^{\beta E(n)} - 1}. \tag{1.76}$$

If we now consider the states with energies that lie in a small range $E(n) < E < E(n) + \delta$, define $g(E)$ as the density of states:

$$U = \int_0^{\infty} \frac{E(n)}{e^{\beta E(n)} - 1} g[E(n)] dE(n). \tag{1.77}$$

We recall Equations 1.72 and 1.73, and we discover that this $g[E(n)]dE(n)$ integral is comprised of a single octant of a spherical shell; thus, by accounting for two polarizations of light (an additional factor of two in the number of states) and the $g[E(n)]dE(n) = 4\pi n^2 dn = \frac{8\pi L^3 E^2}{h^3 c^3} dE$ contribution to the integral is found, and we are able to drop the $E(n)$ notation, yielding:

$$U = \frac{8\pi L^3}{h^3 c^3} \int_0^\infty \frac{E^3}{e^{\beta E} - 1} dE, \tag{1.78}$$

$$\mu = \frac{8\pi h}{c^3} \int_0^\infty \frac{\nu^3}{e^{\frac{h\nu}{k_B T}} - 1} d\nu, \tag{1.79}$$

which is an integral we can carry out to find the power radiated per unit area and wavelength, the Planck blackbody spectrum (in units of Watt per square meter per nanometer):

$$B(\lambda, T) = \frac{2hc^2}{\lambda^5} \frac{1}{e^{\frac{hc}{\lambda k_B T}} - 1}. \tag{1.80}$$

It is important to note here, that $B(\lambda, T)$ is used interchangeably with μ only for a perfect blackbody. If we wish to extend this to other objects, we must alter the form of μ slightly, which will be discussed in Section 1.3.2.

Let us now investigate some of the properties of this distribution. We can calculate the power radiated per unit area as a function of temperature by considering Equation 1.79, and making the substitution $q = \frac{h\nu}{k_B T}$, which leads to the integral:

$$\mu = (\frac{k_B T}{h})^4 \frac{8\pi h}{c^3} \int_0^\infty \frac{q^3}{e^q - 1} dq = \frac{8\pi^5 k_B^4}{15 c^3 h^3} T^4; \tag{1.81}$$

thus, we recover the power radiated by a blackbody as a function of temperature, the Stefan-Boltzman law:

$$\mu = \sigma T^4, \tag{1.82}$$

where $\sigma = 7.566 \times 10^{-16} \frac{J}{m^3 K^4}$.

1.3 Kirchoff's Law

We seek a method to relate the emittance of an object (how well a particular object, or, in our case, the multilayer structure) emits a given wavelength λ. To achieve this, we will investigate

the implications of a simple system and the laws of thermodynamics. It is important to note that a full proof of Kirchoff's laws is beyond the scope of this dissertation, and we will only complete an argument for Kirchoff's law of thermal radiation here, which speaks to the link between emittance and absorptance. This law also spoke to the dependence of thermal radiation on the wavelength of light radiated; however, that portion of the work has since been overshadowed by Planck's work on blackbody radiation shown in Equation 1.80.

We consider placing a hot block of material, with emittance $\epsilon_b(\lambda)$ and absorptance $A_b(\lambda)$ in an extremely-well-insulated container, with emittance $\epsilon_c(\lambda) = 1$ and absorptance $A_c(\lambda) = 1$, a perfect blackbody. The block of material emits radiation. Specifically, we choose to consider the positive x direction, without loss of generality. At a wavelength, λ_0, the radiation which is emitted over the cross-section dA of the block facing the positive x direction is given by $\epsilon_b(\lambda)B(\lambda, T_b)dA$. Similarly, the wall of the container emits radiation which will fall on that same area dA which is given by $\epsilon_c(\lambda)B(\lambda, T_c)dA$. The wall of the container absorbs A_c of incident power and the block absorbs A_b of the incident power, where each $0 < A_c, A_b < 1$. Now, we have that the transfer of energy onto the surface of the block of material:

$$Q = A_b(\lambda)\epsilon_c(\lambda)B(\lambda, T_c)dA - \epsilon_b(\lambda)B(\lambda, T_b)dA, \tag{1.83}$$

which is to say that the container absorbs a fraction $A_c(\lambda)$ of the incident radiation, and then re-radiates a portion. Now, If we consider the system in thermodynamic equilibrium, we know that $B(\lambda, T_b) = B(\lambda, T_c)$, the walls are a perfect blackbody, and that the transfer of energy $Q = 0$ due to the second law of thermodynamics, which yields:

$$A_b(\lambda) = \epsilon_b(\lambda). \tag{1.84}$$

That is, the absorptance of the black and the emittance of the block of material are equal under the condition of thermal equilibrium. Thus, we have recovered Kirchoff's law for radiation: In the state of thermal equilibrium, the emittance and absorptance of a given object

must be equal. We can now combine Equations 1.80 and 1.84:

$$\mu(\lambda,\theta) = \epsilon_{\text{Total}}(\lambda,\theta)\frac{2hc^2}{\lambda^5}\frac{1}{e^{\frac{hc}{\lambda k_B T}}-1}, \tag{1.85}$$

which is the power radiated per unit area and unit wavelength by a non-blackbody as a function of wavelength, angle, and temperature. Here, $\epsilon_{\text{Total}}(\lambda,\theta)$ is the averaged emittance from both the TE and TM polarizations.

1.3.1 Solar Thermophotovoltaics for Power Generation

Traditional solar energy conversion occurs when incident radiation from the Sun falls on a solar cell, which contains a photovoltaic cell and is converted into usable energy via the photoelectric effect. This conversion process takes place when an incident photon dislodges an electron which is orbiting an atom. This now free electron had some transition energy that is a function of the material used in the photovoltaic cell wafer and is commonly referred to as the band gap. A maximum conversion efficiency by the solar cell is reached when incident light on the wafer is comprised only of monochromatic light tuned to the band gap wavelength λ_0.

Figure 1.7 depicts the solar irradiance, the energy incident on the earth's surface which is usable by a photovoltaic cell. Solar radiation is broadband. Approximately 42% of solar radiation lies in the visible; while around 55% is in the infrared. The final 3% is found in the ultraviolet, with wavelengths less than 400 nm. Because of large spread in incident radiation, photovoltaic solar cells are extremely inefficient. Photons which have a lower energy than the bandgap simply cannot excite a transition; while, photons which have a higher energy than the band gap waste any energy they have in excess of the band gap.

In recent history, there has been much research in the area of these cells. Some research suggests that employing concentrators to increase the amount of radiation which falls on the solar cell to both decrease initial investment cost and increase efficiency; however, concentrators are extremely bulky and heavy, not suitable for use on spacecraft. Additionally, while it is cheaper to increase the incident radiation on solar cells with concentrators than it is to

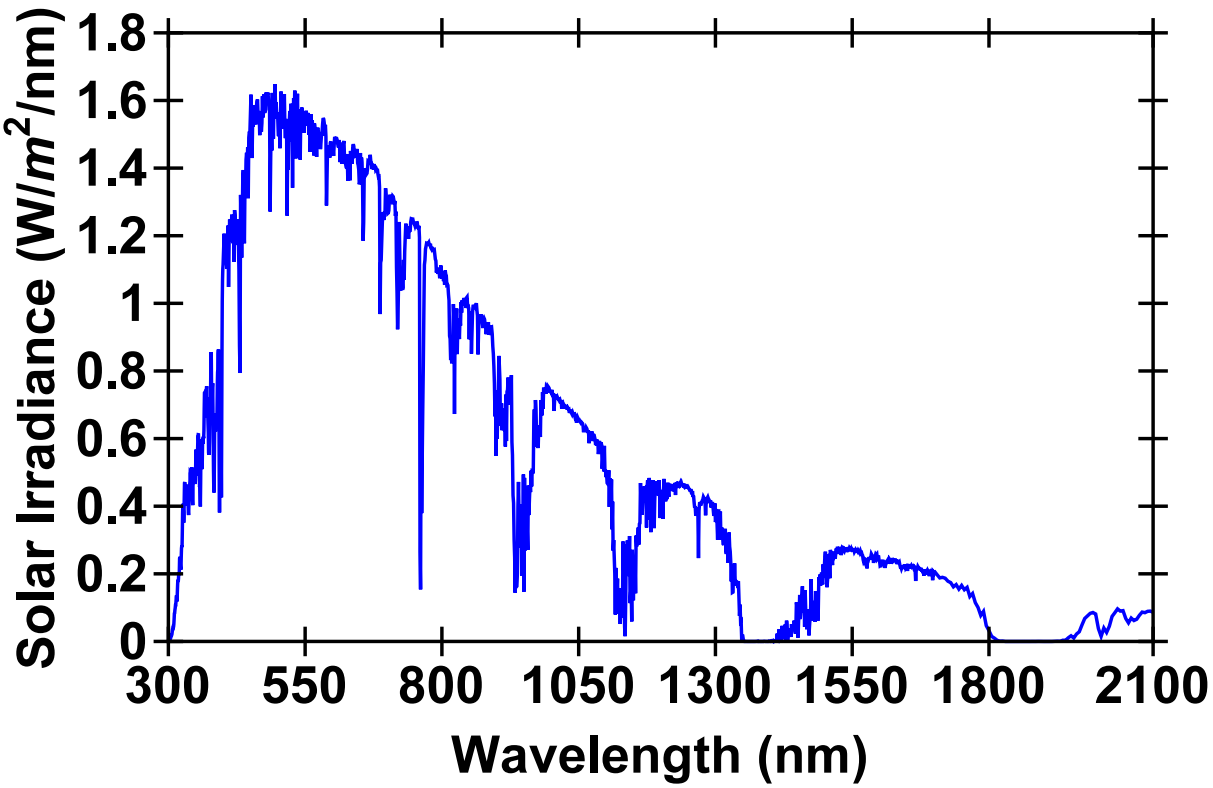

FIGURE 1.7: Solar irradiance incident on the earth's surface in units of watt per meter squared per nanometer. Above the earth's surface, approximately 1400 watts per meter squared is incident; however, due to the screening effects of the atmosphere, this falls to approximately 1100 watts per meter squared at sea-level.

simply increase the surface area which is composed of wafers, the concentrators themselves are still quite expensive.

Other research (and some in-practice solar plants) has developed multi-junction solar cells. While conventional photovoltaic cells utilize one semiconductor material to convert a small range of wavelengths efficiently, multi-junction photovoltaic cells use two, three, or even four different layers of semiconductor materials to efficiently convert a larger portion of the Sun's radiation to usable energy.

In 2007, Florescu et al proposed two closely related new designs as seen in Figure 1.8 for solar cells relying on solar thermophotovoltaics - utilizing the heat from the Sun's radiation to cause monochromatic thermal emission from a nanophotonic emitter [8]. A blackbody's

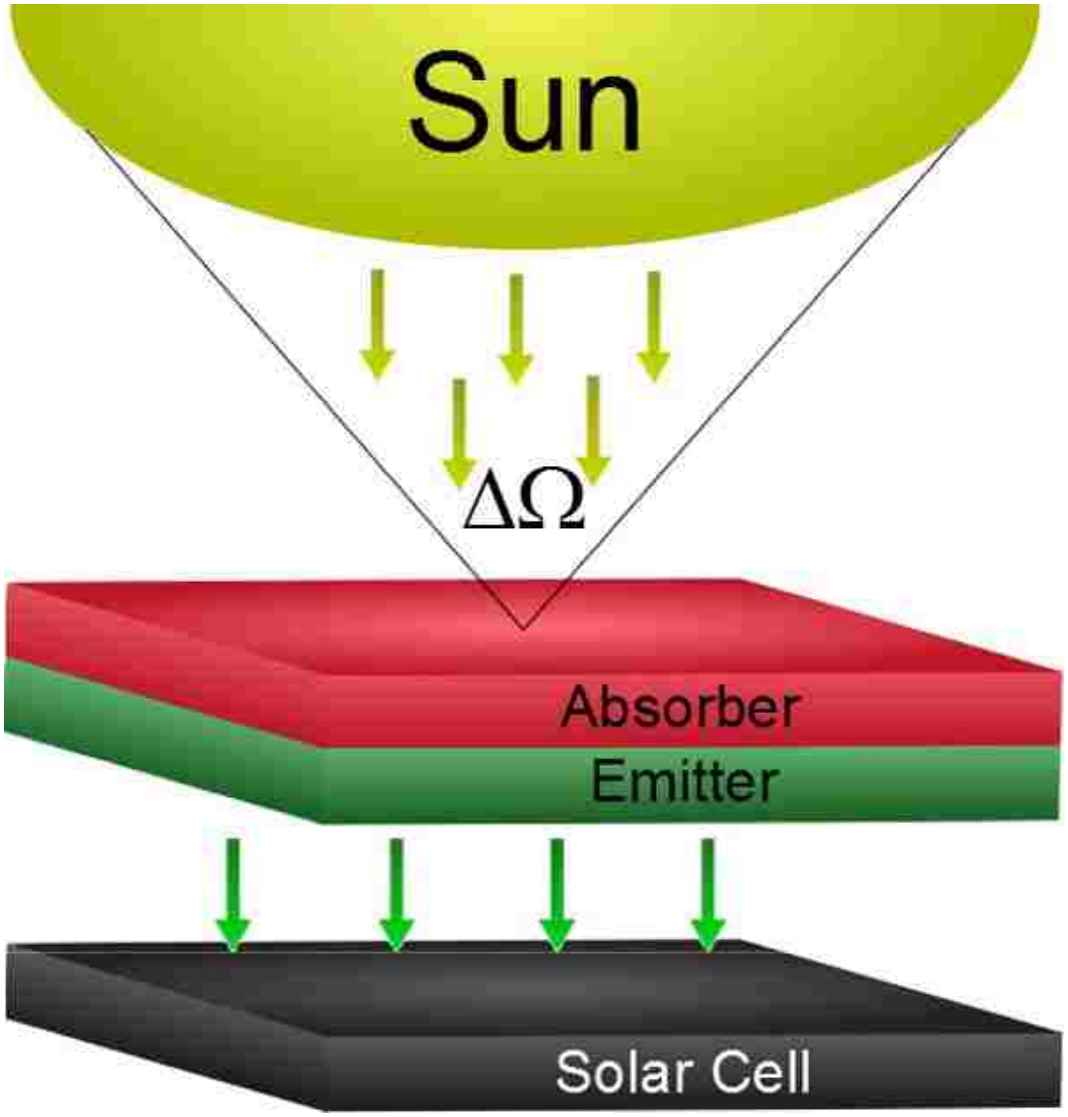

FIGURE 1.8: Schematic of proposed energy conversion device. Radiation from the Sun is incident on an absorbing layer which is in contact with a narrowband emitting layer. Narrowband radiation from the emitting layer strikes the solar cell and is converted with high efficiency to usable energy. Here $\Delta\Omega$ is the solid angle subtended by the Sun at the surface of the absorbing layer of the solar cell.

radiant power is given by Equation 1.82 and the efficiency of a Carnot Engine is given by:

$$\eta = 1 - \frac{T_c}{T_h}, \tag{1.86}$$

where T_h is the temperature of the absorbing layer and T_c is the temperature of the cell. It is important to note here, that for the purposes of this discussion, we are suppressing the dependence of emittance on wavelength. In principle, for the absorbing layer, the integral

leading to the calculation of Equation 1.82 would need to be numerically evaluated and depend on $\epsilon(\lambda, \theta, \phi)$. However, for this discussion, we will continue to assume that for the absorbing layer, $\epsilon(\lambda, \theta, \phi) = 1$ and consider the incident radiation on the cell as well as the energy which is re-radiated by the cell due to spontaneous thermal emission:

$$P_{net} = \frac{F_s}{\pi}\sigma T_s^4 - \frac{F_a}{\pi}\sigma T_a^4, \tag{1.87}$$

in which each term resembles Equation 1.82 due to the fact that the form factors $\frac{F_a}{\pi}$ and $\frac{F_s}{\pi}$ are the ratios of the solid angle subtended by the Sun and the absorbing cross section to the total solid angle facing the other. Here, T_s is the surface temperature of the Sun, T_a is the temperature of the absorbing layer, and σ is the Stefan Boltzmann constant.

Let us now investigate the the normalization factor of π. Equation 1.82 applies to a blackbody with emittance $\epsilon = 1$ for all wavelengths; here, the Sun is, to a very good approximation, a blackbody, but is located a large distance from the Earth. This decreases the solid angle subtended by the Sun and must be accounted for. Similarly, our absorbing layer is not a perfect blackbody. That is, ϵ_a *and* A_a, the emittance and absorptance, respectively, of the absorbing layer can be written as $\epsilon_a = A_a < 1$. The solid angle subtended by the Sun is given by:

$$F_s = \Omega = \int\int_{\text{Surface}} \frac{\hat{\mathbf{r}} \cdot \hat{\mathbf{n}}\ d\mathbf{S}}{r^2}, \tag{1.88}$$

where $\hat{\mathbf{r}}$ and $\hat{\mathbf{n}}$ are the unit vectors in the direction of the viewer and to the surface, respectively. For the sum this dot product can be closely approximated as unity. Therefore, we are left with the cross sectional area of the Sun, and the radius at which the earth orbits the Sun, leading to $F_a = 6.796 \times 10^{-5}\ sr$. Following a similar argument and accounting for the fact that the emittance and absorptance of the absorbing layer are not one, as well as the fact that the backradiation of the absorbing layer will follow that of a Lambertian object we can write:

$$F_a = \int_0^{\infty} \int_0^{2\pi} \int_0^{\frac{\pi}{2}} \epsilon_{\text{Total}}(\lambda, \theta) \frac{2hc^2}{\lambda^5} \frac{1}{e^{\frac{hc}{\lambda k_B T}} - 1} \sin(\theta) \cos(\theta) \, d\theta \, d\phi \, d\lambda, \tag{1.89}$$

where, for a one-dimensional multilayer structure, the emittance does not depend on ϕ. Thus, we seek to maximize the solar thermophotovoltaic cell efficiency, given by:

$$\eta_{\text{TPV}} = (1 - \frac{F_a T_a^4}{F_s T_s^4})(1 - \frac{T_c}{T_a}), \tag{1.90}$$

where the left multiplicand accounts for the efficiency of the Sun-absorber system and the right multiplicand accounts for the efficiency of the absorber-emitter. If we assume a small solid angle for absorption such that F_a/F_s is on the order of 100, we note that the theoretical limit of thermophotovoltaic energy conversion efficiency nears 70% [9].

Thus, we seek to maximize the temperature of the absorbing layer. This can be accomplished by a broadband, narrow angle absorbing layer. Our search for such a layer to serve as a key component of this system is found in Chapter 3.

1.4 Discussion of Optimization Algorithms

Physics in general, and, in particular, computational electricity and magnetism often presents problems which possess solution spaces which are incredibly vast. For instance, a seemingly simple 16-layer aperiodic multilayer structure that will be discussed in Chapter 2 has approximately 2×10^{48} possible solutions, even in the case of discretizing the layer length. Specifically, in most situations, we choose the smallest layer change to be 1 nm. Thus even using today's high-powered computers, finding an optimal solution to this problem by brute force would likely take years to achieve. Therefore, we must employ optimization algorithms to quickly and efficiently assess the solution space and produce a solution in a reasonable period of time. Genetic optimization algorithms [10] are very-well suited for global optimization (searching a large portion of a solution space); however, they do not perform efficiently for local optimization. Therefore, in this dissertation, we employ a genetic optimization algorithm both by itself as well as a hybrid [11] code which couples the genetic algorithm to an optimization suite packaged by Massachusetts Institute of Technology called NLOPT [12].

A genetic algorithm is an optimization procedure which begins with a randomly selected population of possible solutions. It gradually evolves toward an improved solution by applying genetic operators which are patterned after the natural selection process. To begin the calculation, a random selection of values for the genes is created and assigned to a population of chromosomes. Then, the genetic algorithm iteratively generates a new population by the crossover, mutation, and selection operators.

The work in this dissertation made use of a microgenetic algorithm, which has been shown to avoid the problem of premature convergence which is associated with more traditional, large-population genetic algorithms. The microgenetic algorithm also shows faster convergence to the near-optimal region [13, 14, 15]. A microgenetic algorithm begins with a small population of random members which evolves and converges after a few generations. Here, the genetic algorithm selects a new random population, and the evolution process restarts while keeping the best individual from the previously converged generation.

It is here that in some of the results (particularly in Chapter 4) contained in this document we make use of the NLOPT optimization package which provides access to extremely efficient local optimization algorithms. Specifically, we make use of the COBYLA [16] (Constrained Optimization by Linear Approximations) algorithm contained in NLOPT. This optimization algorithm maps the local area by examining small changes in the optimization parameters; then, the algorithm follows this mapping to the local maximum. Once no further improvement can be found in a small region around the best solution, the new optimized parameters are returned to the microgenetic algorithm for further optimization. In results presented in Chapters 2 and 3, however, we do not utilize the NLOPT optimization package.

A tournament selection scheme is employed in this genetic algorithm. Here, we select a subpopulation of individuals at random from the general population. This subpopulation competes on the basis of their fitness values. We then choose the individual with the highest fitness value as the winner and the process is repeated. It has been shown that this selection

scheme converges more rapidly and operates more quickly when compared to other competing schemes [17]. We then select a pair of individuals as the parents, and the crossover operator creates two offspring. These offspring possess a combination of the chromosomes of their parents. Here, we use uniform crossover [17, 14] rather than single-point crossover, as it has been shown that microgenetic algorithm convergence is faster with uniform crossover. For each generation, we employ an elitist [18] strategy, choosing the best individual from the previous population to pass on to the next.

Chapter 2

Optimized Aperiodic Highly Directional Narrowband Infrared Emitters

In this chapter, we present optimized aperiodic structures for use as narrowband, highly directional thermal infrared emitters for both TE and TM polarizations. These aperiodic multilayer structures designed with alternating layers of silicon and silica on top of a semi-infinite tungsten substrate exhibit extremely high emittance peaked around the wavelength at which the structures are optimized. Structures were designed by a genetic optimization algorithm coupled to a transfer matrix code which computed thermal emittance. First, we investigate the properties of the genetic-algorithm optimized aperiodic structures and compare them to a previously proposed resonant cavity design. Second, we investigate a structure optimized to operate at the Wien wavelength corresponding to a near-maximum operating temperature for the materials used in the aperiodic structure. Finally, we present a structure that exhibits narrowband and highly directional emittance for both TE and TM polarizations at the frequency of one of the molecular resonances of carbon monoxide (CO); hence, the design is suitable for use in the emitting portion of a detector of CO via absorption spectroscopy.[1]

2.1 Introduction

The thermal emittance of both bulk materials and textured structures has been widely investigated over recent years. Bulk thermal emittance sources (such as tungsten) possess incoherent, isotropic, and broadband radiation spectra that vary from material to material; however, it is well-known that these radiation spectra can be drastically altered by utilizing textured surfaces [19], multilayer structures, or even three-dimensional constructions [20] possibly in tandem with a bulk material substrate. From highly directional emitters (anten-

[1]Part of this chapter previously appeared as C. H. Granier, F. O. Afzal, C. Min, J. P. Dowling, and G. Veronis, "Optimized aperiodic highly directional narrowband infrared emitters," J. Opt. Soc. Am. B, **31**, 1316, (2014). It is reprinted by permission of the Optical Society of America (OSA). See the permission letter in the Appendix.

nae) to quasi-coherent radiation sources [21, 22] (lasers), as well as solar photovoltaics [23, 9], these emitters may have many uses due to their emittance spectra altering properties.

There are several approaches that have been used to achieve narrowband, highly directional thermal emittance. One of these approaches, with one-dimensional photonic crystals, employed a periodic quarter-wave stack with a half-wavelength resonant cavity as well as tungsten or silver substrate. This design resulted in the bulk substrate exhibiting directional, tunable, wavelength-selective emittance [24]. A similar outcome was realized using periodic one-dimensional metallic photonic crystal slabs [25]. Another approach to achieve coherent thermal emittance is to use gratings [26, 27, 28] or textured metal surfaces [29]. Other approaches include utilizing metamaterials [30] or shock waves propagating through a crystal [31, 32] to achieve this end. Finally, narrowband, highly directional transmittance can be achieved by a photonic heterostructure consisting of two, defective, one-dimensional photonic crystals [33].

In this chapter, we focus on aperiodic multilayer structures of alternating layers composed of silicon and silica above a tungsten substrate to produce narrowband, highly directional thermal emission for both TE and TM polarizations. One-dimensional layered structures without texturing are preferable to more complex two- and three-dimensional structures because of the relative ease and low cost of fabrication. Our narrowband, highly tunable infrared emitter exhibits highly narrow angular emittance. We achieve this emittance profile by utilizing a genetic optimization algorithm [14] to select each layer's thickness independently so that the structure is completely aperiodic. The choice of the fitness function proved crucial in obtaining structures with narrowband highly directional emittance. Such a device should have applications not only as a quasi-coherent radiation source, but also a gas-detection scheme which will be discussed.

The remainder of this chapter will be organized into three sections. The theory section, (II), will discuss the computational techniques used. The theory section is followed by the results,

(III), which is broken into three subsections. In the first subsection, (III.A) of the results, we investigate the properties of a genetic-algorithm optimized aperiodic design and compare them to a previously proposed resonant cavity design. A discussion of an emitter tuned to the Wien wavelength of a near maximum operating temperature for the structure follows in the next subsection, (III.B). Lastly, we discuss a structure designed for an application as the emitting portion of a low-cost carbon monoxide (CO) detector (III.C) and provide our conclusions in Sec. IV.

2.2 Theory

We envision a structure composed of infinite slabs of material of varying aperiodic thicknesses as depicted in Figure 2.1. Light is incident from air at an angle θ to the structure. Utilizing the transfer matrix method [34], we calculate the transmittance, reflectance, and absorbance of the structure for both TE and TM polarized light.We make use of experimental data for the wavelength-dependent indexes of refraction, both real and imaginary parts, for silica, silicon, and tungsten [35] for the calculations done in this chapter. Since the tungsten substrate is taken to be semi-infinite, the transmittance is identically zero, so that:

$$A_{\mathrm{TE/TM}}(\lambda,\theta) = 1 - R_{\mathrm{TE/TM}}(\lambda,\theta), \tag{2.1}$$

where $A_{\mathrm{TE/TM}}$ is the TE/TM absorbance, $R_{\mathrm{TE/TM}}$ is the TE/TM reflectance, and λ is the wavelength. While we only calculate absorbance, reflectance, and, in principle, transmittance, we make use of Kirchhoff's second law and conservation of energy to equate absorbance ($A_{\mathrm{TE/TM}}$) and emittance ($\epsilon_{\mathrm{TE/TM}}$) under thermal equilibrium [36] .

2.2.1 Fitness

We are interested in finding structures with highly directional and narrowband thermal emittance. We used a genetic optimization algorithm to determine the best structure's dimensions for varying numbers of layers at a given wavelength, λ_0. The genetic algorithm is an iterative optimization procedure, which starts with a randomly selected population of potential solutions, and gradually evolves toward improved solutions, via the application of the genetic

operators. These genetic operators are patterned after the natural selection process. In the initialization function, a population of chromosomes is created by random selection of values for the genes. The genetic algorithm then proceeds to iteratively generate a new population by the application of selection, crossover, and mutation operators.

More specifically, here we use the microgenetic algorithm. It has been shown that the microgenetic algorithm avoids premature convergence and shows faster convergence to the

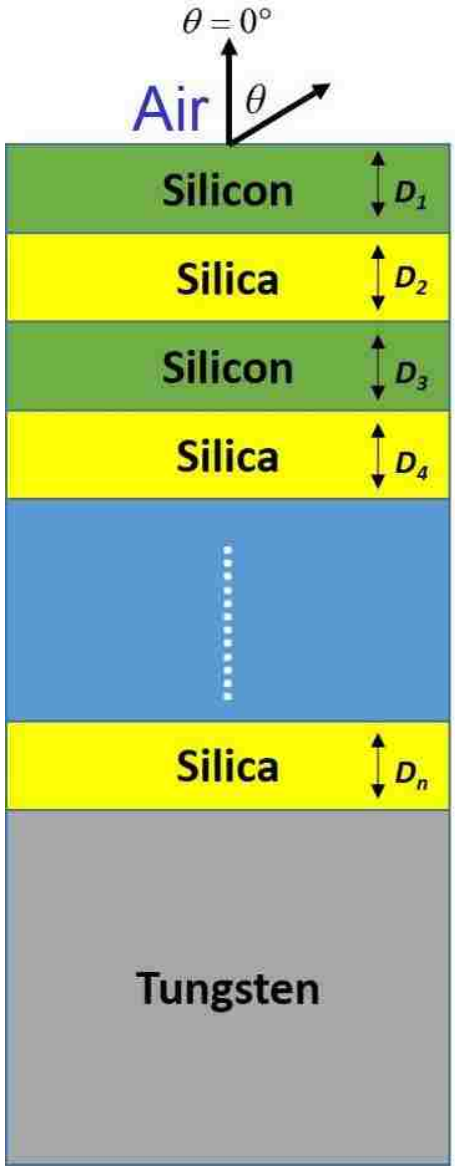

FIGURE 2.1: Schematic of structure optimized by genetic algorithm coupled to the transfer matrix code. Incident light at an angle θ to the normal of the surface of the structure enters the n-layer alternating structure of silicon and silica above a semi-infinite tungsten substrate.

near-optimal region compared to the conventional large-population genetic algorithm for multidimensional problems [13, 14, 15]. The microgenetic algorithm starts with a small random population which evolves and converges after a few generations. At this point, keeping the best individual from the previously converged generation, a new random population is chosen, and the evolution process restarts.

We use the tournament selection as the selection scheme in the genetic algorithm. In this method, a subpopulation of individuals is randomly chosen from the population and made to compete on the basis of their fitness values. The individual in the subpopulation with the highest fitness value wins the tournament, and is thus selected. The remaining members of the entire subpopulation are then put back into the general population, and the process is repeated. This selection scheme converges more rapidly and has a faster execution time compared to other competing schemes [17]. Once a pair of individuals is selected as parents, the basic crossover operator creates two offspring by combining the chromosomes of their parents. We use uniform crossover rather than single point crossover, as it has been found that microgenetic algorithm convergence is faster with the uniform crossover [17, 14]. An elitist strategy [18] is also employed, wherein the best individual from one generation is passed on to the next generation.

Specifically, we calculated the emittance of each structure as a function of angle for $0^\circ \leq \theta \leq 90^\circ$. We then minimized the fitness function, $F(\lambda_0)$,

$$F(\lambda_0) = \int_{0^\circ}^{90^\circ} \epsilon_{\text{Total}}(\lambda_0, \theta)\, d\theta, \tag{2.2}$$

subject to the constraint that $\epsilon_{\text{Total}}(\lambda_0, \theta = 0^\circ) \geq 0.95$. Here, $\epsilon_{\text{Total}}(\lambda_0, \theta) = [\epsilon_{\text{TE}}(\lambda_0, \theta) + \epsilon_{\text{TM}}(\lambda_0, \theta)]/2$. That is, we calculated the integral of the emittance over all angles θ at a given wavelength, λ_0, and minimized it subject to the constraint that the emittance at normal incidence was at least 95%. It is interesting to note that the fitness function that we use does not impose any constraints on the wavelength dependence of the emittance, since the

structures are optimized at a single wavelength; however, simply by minimizing the integral of the emittance over all angles at a single wavelength [as seen in Figure 2.2, for example], we also achieve narrowband emittance.

2.3 Results

In this section, we discuss three genetic algorithm optimized structures for use as thermal emitters. The first structure is optimized to operate at $\lambda_0 = 2.357$ μm for ease of comparison to a previously proposed resonant cavity design. The second structure is optimized to operate at the Wien wavelength corresponding to a near-maximum operating temperature for the materials used in the structure. Finally, the third structure discussed is optimized to operate at one of the molecular transition frequencies for CO for possible use in the emitting portion of an absorption spectroscopy detector.

2.3.1 Aperiodic Emitter

Using the transfer matrix method and genetic algorithm as outlined in Sec. II, we investigated the properties of the aperiodic one-dimensional structures. We chose $\lambda_0 = 2.357$ μm as a first example in the infrared wavelength range. For comparison, we define the angular full width at half maximum (FWHM) $\delta\theta_n$ for the n-layer structure, calculating the width about $\theta = 0°$ for which the emittance is larger than half of the maximum achieved value as seen in Figure 2.2. We also define the spectral FWHM $\delta\lambda_n$ for the n-layer structure, calculating the width about the wavelength at which we optimized the structure, λ_0, for which the emittance is larger than half of the maximum achieved value as seen in Figure 2.3.

We consider structures of six, eight, and sixteen layers composed of alternating layers of silicon and silica. In each case, we minimize the fitness function, $F(\lambda_0)$, [Equation 2.2] subject to the constraint that the normal incidence emittance $\epsilon_{\text{Total}}(\lambda_0, \theta = 0°) \geq 0.95$.

The optimized six-layer structure shows highly directional emittance with $\delta\theta_6 = 10.8°$ [Figure 2.2]. The optimized eight-layer structure improves upon this with $\delta\theta_8 = 7.2°$. The optimized sixteen-layer structure improves on the six-layer and eight-layer designs by nearly

a factor of four and more than a factor of two, respectively, having $\delta\theta_{16} = 2.7°$. We also compare the genetically optimized structures with a previously proposed design consisting of a periodic quarter-wavelength stack with a half-wavelength resonant cavity over a semi-infinite tungsten substrate [24], which will heretofore be referred to as the periodic design, having $\delta\theta_{\text{Periodic}} = 26°$, an angular FWHM of more than twice that of the six-layer optimized structure [Figure 2.2].

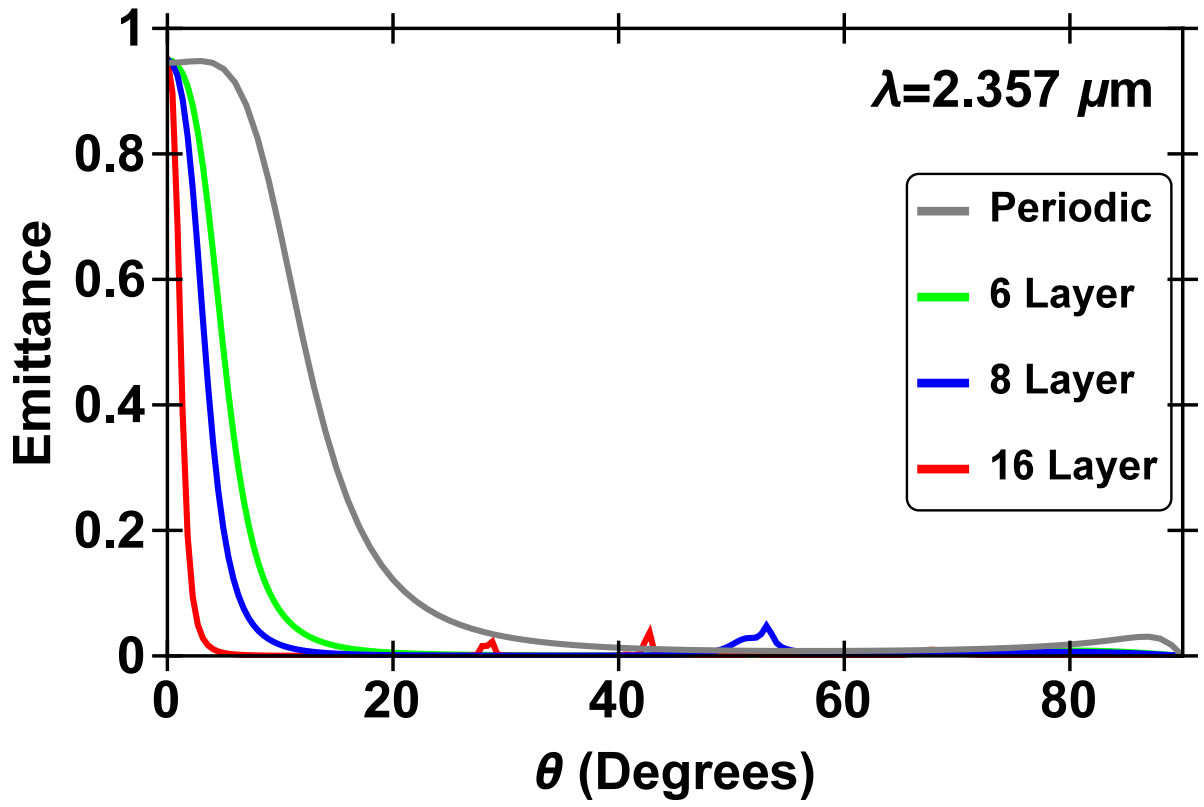

FIGURE 2.2: Emittance versus angle of an aperiodic multilayer structure of six, eight, and sixteen alternating layers of silicon and silica over a semi-infinite tungsten substrate. The structure is optimized such that the integral of the emittance over all angles for λ_0 =2.357 μm is minimized subject to the constraint that the emittance at normal incidence is greater than 0.95. The layer thicknesses of the optimized structure (in units of microns) are: {1.53, 0.46, 0.17, 0.36, 2.32, 2.0} for the six-layer structure, {2.21, 0.45, 1.83, 1.92, 1.18, 1.49, 0.19, 2.07} for the eight-layer structure, and {2.25, 1.28, 0.49, 1.95, 2.27, 1.14, 0.85, 2.03, 0.33, 1.94, 2.34, 2.28, 0.92, 2.36, 1.27, 1.18} for the sixteen-layer structure. The red dashed line depicts a four-layer quarter-wave stack of alternating layers of silicon and silica followed by a half-wavelength resonant cavity over a semi-infinite tungsten substrate tuned to λ_0 =2.357 μm.

Moving to the spectral FWHM, we note that the six-layer optimized structure has $\delta\lambda_6 = 8.8$ nm [Figure 2.3]. In comparison, the eight-layer optimized structure improves by more than a factor of two with $\delta\lambda_8 = 3.1$ nm. The sixteen-layer structure further improves this property by a factor of six over the eight-layer structure with a $\delta\lambda_{16} = 0.5$ nm. Compared to the genetic-algorithm-optimized aperiodic structures, the periodic structure exhibits much more broadband emittance, having $\delta\lambda_{\text{Periodic}} = 39.7$ nm [Figure 2.3]. These results can be found for at-a-glance comparison in Table 2.1.

In Figure 2.4 we show the profile of the electric field amplitude, normalized with respect to the field amplitude of the incident plane wave for the six-layer genetic-algorithm-optimized aperiodic structure. The structure is excited by a normally incident plane wave at the resonant wavelength. We observe a large resonant enhancement of the electric field inside the

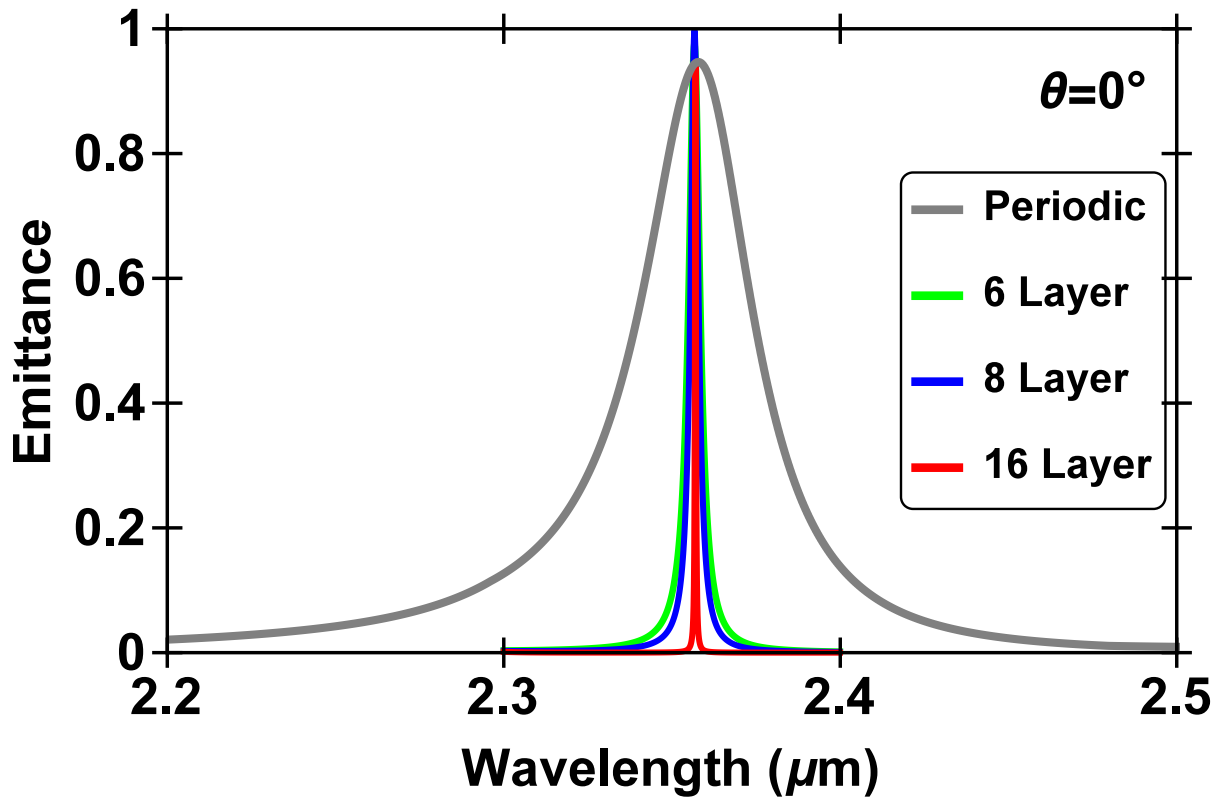

FIGURE 2.3: Emittance versus wavelength of the same structures described in Figure 2.2 at normal incidence.

TABLE 2.1: Angular FWHM $\delta\theta_n$ and spectral FWHM $\delta\lambda_n$ of the structures described in Figure 2.2.

n	$\delta\theta_n$	$\delta\lambda_n$
6	10.8°	8.8 nm
8	7.2°	3.1 nm
16	2.7°	0.5 nm
Periodic	26°	39.7 nm

silica layer adjacent to the tungsten substrate, which leads to greatly enhanced absorption in the substrate. Thus, one can think of this structure as a silica cavity sandwiched between a tungsten substrate and a partially reflective aperiodic multilayer stack composed of alternating layers of silicon and silica. We also found that, when the wavelength or the angle of

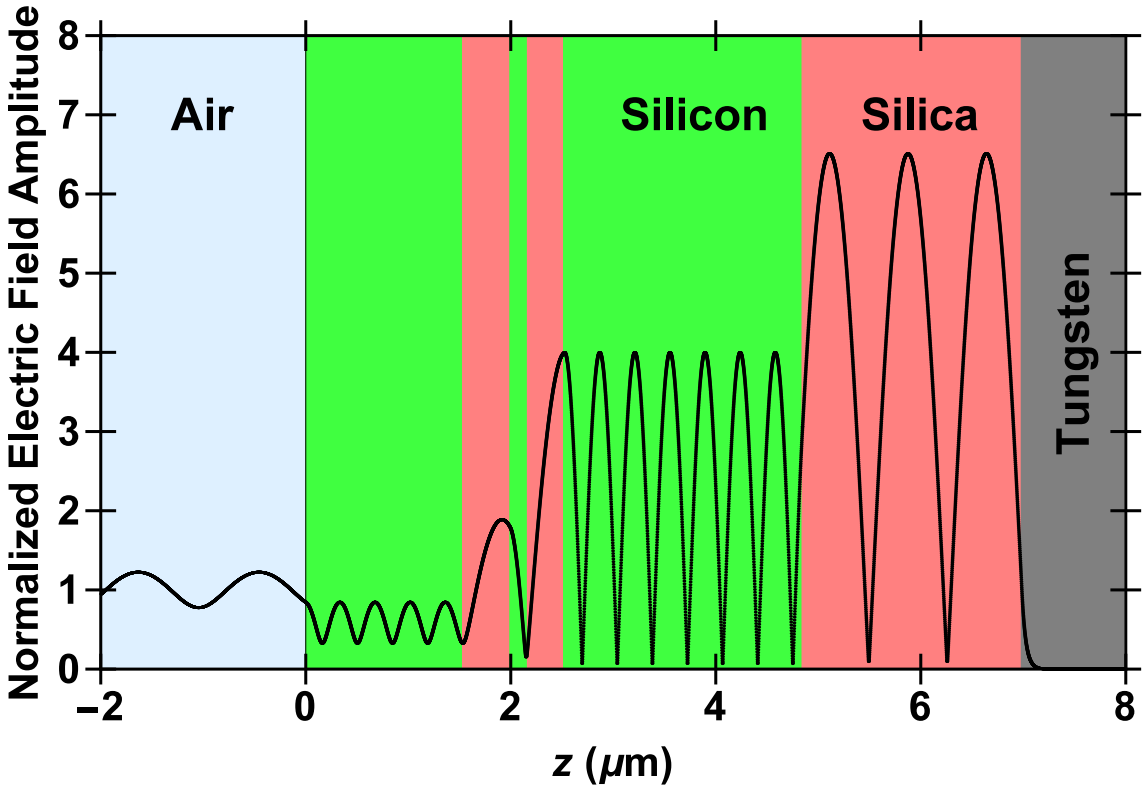

FIGURE 2.4: Profile of the electric field amplitude, normalized with respect to the field amplitude of the incident plane wave for the six-layer genetic-algorithm-optimized aperiodic structure described in Figure 2.2. The structure is excited by a normally incident plane wave at the resonant wavelength of $\lambda_0 = 2.357$ μm.

incidence are shifted away from the resonance, the field enhancement rapidly decreases. This is consistent with the narrowband, highly directional emittance of the structure (Figure 2.2).

Overall, the periodic structure exhibited both highly directional and narrowband emittance; however, even the six-layer genetic-algorithm-optimized aperiodic structure improved upon the directionality and increased the wavelength selectivity of the emittance, with the eight-layer and sixteen-layer structures further improving these features. As depicted in Figure 2.2, it is important to note there is a trend of increasing angular selectivity as the number of layers increases. In addition, we found that there is a decrease in the outlying emittance in the $\theta > 60°$ range as the number of layers increases. In Figure 2.3, a similar trend is seen: the wavelength selectivity of the emittance of the structure increases with the number of layers. Even the six-layer aperiodic structure shows vastly increased performance over the previously seen periodic design. The eight-layer aperiodic structure shows further increased

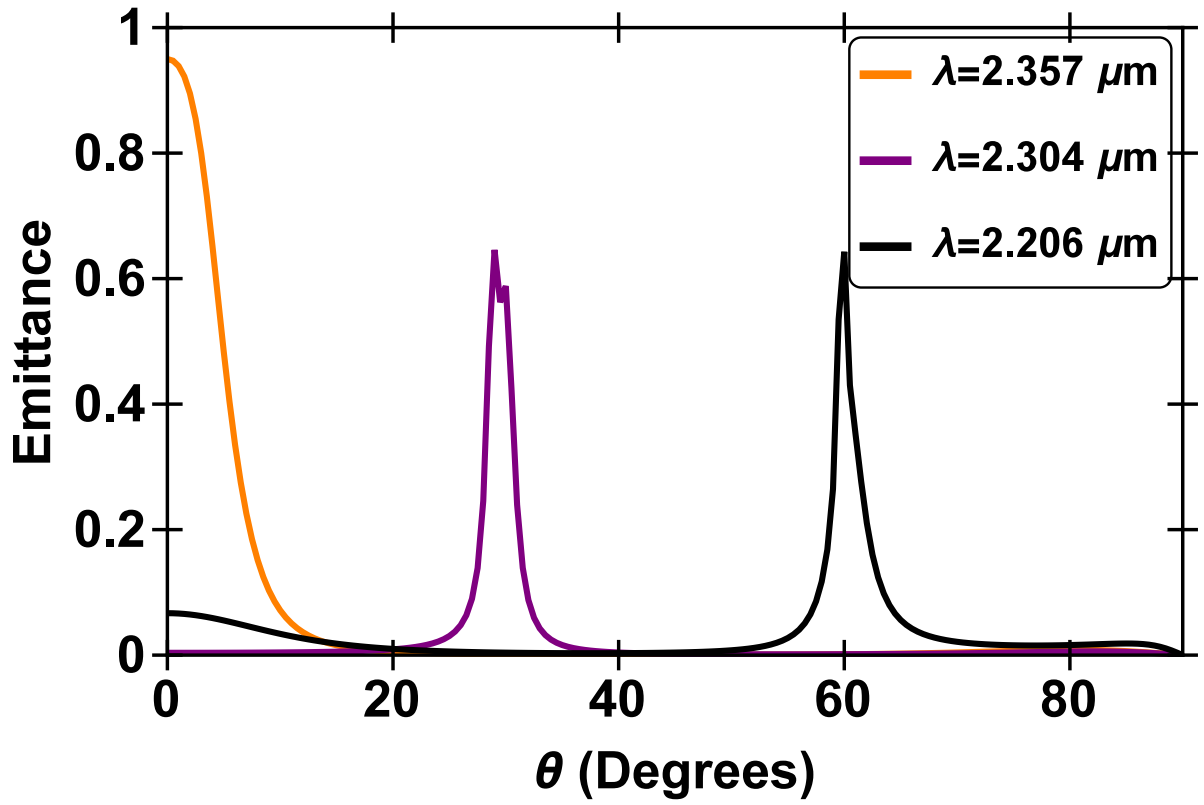

FIGURE 2.5: Angular emittance of the six-layer aperiodic structure described in Figure 2.2.

performance, and the sixteen-layer aperiodic structure exhibits both extreme angular and spectral selectivity.

We then investigated the off-normal behavior of the emittance for both the genetic-algorithm-optimized aperiodic structures [Figure 2.5] as well as the periodic structure [Figure 2.6]. Similar trends were seen in the off-normal emittance bands as were seen with the normal. We looked specifically at the emittance at 30° and 60° and selected the peak wavelength emitted at those angles. There is a trend that as the angle θ increases, the peak of the emittance shifts to shorter wavelengths. This is due to the fact that the phase accumulation inside each layer decreases as the angle of incidence increases. This decrease can be compensated for by decreasing the wavelength [37]. This trend can also be seen in Figure 2.7 where we show the emittance as a function of wavelength and angle for the six-layer genetic-algorithm-optimized aperiodic structure. Qualitatively, the periodic structure's peaks possess larger FWHM for

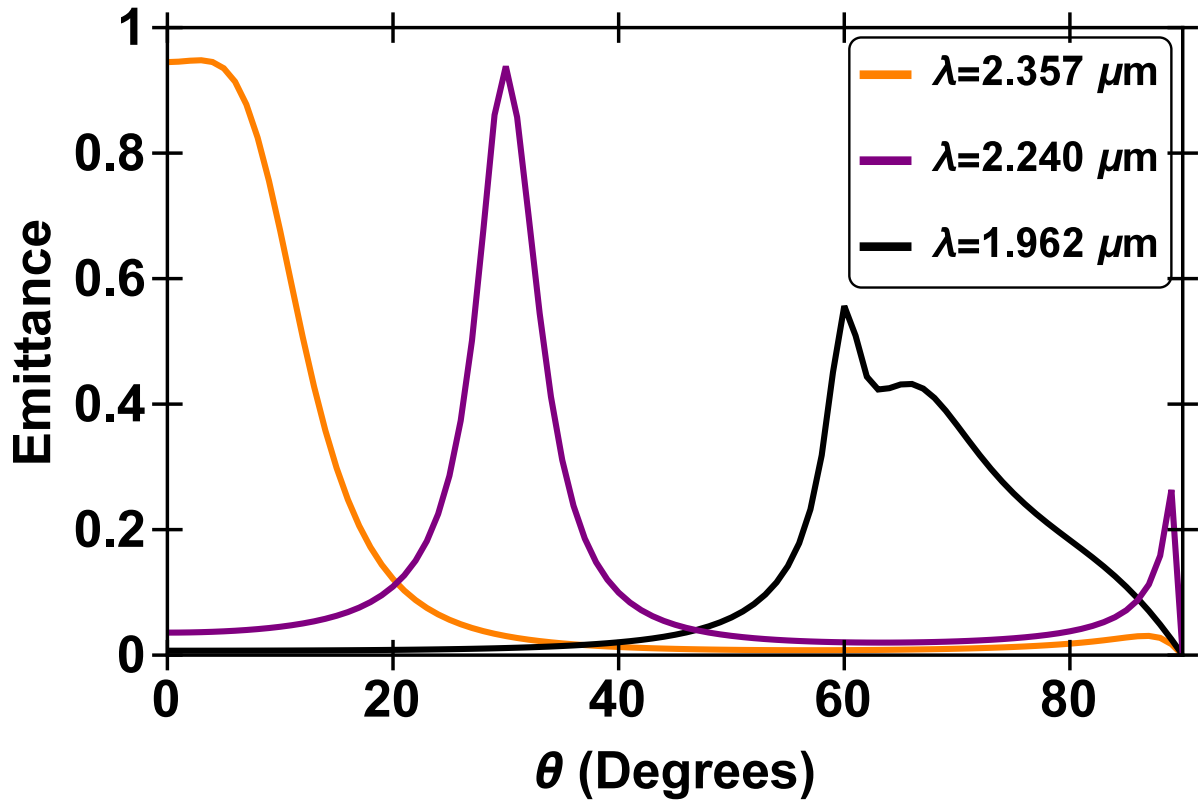

FIGURE 2.6: Angular emittance for the periodic structure described in Figure 2.2.

both wavelength and angular emittance peaks than the genetic-algorithm-optimized aperiodic structures. We also note that the genetic algorithm-optimized aperiodic structures' peaks shift more in angle with decreasing wavelength than do those of the resonant cavity design. This difference is related to the higher quality factor of the resonances, $Q = \lambda/\delta\lambda$, of the aperiodic structures, which leads to higher sensitivity to changes in angle of incidence.

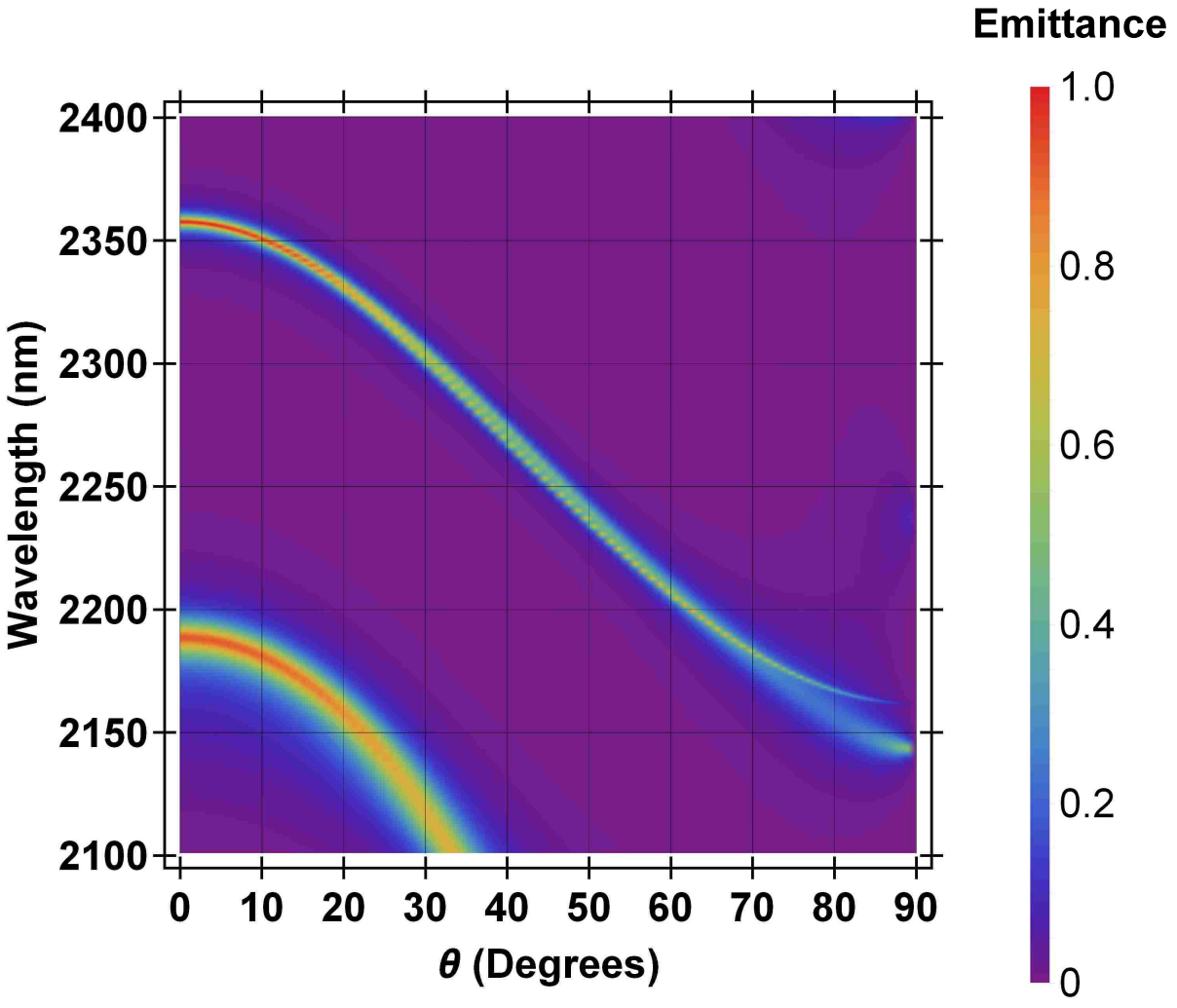

FIGURE 2.7: Emittance as a function of wavelength and angle for the six-layer genetic-algorithm-optimized aperiodic structure described in Figure 2.2.

2.3.2 Wien Wavelength

The Planck blackbody spectrum introduces temperature and wavelength dependence into the spectral radiance $B(\lambda, T)$ of a blackbody:

$$B(\lambda, T) = \frac{2hc^2}{\lambda^5} \frac{1}{e^{\frac{hc}{\lambda k_B T}} - 1}, \tag{2.3}$$

where h is Planck's constant, c is the speed of light, and k_B is the Stefan-Boltzman constant. In principle, the power spectrum $\mu(\lambda)$ for any material or structure with emittance $\epsilon(\lambda)$ is:

$$\mu(\lambda) = \epsilon(\lambda) B(\lambda, T). \tag{2.4}$$

Here, we seek to maximize such emittance while accounting for the melting points of the materials used. We can calculate the maximum of B as a function of wavelength by setting $\partial B / \partial \lambda = 0$. This results in the following equation:

$$\frac{x e^x}{e^x - 1} = 5, \tag{2.5}$$

where $x = hc/\lambda k_B T$. Once solved, Wien's displacement law is extracted:

$$\lambda_{\max} = \frac{hc}{x k_B T}, \tag{2.6}$$

where x is the solution of Equation 2.5, $x = 4.96511....$

Considering melting points for silicon, silica, and tungsten, silicon has the lowest melting point of 1690 K. Allowing a small safety margin, we reduce this temperature to 1500 K and make use of Wien's displacement law to calculate the appropriate wavelength for maximum power output to be $\lambda = 1.931$ μm. As before, we consider structures of six, eight, and sixteen layers composed of alternating layers of silicon and silica. In each case, we minimize the fitness function $F(\lambda_0)$, [Equation(2.2)], subject to the constraint that the normal incidence emittance $\epsilon_{\text{Total}}(\lambda_0, \theta = 0^\circ) \geq 0.95$.

We chose this wavelength and optimized the same six-, eight-, and sixteen-layer aperiodic structures for angular and wavelength selective emittance here. Again, as we saw in Figure 2.2

& Figure 2.3, the same trends appear in Figure 2.8 & Figure 2.9, with the six-layer structure showing a well-defined peak in both angular and wavelength space, the eight-layer structure improving upon what the six-layer offered, and the sixteen-layer further increasing angular and wavelength selectivity. More concretely, the six-layer structure offers a selective emitter, with a $\delta\theta_6 = 14.4°$ and $\delta\lambda_6 = 11.1$ nm. The eight-layer optimized structure performs better by nearly a factor of two with a $\delta\theta_8 = 8.1°$ and $\delta\lambda_8 = 3.2$ nm. The sixteen-layer optimized structure outperforms the eight-layer by another factor of two and is a full factor of four

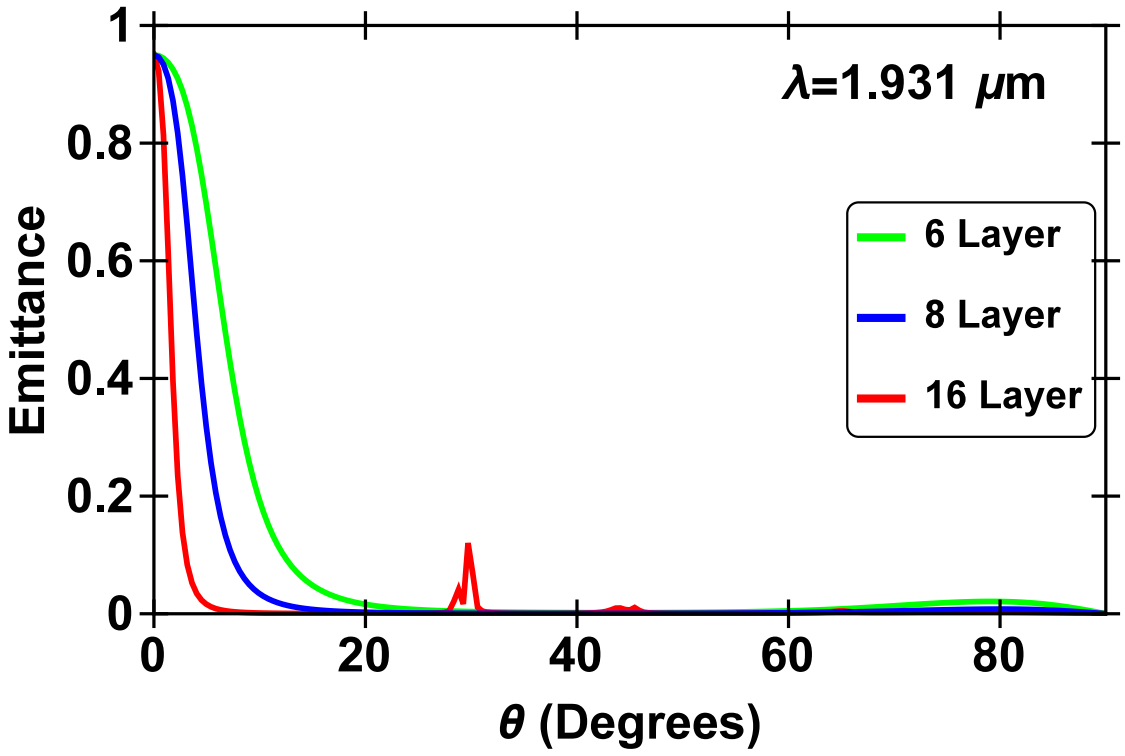

FIGURE 2.8: Emittance versus angle of an aperiodic multilayer structure of six, eight, and sixteen alternating layers of silicon and silica over a semi-infinite tungsten substrate. The structure is optimized such that the integral of the emittance for λ_0 =1.931 μm over all angles is minimized subject to the constraint that the emittance at normal incidence is greater than 0.95. The layer thicknesses of the optimized structure (in units of microns) are: {1.81, 0.36, 0.12, 1.83, 0.43, 1.09} for the six-layer structure, {1.81, 0.29, 0.72, 0.35, 0.72, 1.82, 0.72, 0.26} for the eight-layer structure, and {1.55, 0.9, 1.56, 1.63, 1.21, 1.62, 0.39, 1.24, 1.30, 0.34, 0.77, 1.87, 1.54, 0.23, 0.24, 0.24} for the sixteen-layer structure.

TABLE 2.2: Angular FWHM $\delta\theta_n$ and spectral FWHM $\delta\lambda_n$ of the structures described in Figure 2.8.

n	$\delta\theta_n$	$\delta\lambda_n$
6	14.4°	11.1 nm
8	8.1°	3.2 nm
16	3.6°	0.5 nm

better than the six-layer structure with a $\delta\theta_{16} = 3.6°$ and $\delta\lambda_{16} = 0.5$ nm. These results can be found for at-a-glance comparison in Table II.

2.3.3 Aperiodic Structure as the Emitting Portion of a Detector

Carbon Monoxide (CO) is a colorless, odorless, and tasteless gas that is poisonous to humans. One of the molecular resonances of CO occurs at $\lambda = 4.7$ μm [38]. Here, we consider

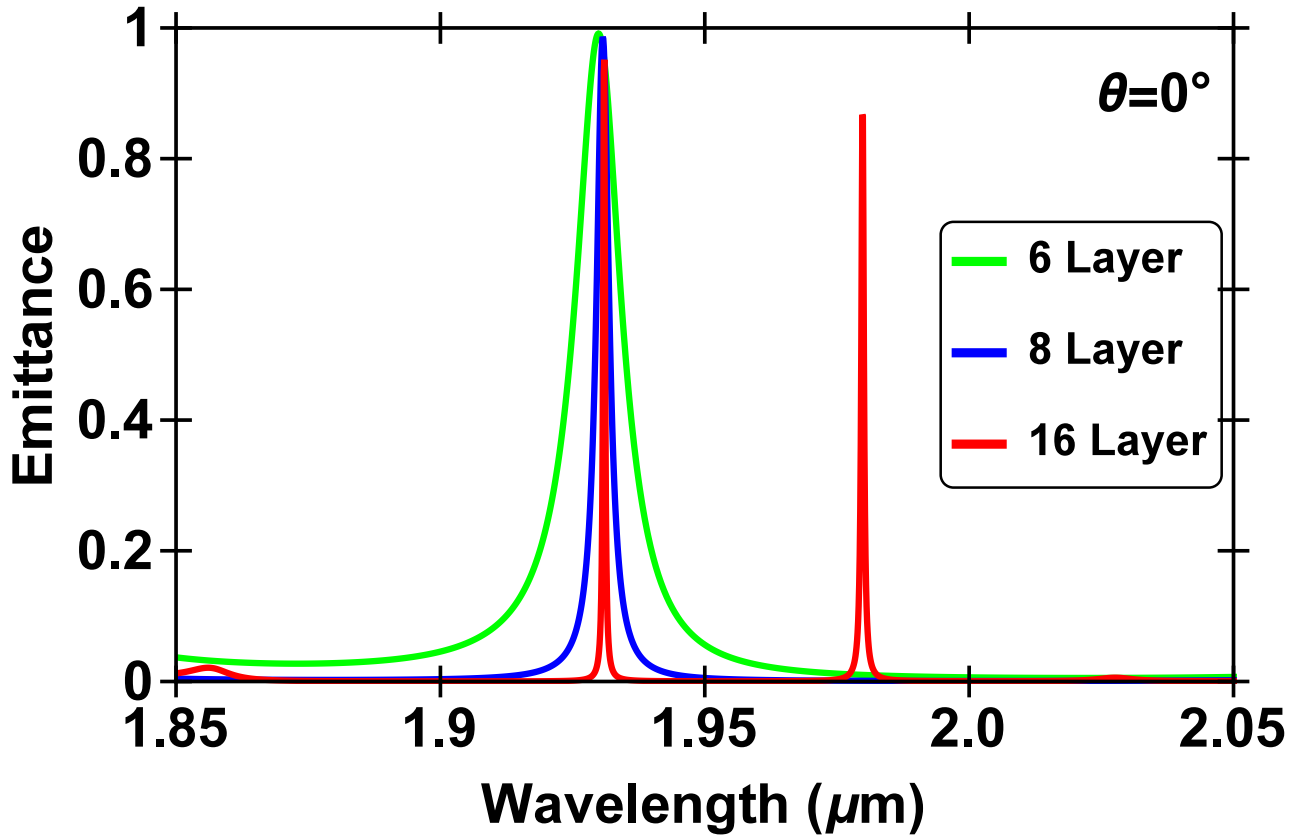

FIGURE 2.9: Emittance versus wavelength of the same aperiodic structures described in Figure 2.8 at normal incidence.

constructing the emitting portion of a low-cost detector for CO utilizing a quasi-coherent thermal source emitting at the transition frequency.

By heating the designed structure, light is emitted at one of the resonant frequencies of CO. Via absorption spectroscopy, one may use a detector which searches for dips in the intensity of the 4.7μm light which would signify an increase of concentration of CO in the air, thereby setting off the alarm.

With this application in mind, we chose $\lambda_0 = 4.7$ μm, and we designed optimized structures. These results are depicted in Figure 2.10 & Figure 2.11. Again, the same trends are found that increasing the number of layers both increases the angular and wavelength selectivity. At 4.7μm, the selectivity of each the six-, eight-, and sixteen-layer structures was notably higher than at previously optimized wavelengths.

At this wavelength, the six-layer structure performed a factor of two better than the structure optimized for $\lambda_0 = 1.931$ μm with a $\delta\theta_6 = 8.2^\circ$ and $\delta\lambda_6 = 4.4$ nm. The eight-layer structure showed marginal improvement over the six-layer with $\delta\theta_8 = 5.4^\circ$ and $\delta\lambda_8 = 2.2$ nm; however, the sixteen-layer optimized structure showed more than a factor of three overall improvement, with a $\delta\theta_{16} = 1.8^\circ$ and $\delta\lambda_{16} = 0.2$ nm. These results can be found for at-a-glance comparison in Table III.

TABLE 2.3: Angular FWHM $\delta\theta_n$ and spectral FWHM $\delta\lambda_n$ of the structures described in Figure 2.10.

n	$\delta\theta_n$	$\delta\lambda_n$
6	8.2°	4.4 nm
8	5.4°	2.2 nm
16	1.8°	0.2 nm

2.4 Conclusion

We have designed a series of aperiodic structures that have been optimized to produce narrow-angular emittance profiles and also display narrow-wavelength emittance. We compared the angular and spectral FWHM of the genetic-algorithm-optimized aperiodic struc-

tures to the ones of the resonant cavity design. We have demonstrated that angular selectivity increases with the number of layers and noticed a strong correlation between angular selectivity and spectral selectivity. We have presented an additional structure that has a use as a quasi-coherent emitter optimized to operate at the Wien wavelength corresponding to a near-maximum operating temperature for a silica-silicon structure. Finally, we have outlined a low-cost method for constructing the emitting portion of an absorption spectroscopy detector for CO.

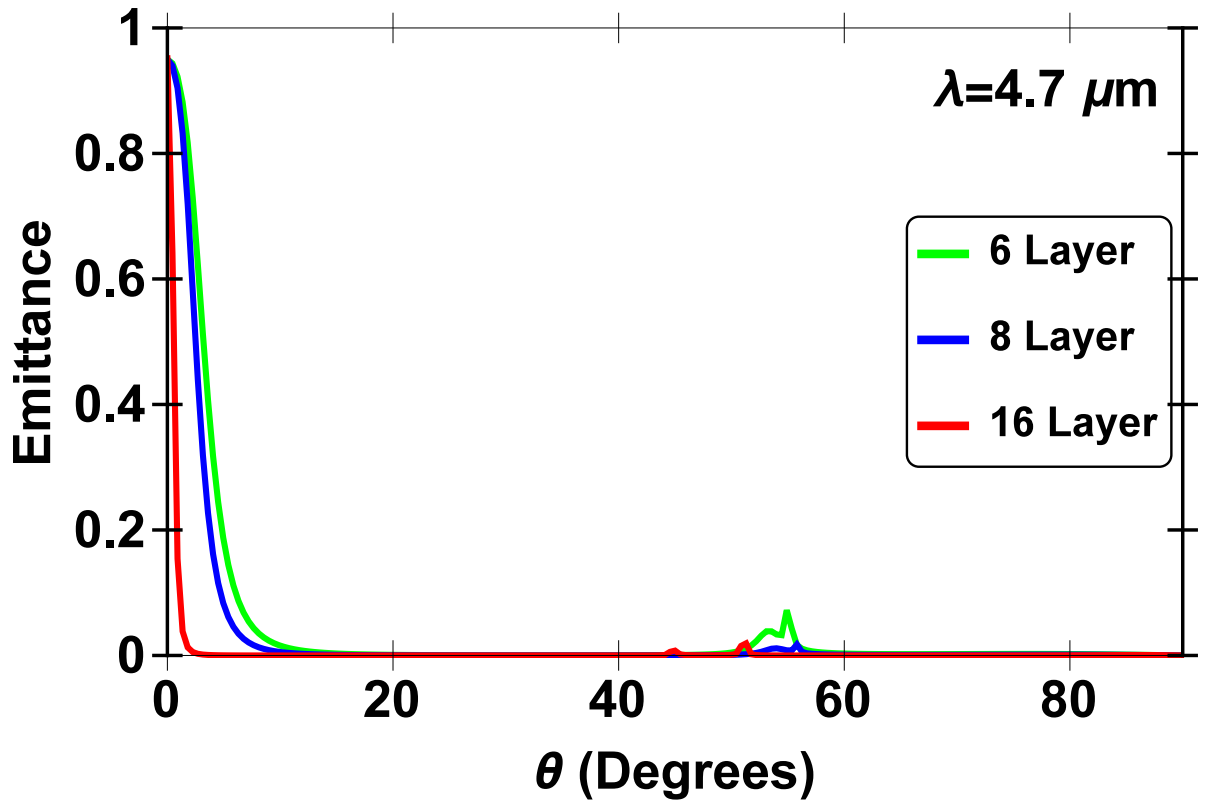

FIGURE 2.10: Emittance versus angle of an aperiodic multilayer structure of six, eight, and sixteen alternating layers of silicon and silica over a semi-infinite tungsten substrate. The structure is optimized such that the integral of the emittance for λ =4.7 μm over all angles is minimized subject to the constraint that the emittance at normal incidence is greater than 0.95. The layer thicknesses of the optimized structure (in units of microns) are: {3.77, 0.9, 3.76, 4.49, 4.62, 3.16} for the six-layer structure, {3.75, 0.91, 2.40, 4.53, 4.51, 1.28, 3.93, 2.94} for the eight-layer structure, and {4.47, 0.88, 0.39, 1.02, 0.35, 0.91, 1.14, 4.00, 2.03, 2.39, 1.72, 3.38, 0.34, 0.99, 3.04, 4.15} for the sixteen-layer structure.

As final remarks, we have discussed several specific structures that can be tuned to emit at a wide variety of wavelengths. We note that due to the wavelength dependence of the dielectric permittivity of the materials used in the design, one cannot simply scale the layer thicknesses by a factor to scale the operating wavelength by that same factor. In other words, the optimized designs are not scale invariant, so the optimization process must be carried out at the new desired wavelength. In all cases, we found that the optimal structures were unique. In other words, if the stochastic genetic optimization process is repeated, it converges to the same result. Finally, for structures designed as emitters, there is a question of how performance will change as temperature is varied. It is known that temperature variations tend to primarily modify the material losses [39]. We found that, if the material losses change, we can still use the same genetic algorithm optimization approach to design highly

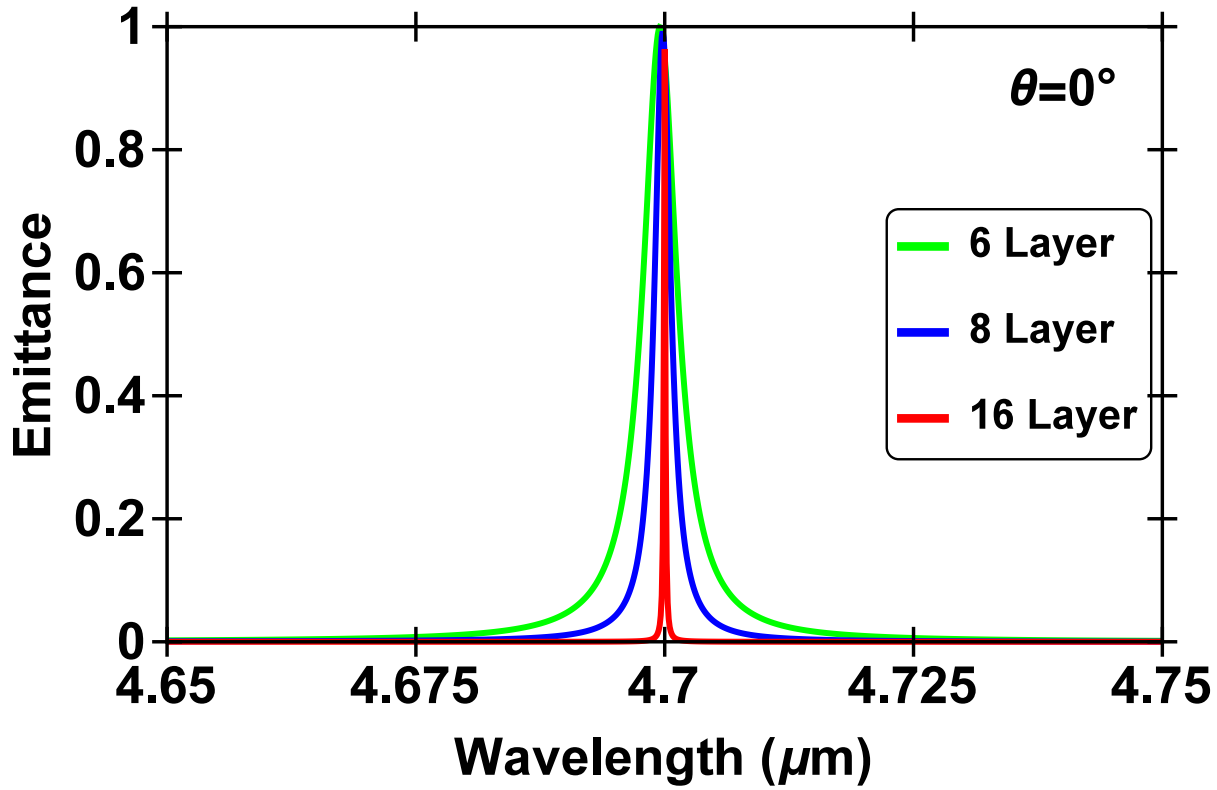

FIGURE 2.11: Emittance versus wavelength of the same aperiodic structures described in Figure 2.10 at normal incidence.

directional, narrowband emitters. Thus, our approach can be used to design structures at a desired operating temperature. We also found that the effect of layer thickness variations due to thermal expansion on emittance can be neglected [39].

This research was supported by the National Science Foundation (Award Nos. 1102301, 1263236, 0968895), and a Fund for Innovation in Engineering Research (FIER) grant from the Louisiana State University College of Engineering. Jonathan P. Dowling wishes to also acknowledge support from the Air Force Office of Scientific Research and the Army Research Office.

Chapter 3

Optimized Aperiodic Multilayer Structures for Use as Narrow-Angular Absorbers

In this chapter, we investigate aperiodic multilayer structures for use as narrow-angular absorbers. The layer thicknesses and materials are optimized using a genetic global optimization algorithm coupled to a transfer matrix code to maximize the angular selectivity in the absorptance at a single or multiple wavelengths. We first consider structures composed of alternating layers of tungsten and silicon or silica, and find that it is not possible to achieve angular selectivity in the absorptance with such structures. We next consider structures composed of alternating layers of silicon and silica, and show that when optimized they exhibit high angular selectivity in absorptance. In addition, as the angular selectivity in absorptance increases, the wavelength range of high angular selectivity also decreases. Optimizing the material composition of the multilayer structures, in addition to optimizing the layer thicknesses, leads to marginal improvement in angular selectivity. Finally, we show that by optimizing the absorptance of the multilayer structures at multiple wavelengths, we can obtain structures exhibiting almost perfect absorptance at normal incidence and narrow angular width in absorptance at these wavelengths. Similar to the structures optimized at a single wavelength, the wavelength range of high angularly selective absorptance is narrow.[1]

3.1 Introduction

The absorptance properties of materials and structures have been widely investigated in recent years. Bulk materials, such as tungsten, exhibit broadband and broad-angle absorption spectra which vary from material to material. However, it has been demonstrated that the absorption spectra of bulk materials can be drastically changed by using multilayer structures[40], textured surfaces, or other three dimensional constructions[41, 42]. Several

[1]Part of this chapter previously appeared as C. H. Granier, F. O. Afzal, S. G. Lorenzo, M. Reyes Jr., J. P. Dowling, and G. Veronis, "Optimized aperiodic multilayer structures for use as narrow-angular absorbers," J. Appl. Phys. **116** 243101 (2014). It is reprinted by permission of the American Institute of Physics (AIP). See the permission letter in the Appendix.

different structures with modified absorptance properties have been investigated, including metallic gratings[43, 44], metallic and semiconductor photonic crystals[45, 46, 47], periodic grooves[48], and nano-antennae[49]. The use of metamaterials has also been investigated as a possible method for tailoring the absorptance characteristics.[30] Developing such structures that have unusual absorption characteristics in the optical wavelength range is important for many applications such as photovoltaics,[50, 51, 20] control of thermal radiation,[52, 53] photodetectors,[54, 55] and chemical sensing[56, 46].

Most related efforts have been focused on developing structures with wide-angle near-perfect absorption in either a narrow or a broad wavelength range [57, 58, 59, 60, 61, 62, 63, 64, 65, 66]. However, structures which exhibit angular selectivity in absorptance are also investigated because of their many potential applications [67, 68]. In particular, in solar thermophotovoltaics solar radiation is absorbed by an intermediate absorber, which then emits thermal radiation towards a solar cell. Solar thermophotovoltaic cells are capable of achieving theoretical efficiency which far exceeds the Shockley-Queisser limit when a single-junction cell is directly exposed to sunlight [20, 8]. In order to approach such efficiency, however, there are very important constraints on the properties of the intermediate absorber. For efficient solar thermophotovoltaic systems which do not employ sunlight concentration, the intermediate absorber must exhibit broadband angular selectivity. More specifically, it must provide near-perfect absorption in a narrow angular range, corresponding to the solid angle subtended by the Sun, over the entire solar spectrum.[20, 8, 69] Efficient solar thermophotovoltaic systems must have relatively high temperature [69]. From the Earth's surface, the solid angle subtended by the Sun is very small. However, a conventional planar surface emits radiation isotropically in all 2π steradians. Due to this angular mismatch, the planar surface reaches thermal equilibrium at a much lower temperature than the Sun's temperature. Angular selectivity in the absorption of the intermediate absorber is therefore highly desired in the case of no sunlight concentration [8, 69], since then we can avoid the loss of energy by

the radiation of the intermediate radiator outside of the solid angle subtended by the Sun, a process which cools the absorber. It was also recently demonstrated that it is possible to design structures which exhibit broadband angular selectivity in transmission by tailoring the overlap of the band gaps of multiple photonic crystals, so as to preserve the characteristic Brewster modes in a broad wavelength range [70].

In this chapter, we investigate one-dimensional multilayer aperiodic structures for use as narrow-angular absorbers. It has been demonstrated that multilayer structures can tailor the absorptance spectra of bulk materials.[23] In many cases a multilayer structure may provide spectra-altering properties similar to that of more complex and harder-to-fabricate two- or three-dimensional structures. Here, we optimize the layer thicknesses and materials using a genetic global optimization algorithm coupled to a transfer matrix code to maximize the angular selectivity in the absorptance at a single or multiple wavelengths. We first consider structures composed of alternating layers of tungsten and silicon or silica over a tungsten substrate. We find that, due to the high absorption of tungsten, it is not possible to achieve angular selectivity in the absorptance with such structures. We next consider structures composed of alternating layers of silicon and silica. Unlike the structures containing tungsten, the optimized silicon-silica structures exhibit high angular selectivity in absorptance at the wavelength at which they are optimized. However, as the angular selectivity in absorptance increases, the wavelength range of high angular selectivity decreases. We then consider optimizing the material composition of the multilayer structures, in addition to optimizing the layer thicknesses, and find that this approach leads to marginal improvement in angular selectivity when compared to the silicon-silica structures. Finally, we investigate optimizing the absorptance of the multilayer structures at multiple wavelengths. We find that with this approach we can obtain structures exhibiting almost perfect absorptance at normal incidence and narrow angular width in absorptance at these wavelengths. However, similar

to the structures optimized at a single wavelength, the wavelength range of high angularly selective absorptance is narrow.

We previously showed that optimized aperiodic multilayer structures can lead to narrow-band, highly directional thermal infrared emitters [71]. In this work, structures are designed to operate in the visible. We note that the properties of the materials used are very different in these two wavelength ranges. Silicon is essentially lossless in the infrared, while it is quite lossy in the visible. As a result, the mechanisms that lead to high angular selectivity in absorptance are very different. In the infrared designs all the power is absorbed in the tungsten substrate[71]. In the visible designs presented in this work only a portion of the power is absorbed in the substrate. In fact, in some of the designs almost no power is absorbed in the substrate. One can think of such structures as lossy multilayer resonators which are almost perfectly impedance matched to air. In this work, we also show that it is not possible to achieve angular selectivity in the absorptance with structures composed of alternating layers of metals, such as tungsten, and dielectrics due to the high material loss of metals. In addition, we investigate the effect of optimizing the material composition of multilayer structures, in addition to optimizing the layer thicknesses. Finally, we show that with the proposed aperiodic structures it is possible to achieve almost perfect absorptance at normal incidence and narrow angular width in absorptance at multiple closely-spaced tunable wavelengths.

The remainder of this manuscript is divided into three sections. The computational techniques used will be discussed in Section II. The results are described in Section III, which is subdivided into four subsections. The first subsection, (III.A) discusses the results of genetic-algorithm optimized structures composed of tungsten and silicon as well as tungsten and silica. Subsection III.B presents the results of genetic-algorithm optimized silicon-silica structures for use as angular selective absorbers. In Subsection III.C, we investigate optimizing the material composition of the multilayer structures, in addition to optimizing the

layer thicknesses. Subsection III.D presents genetic-algorithm-optimized aperiodic structures composed of alternating layers of silicon and silica with narrow angular absorptance at two wavelengths (a narrow-angular, bichromatic absorber). Our conclusions are summarized in Section IV.

3.2 Theory

We model an aperiodic structure composed of infinite slabs of material of varying thicknesses as depicted in Figure 3.1. Light is incident from air at an angle θ to the structure. Utilizing the transfer matrix method [34], we calculate the transmittance, reflectance, and absorptance of the structure for both TE (transverse electric) and TM (transverse magnetic) polarized light. We make use of experimental data for the wavelength-dependent indexes of refraction, both real and imaginary parts, for silicon carbide, silica, silicon, and tungsten [35] for the calculations done in this chapter. These materials are commonly used in applications related to engineering the absorptance properties of different structures [24, 20], and have high melting points. In addition, silicon and silica provide a high index contrast which is useful for engineering the photonic band structure. It is important to note that in the visible range of wavelengths, both silica and silicon carbide are almost lossless. Since the tungsten substrate is taken to be semi-infinite, the transmittance is identically zero, so that:

$$A_{\mathrm{TE/TM}}(\lambda, \theta) = 1 - R_{\mathrm{TE/TM}}(\lambda, \theta), \tag{3.1}$$

where $A_{\mathrm{TE/TM}}$ is the TE/TM absorptance, $R_{\mathrm{TE/TM}}$ is the TE/TM reflectance, and λ is the wavelength.

We are interested in finding structures which are highly absorbing for normally incident light and also exhibit highly directional absorptance.

We use a genetic optimization algorithm to determine the best structure's dimensions for varying numbers of layers at a given wavelength λ_0. The implementation of the genetic algorithm that we use has been realized in-house. A genetic algorithm is an iterative optimization procedure, which starts with a randomly selected population of potential solutions,

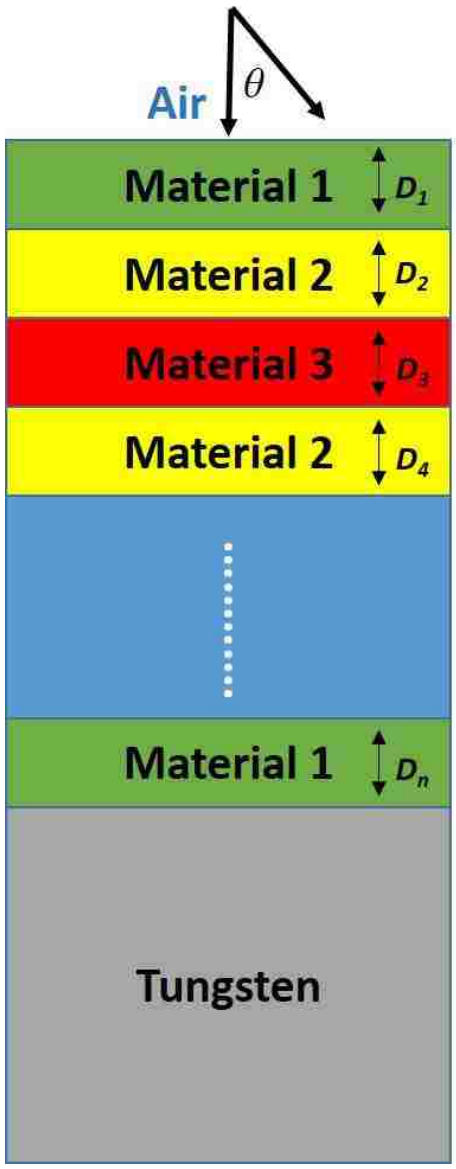

FIGURE 3.1: Schematic of aperiodic structure optimized by genetic algorithm coupled to the transfer matrix code. Incident light at an angle θ to the normal of the surface of the structure enters the n-layer structure comprised of various materials above a semi-infinite tungsten substrate.

and gradually evolves toward improved solutions, via the application of the genetic operators. These genetic operators are patterned after the natural selection process. In the initialization function, a population of chromosomes is created by random selection of values for the genes. The genetic algorithm then proceeds to iteratively generate a new population by the application of selection, crossover, and mutation operators.

More specifically, here we use the microgenetic algorithm. It has been shown that the microgenetic algorithm avoids premature convergence and shows faster convergence to the near-optimal region compared to the conventional large-population genetic algorithm for multidimensional problems [13, 14, 15]. The microgenetic algorithm starts with a small random population which evolves and converges after a few generations. At this point, keeping the best individual from the previously converged generation, a new random population is chosen, and the evolution process restarts.

We use the tournament selection as the selection scheme in the genetic algorithm. In this method, a subpopulation of individuals is randomly chosen from the population and made to compete on the basis of their fitness values. The individual in the subpopulation with the highest fitness value wins the tournament, and is thus selected. The remaining members of the entire subpopulation are then put back into the general population, and the process is repeated. This selection scheme converges more rapidly and has a faster execution time compared to other competing schemes [72]. Once a pair of individuals is selected as parents, the basic crossover operator creates two offspring by combining the chromosomes of their parents. We use uniform crossover rather than single point crossover, as it has been found that microgenetic algorithm convergence is faster with the uniform crossover [14, 72]. An elitist strategy is also employed, wherein the best individual from one generation is passed on to the next generation.

Specifically, for the structures discussed in Subsections III.A, III.B, and III.C, we calculate the absorptance of each structure as a function of angle for $0^\circ \leq \theta \leq 90^\circ$ at wavelength λ_0. We then minimize the fitness function, $F(\lambda_0)$,

$$F(\lambda_0) = \int_0^{\frac{\pi}{2}} A_{\mathrm{Total}}(\lambda_0, \theta)\, d\theta, \tag{3.2}$$

subject to the constraint that $A_{\mathrm{Total}}(\lambda_0, \theta = 0^\circ) \geq A_{\mathrm{min}}$. Here, $A_{\mathrm{Total}}(\lambda_0, \theta) = [A_{\mathrm{TE}}(A_0, \theta) + A_{\mathrm{TM}}(\lambda_0, \theta)]/2$. That is, we calculate the integral of the absorptance over all angles θ at a

given wavelength, λ_0, and minimize it subject to the constraint that the absorptance at normal incidence is at least $A_{\min}$.

3.3 Results

In this section, we discuss genetic-algorithm-optimized structures for use as directional absorbers. Each structure is optimized for angular selectivity in an attempt to find a broadband, narrow-angle absorber. The structures discussed in Subsections III.A, III.B, and III.C are optimized at $\lambda_0 = 550$ nm, roughly the center of the visible range. The structure discussed in Subsection III.D is optimized to operate as a narrow-angular, bichromatic absorber. It is optimized at both $\lambda_1 = 450$ nm and $\lambda_2 = 550$ nm, which correspond to indigo and green light, respectively, in the visible range.

3.3.1 Tungsten-Silicon and Tungsten-Silica Structures

Using the transfer matrix method and genetic algorithm as outlined in Sec. II, we investigate the properties of the aperiodic one-dimensional structures. We choose $\lambda_0 = 550$ nm at the center of the visible spectrum as the wavelength at which to optimize angular selectivity of the absorptance.

First, we consider structures of six, eight, and sixteen layers composed of alternating layers of tungsten and silicon over a semi-infinite tungsten substrate. In each case, we minimize the fitness function, $F(\lambda_0)$, [Equation (3.2)] subject to the constraint that the normal incidence absorptance, $A_{\text{Total}}(\lambda_0, \theta) \geq A_{\min} = 0.90$. For comparison of the structures, we define the angular full width at half maximum (FWHM), $\delta\theta_n$, for the n-layer structure, calculating the width about $\theta = 0^\circ$ for which the absorptance is larger than half of the maximum achieved value as seen in Figure 3.2. We also define the spectral FWHM, $\delta\lambda_n$, for the n-layer structure, calculating the width about the wavelength at which we optimized the structure, λ_0, for which the absorptance is larger than half of the maximum achieved value as seen in Figure 3.3. These results for the tungsten-silicon structure are found in Table 3.1.

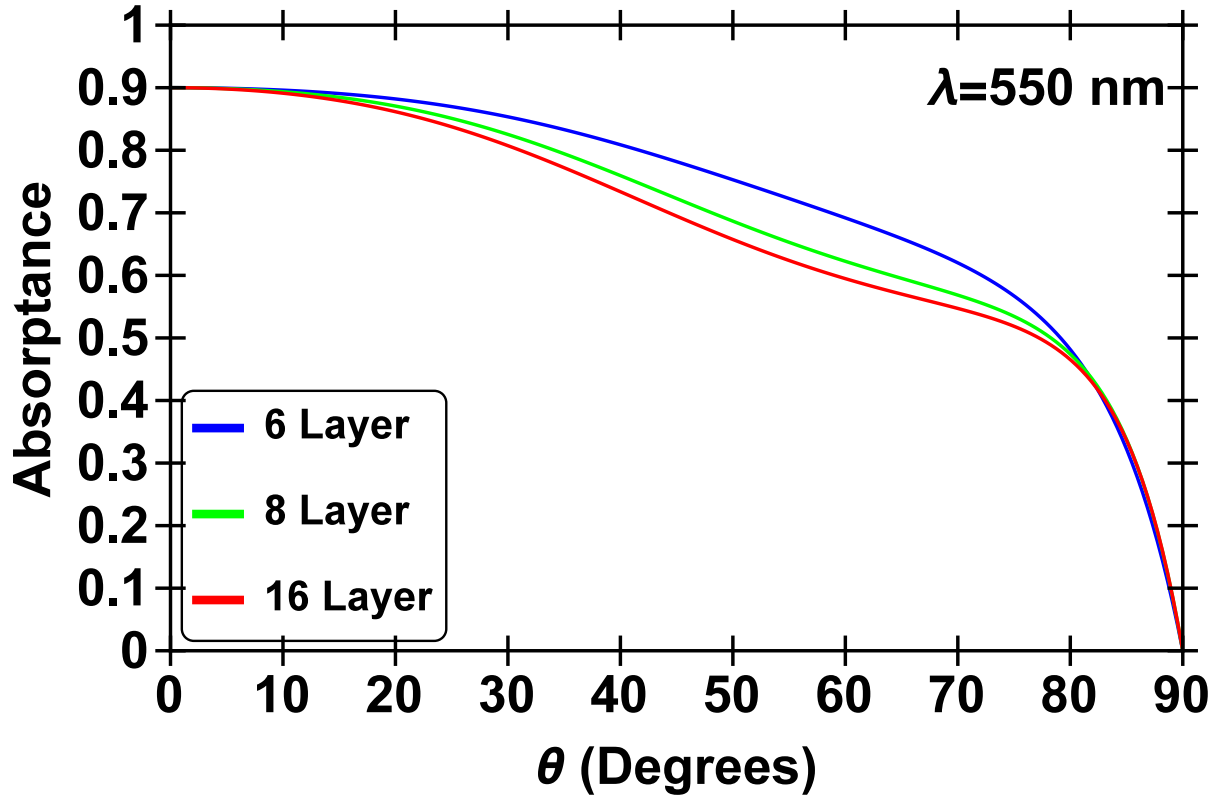

FIGURE 3.2: Absorptance versus angle of an optimized, aperiodic multilayer structure of six, eight, and sixteen alternating layers of tungsten and silicon over a semi-infinite tungsten substrate. The structure is optimized such that the integral of the absorptance over all angles for $\lambda_0 = 550$nm is minimized subject to the constraint that the absorptance at normal incidence is greater than 90% ($A_{\text{min}} = 0.90$). The layer thicknesses of the optimized tungsten-silicon structures (in units of nanometers) are: {0, 222, 17, 117, 34, 511} for the six-layer structure, {0, 357, 17, 51, 18, 48, 30, 313} for the eight-layer structure, and {0, 166, 0, 37, 0, 154, 17, 51, 17, 56, 15, 50, 26, 43, 34, 443} for the sixteen-layer structure. It is important to note that, for some layers, the optimized thickness was found to be zero. We found that for the opimized tungsten-silicon structures the top layer, which is adjacent to air, is always silicon.

TABLE 3.1: Angular FWHM $\delta\theta_n$ and spectral FWHM $\delta\lambda_n$ of the tungsten-silicon structures described in Figure 3.2.

n	$\delta\theta_n$	$\delta\lambda_n$
6	161.4°	70.4 nm
8	161.6°	42.6 nm
16	161.8°	45.4 nm

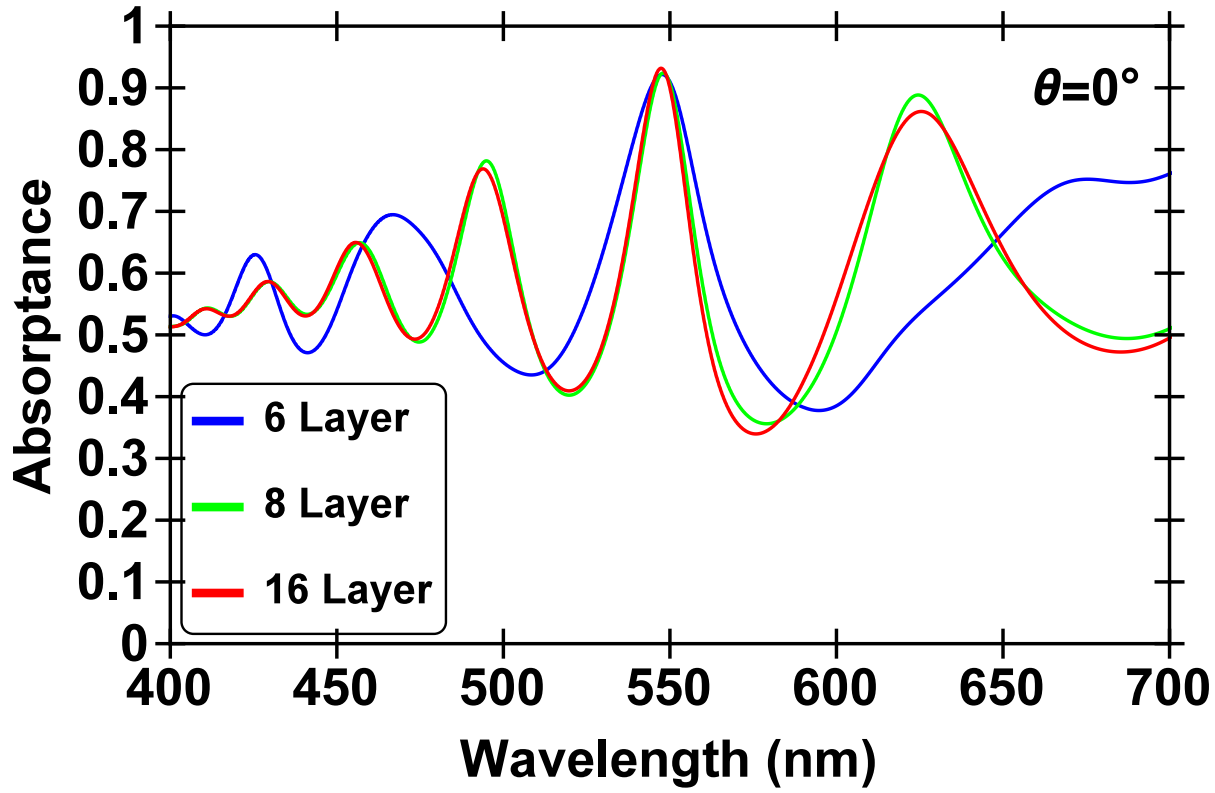

FIGURE 3.3: Absorptance versus wavelength of the same structures described in Figure 3.2 at normal incidence.

We observe that the genetic-algorithm-optimized tungsten-silicon structures do not exhibit angular selectivity [Figure 3.2]. In addition, the structures exhibit no wavelength-selectivity and the absorptance is relatively broadband in nature. The structures exhibit absorptance of more than 50% in a broad wavelength range [Figure 3.3]. There is very little change in the angular FWHM, $\delta\theta_n$, of the respective silicon-tungsten genetic-algorithm-optimized structures with increasing number of layers (Table 3.1). Overall, the silicon-tungsten material combination fails to provide angular selectivity and increasing number of layers does not improve the angular selectivity. This is due to the high absorption of tungsten. In Figure 3.7, we show the profile of the electric field amplitude, normalized with respect to the field amplitude of the incident plane wave for the six-layer genetic-algorithm-optimized aperiodic tungsten-silicon structure. The structure is excited by a normally incident plane wave at the wavelength of

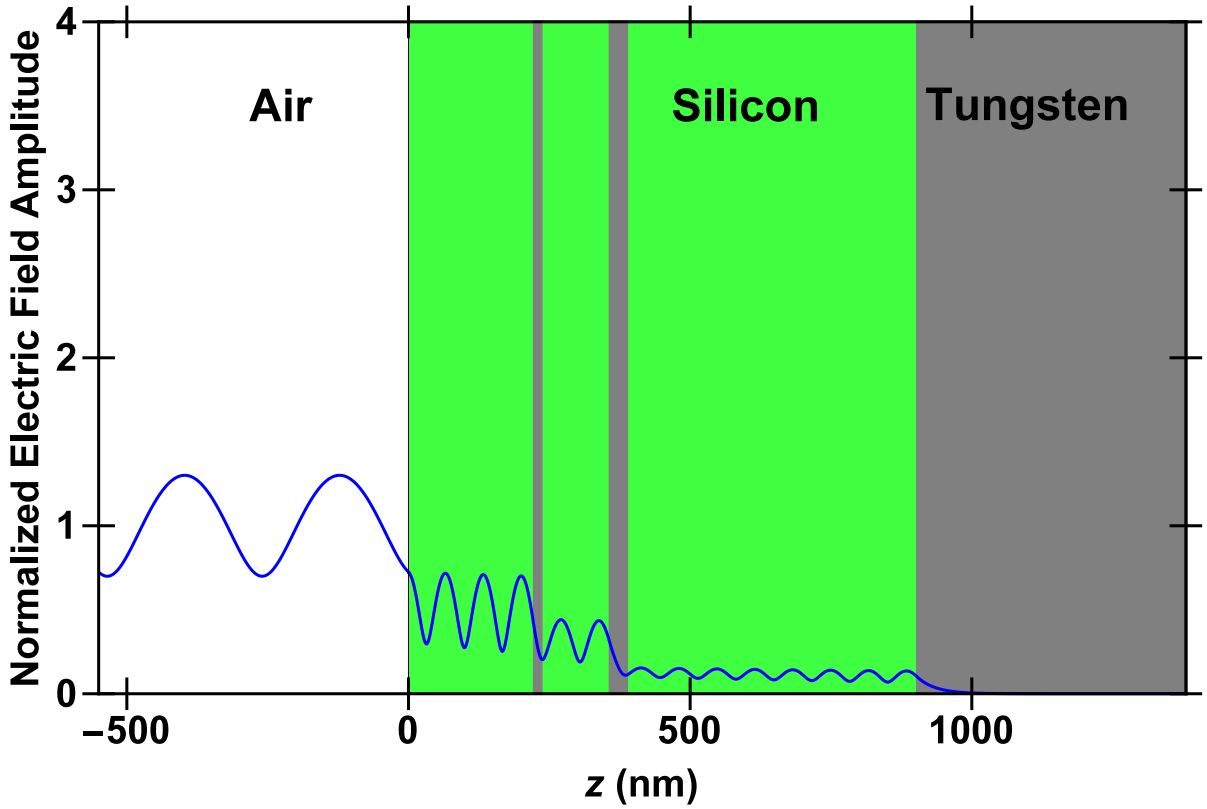

FIGURE 3.4: Profile of the electric field amplitude, normalized with respect to the field amplitude of the incident plane wave for the six-layer genetic-algorithm-optimized tungsten-silicon aperiodic structure described in Figure 3.2. Note that the thickness of the first tungsten layer is zero; thus, the layer adjacent to air is silicon. The structure is excited by a normally incident plane wave at the wavelength of $\lambda_0 = 550$ nm. The ratio of the power absorbed inside each layer to the total power absorbed in the structure was calculated and from left to right, beginning with air, is: {0, .273, .323, .06, .274, .03, .04}. That is, ∼27.3% of the power is absorbed in the first silicon layer adjacent to air; while, ∼4% is absorbed in the tungsten substrate.

$\lambda_0 = 550$ nm. We observe that the structure is almost perfectly impedance-matched to air, since only ∼10% of the incident power is reflected. For this tungsten-silicon structure, the first two layers provide the majority of the absorption in the structure, contributing ∼27% and ∼32%, respectively. The second tungsten layer provides ∼27%; while, the substrate provides less than ∼5 % of the overall absorption of the structure. In the silicon-tungsten structure, it is obvious from Figure 3.4 that there is no field enhancement provided by the structure. We therefore conclude that the high absorptance at normal incidence is not asso-

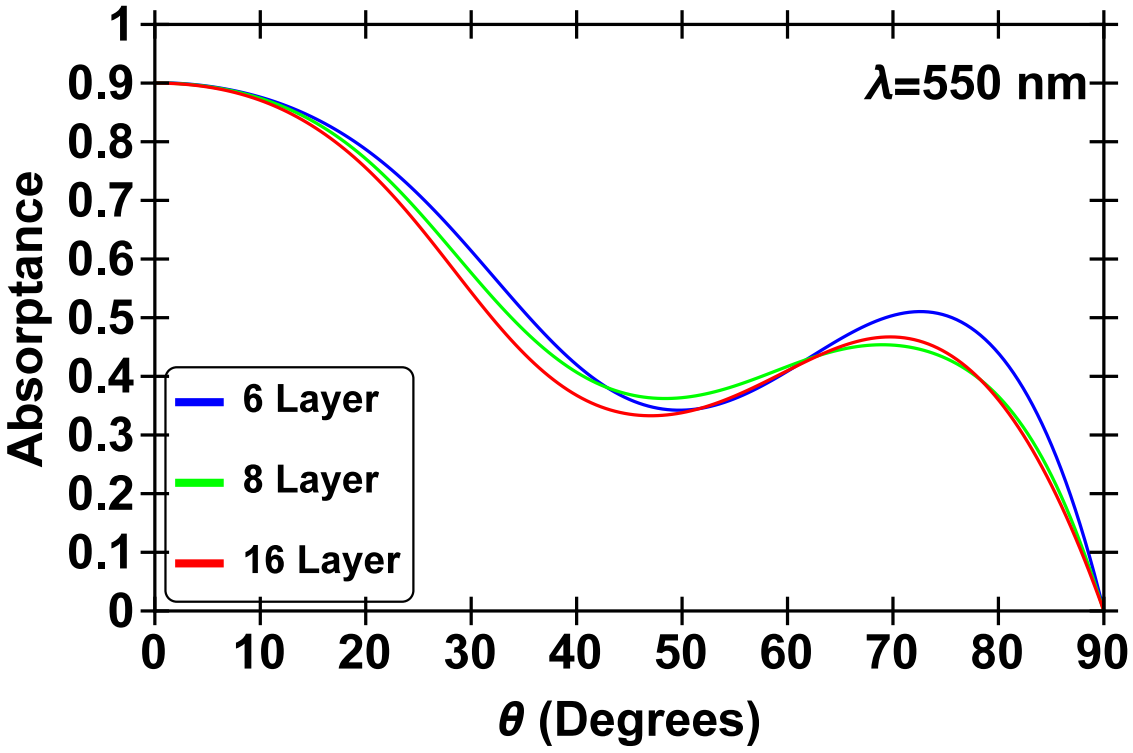

FIGURE 3.5: Absorptance versus angle of an optimized aperiodic multilayer structure of six, eight, and sixteen alternating layers of tungsten and silica over a semi-infinite tungsten substrate. The structure is optimized such that the integral of the absorptance over all angles for $\lambda_0 = 550$nm is minimized subject to the constraint that the absorptance at normal incidence is greater than 90% ($A_{\min} = 0.90$). The layer thicknesses of the optimized tungsten-silica structures (in units of nanometers) are: {2, 406, 21, 171, 34, 137} for the six-layer structure, {0, 395, 3, 207, 21, 165, 34, 144} for the eight-layer structure, and {0, 413, 9, 192, 22, 168, 22, 155, 26, 293, 0, 392, 17, 163, 13, 517} for the sixteen-layer structure. It is important to note that, for some layers, the optimized thickness was found to be zero. We also found that for the optimized tungsten-silicon structures the top layer, which is adjacent to air, is in the case of the eight and sixteen layer structure, silicon.

ciated with any strong resonances. This is also supported by the broad angle and wideband absorptance depicted in Figures 3.2 and 3.3.

We also consider structures of six, eight, and sixteen layers composed of alternating layers of tungsten and silica. Again, we minimize the fitness function, $F(\lambda_0)$, [Equation (3.2)] subject to the constraint that the normal incidence absorptance, $A_{\text{Total}}(\lambda_0, \theta) \geq A_{\min} = 0.90$.

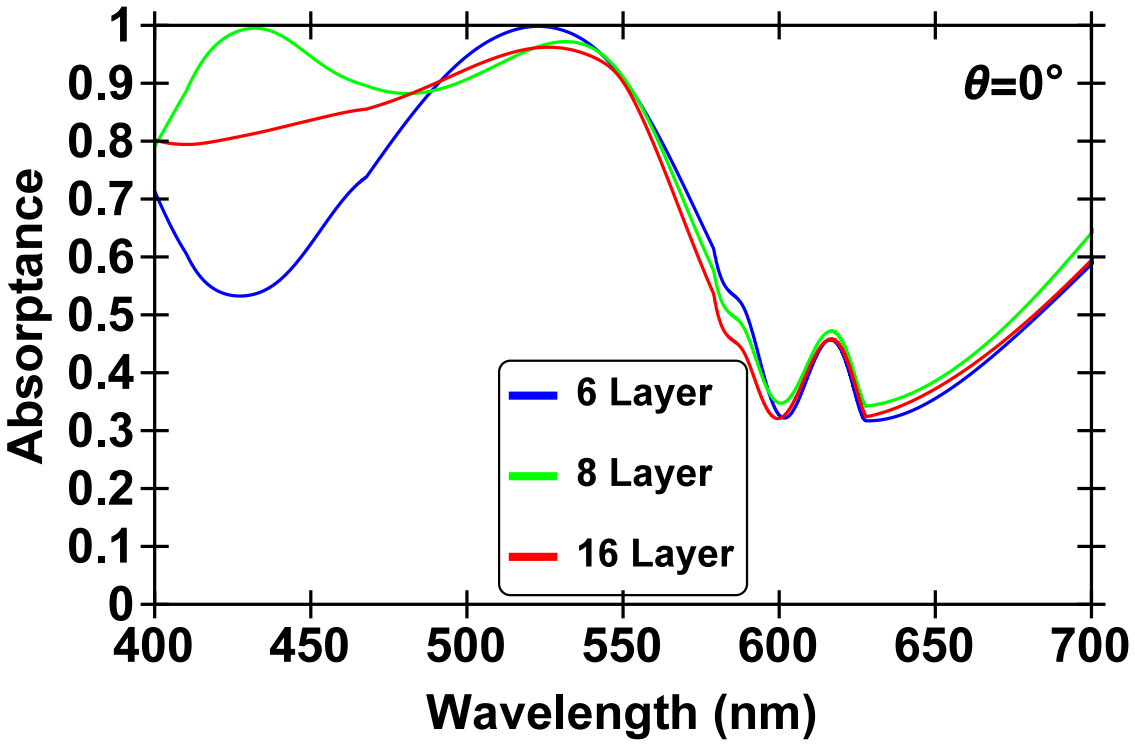

FIGURE 3.6: Absorptance versus wavelength of the same structures described in Figure 3.5 at normal incidence.

TABLE 3.2: Angular FWHM $\delta\theta_n$ and spectral FWHM $\delta\lambda_n$ of the tungsten-silica structures described in Figure 3.5.

n	$\delta\theta_n$	$\delta\lambda_n$
6	74.6°	88.4 nm
8	72.9°	82.6 nm
16	68.4°	71.0 nm

Similar to the tungsten-silicon structures, the tungsten-silica structures do not exhibit high angular selectivity in absorptance. As depicted in Figure 3.5, the tungsten-silica structures all achieve a peak of 90% absorptance at normal incidence and exhibit reduced angular FWHM, $\delta\theta_n$, (Table 3.2) when compared to the tungsten-silicon structures. However, the tungsten-silica structures maintain high absorptance for large angles of incidence [Figure 3.5]. We note that the tungsten-silica structures possess more broadband absorptance, having a larger spectral FWHM ($\delta\lambda_n$) compared to the tungsten-silicon structures (Table 3.2). In

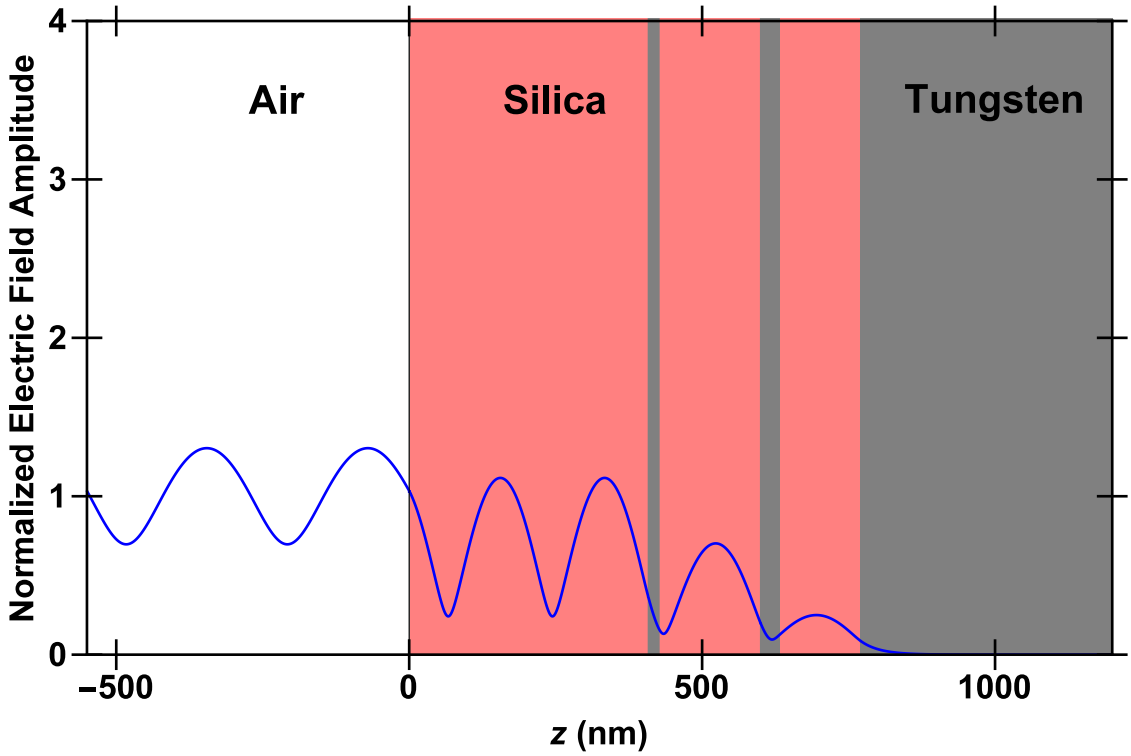

FIGURE 3.7: Profile of the electric field amplitude, normalized with respect to the field amplitude of the incident plane wave for the six-layer genetic-algorithm-optimized tungsten-silica aperiodic structure described in Figure 3.5. The structure is excited by a normally incident plane wave at the wavelength of $\lambda_0 = 550$ nm. The ratio of the power absorbed inside each layer to the total power absorbed in the structure was calculated and from left to right, beginning with air, is: {0, .541, 0, .302, 0, .13, 0, .03}. That is, ∼54.1% of the power is absorbed in the first tungsten layer adjacent to air; while, ∼3% is absorbed in the tungsten substrate.

Figure 3.7, we show the profile of the electric field amplitude, normalized with respect to the field amplitude of the incident plane wave for the six-layer genetic-algorithm-optimized aperiodic tungsten-silica structure. As before, the structure is excited by a normally incident plane wave at the wavelength of $\lambda_0 = 550$ nm. In the tungsten-silica structure, ∼85% of the absorption occurs in the first two tungsten layers. The substrate provides less than ∼5% of the overall absorptance in the structure. As with the tungsten-silicon structure, the absorptance mechanism is non-resonant and is the result of impedance matching.

Overall, due to the high absorption of tungsten, we found that it is not possible to achieve angular selectivity with structures using tungsten. In both tungsten-based structures, the

high absorptance at normal incidence is not associated with resonant field enhancement. In addition, in both cases the structures were impedance-matched to air in a broad wavelength range.

3.3.2 Silica-Silicon Structures

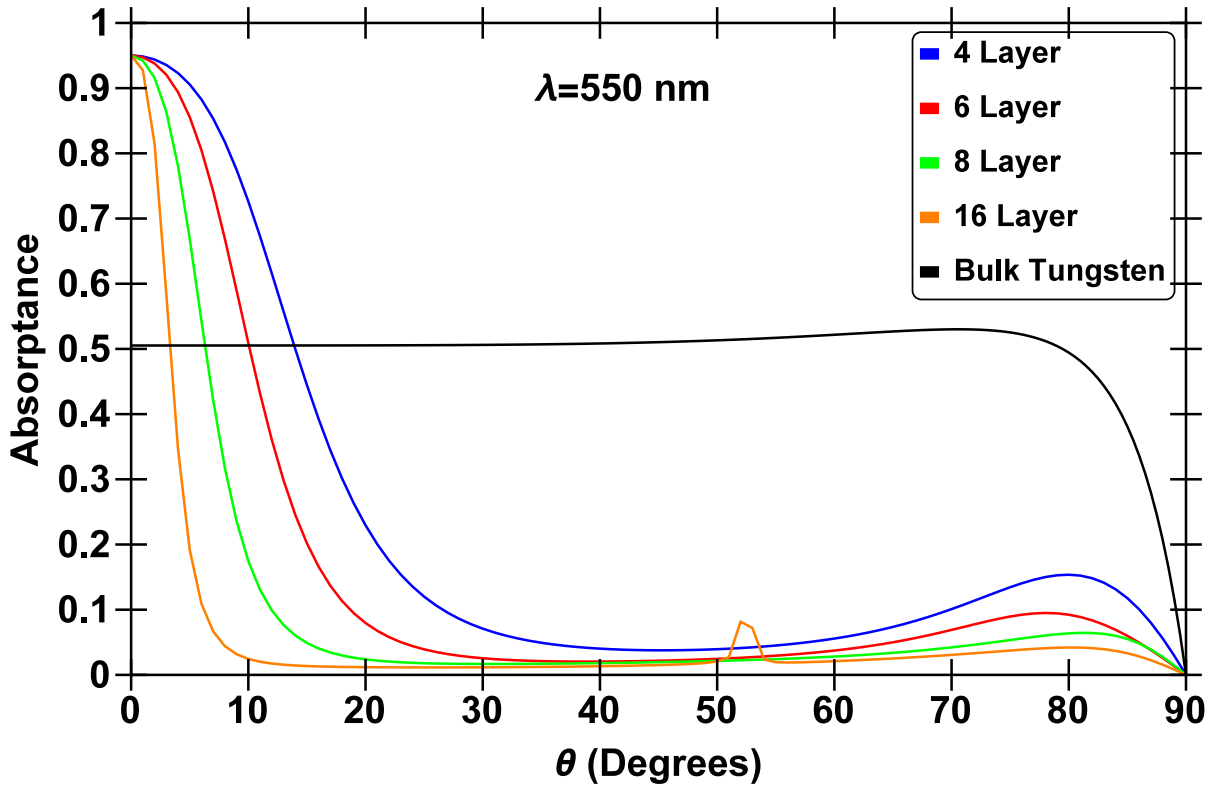

FIGURE 3.8: Absorptance versus angle of an optimized aperiodic multilayer structure of four, six, eight, and sixteen alternating layers of silicon and silica over a semi-infinite tungsten substrate. The structure is optimized such that the integral of the absorptance over all angles for $\lambda_0 = 550$nm is minimized subject to the constraint that the absorptance at normal incidence is greater than 0.95 ($A_{\min} = 0.95$). The absorptance of bulk tungsten is depicted in black for reference. The layer thicknesses of the optimized silicon-silica structures (in units of nanometers) are: {28, 530, 33, 301} for the four-layer structure, {30, 508, 32, 340, 34, 88} for the six-layer structure, {25, 110, 34, 530, 34, 92, 33, 80} for the eight-layer structure, and {12, 172, 28, 120, 34, 496, 34, 503, 0 (silicon), 550, 25, 321, 27, 106, 36, 81} for the sixteen-layer structure. It is important to note that in some cases the optimized thickness was found to be zero.

We consider structures of four, six, eight, and sixteen layers composed of alternating layers of silicon and silica over a semi-infinite tungsten substrate. In each case, we minimize the

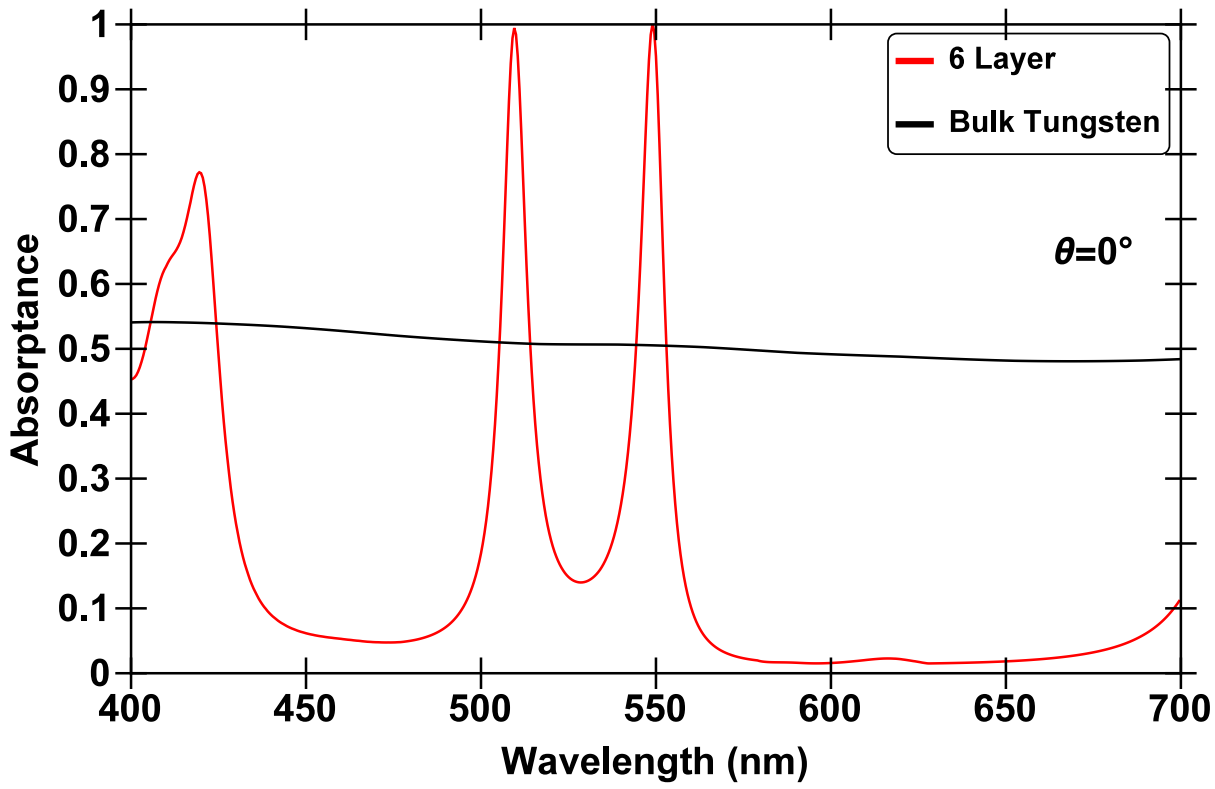

FIGURE 3.9: Absorptance versus wavelength of the six-layer structure described in Figure 3.8 at normal incidence. Again, absorptance of bulk tungsten is depicted in black for reference.

fitness function, $F(\lambda_0)$, [Equation (3.2)] subject to the constraint that the normal incidence absorptance at $\lambda_0 = 550$ nm, $A_{\text{Total}}(\lambda_0, \theta) \geq A_{\text{min}} = 0.95$. In doing so, we seek structures which provide narrow angular absorptance profiles.

TABLE 3.3: Angular FWHM $\delta\theta_n$ and spectral FWHM $\delta\lambda_n$ of the silicon-silica structures described in Figure 3.8.

n	$\delta\theta_n$	$\delta\lambda_n$
4	28.8°	12.8 nm
6	20.8°	6.6 nm
8	13.3°	2.6 nm
16	6.9°	0.8 nm

The genetic-algorithm-optimized, silicon-silica structures exhibit angular selectivity at $\lambda = 550$ nm, the wavelength at which the structures are optimized. As before, the FWHM comparison of the optimized four, six, eight, and sixteen layer structures can be found in

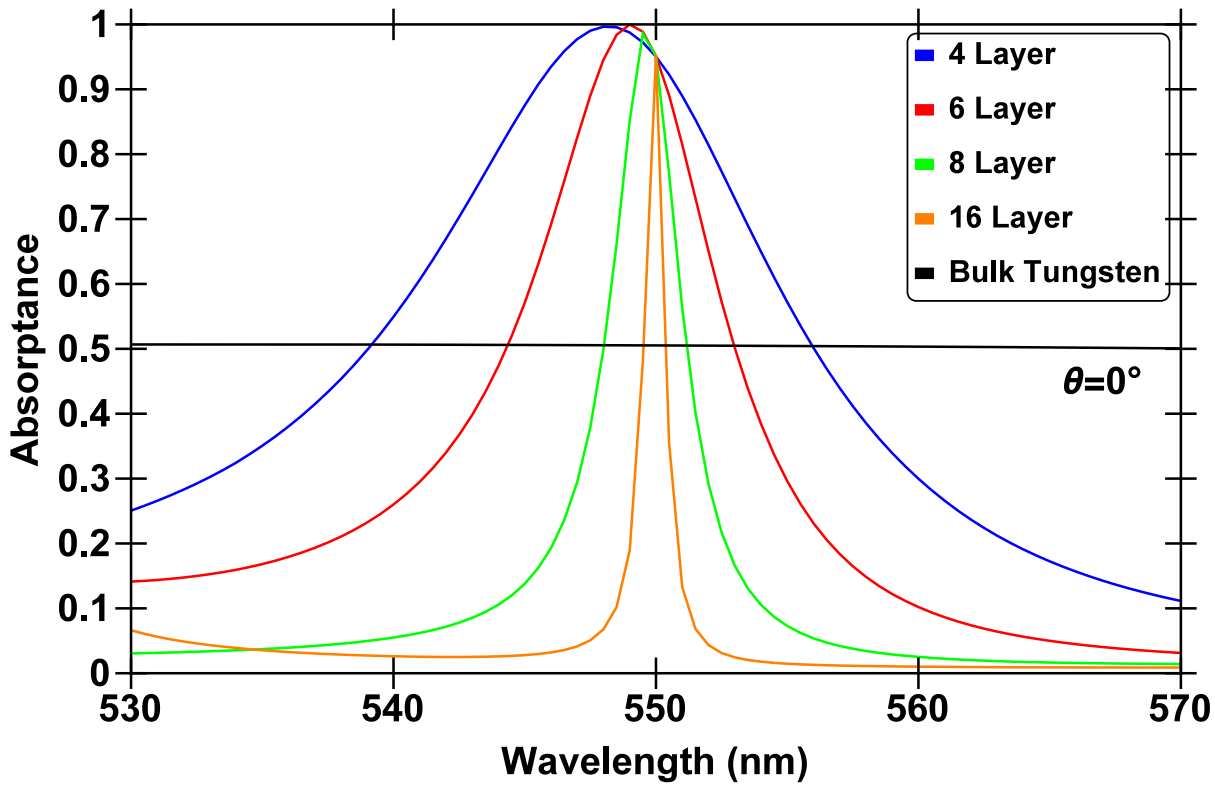

FIGURE 3.10: Absorptance versus wavelength of the four, six, eight, and sixteen layer structures described in Figure 3.8 and zoomed in on the wavelength for which the structure was optimized. Absorptance of bulk tungsten is depicted in black for reference.

Table 3.3. All of the silicon-silica structures exhibit angular selectivity, with each structure peaking at 95% absorptance at normal incidence and decreasing rapidly as θ increases [Figure 3.8]. We also note that there is a trend of increasing angular selectivity as the number of layers increases. For comparison, the absorptance of bulk tungsten at this wavelength is also shown. Figure 3.9 shows the spectral response at normal incidence of the six-layer genetic-algorithm-optimized, silicon-silica structure as well as bulk-tungsten's response. The six-layer structure provides a narrow band response centered around the wavelength at which it is optimized with additional resonances at other wavelengths. The eight and sixteen layer structures' spectral response at normal incidence is similar. As the number of layers in the optimized structure increases, the number of resonances in the $\lambda = 400$ nm to $\lambda = 700$ nm wavelength range also increases. Figure 3.10 shows the absorptance of the four, six, eight,

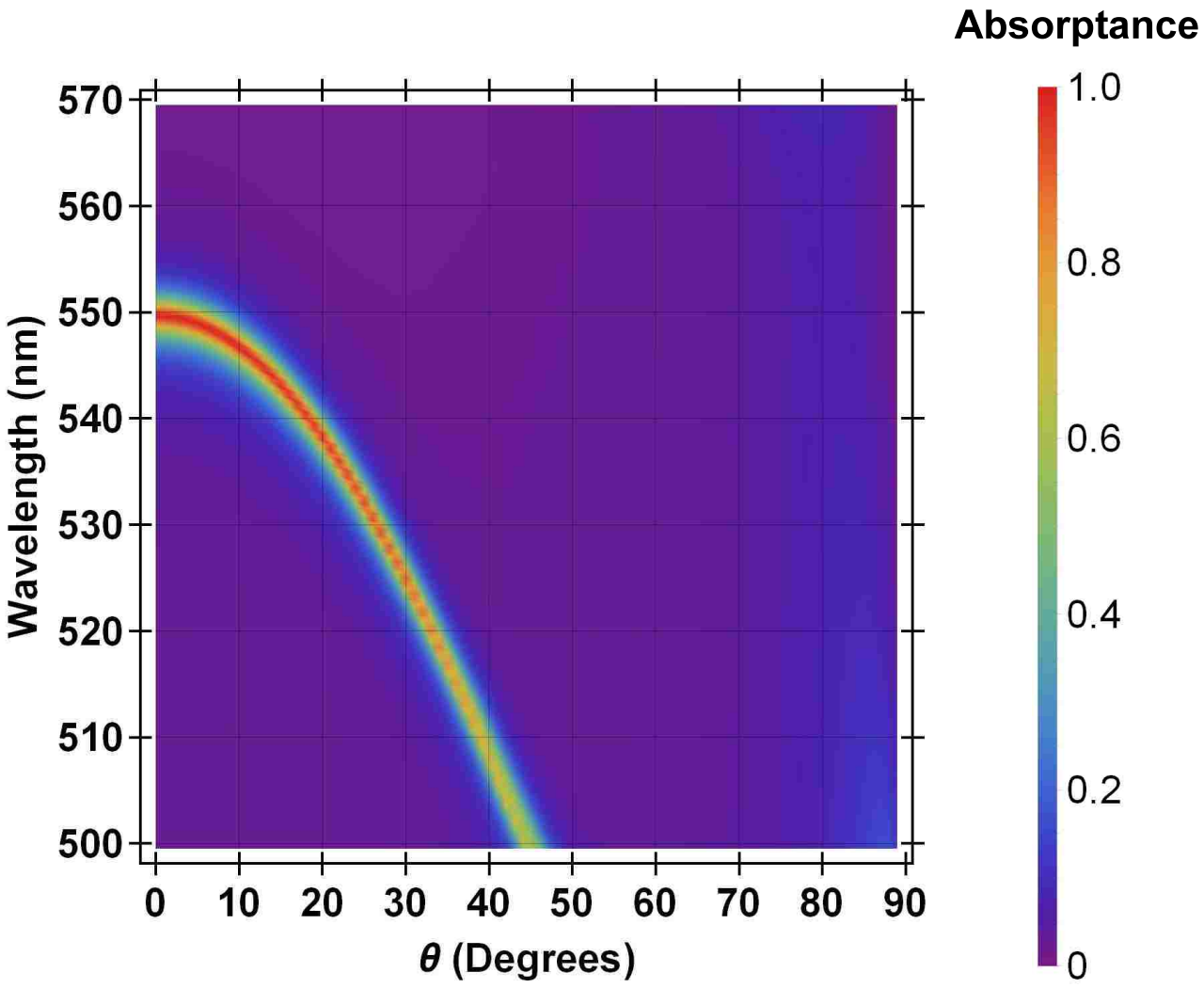

FIGURE 3.11: Absorptance as a function of wavelength and angle for the eight-layer, genetic-algorithm-optimized, aperiodic structure described in Figure 3.8.

and sixteen layer structures near $\lambda = 550$ nm, the wavelength at which the structures are optimized. We observe that there is a trend of decreasing spectral resonance width with increasing number of layers in the optimized structure. Figure 3.11 shows a color plot of the absorptance as a function of both angle and wavelength for the eight-layer, genetic-algorithm-optimized structure. We observe that the structure exhibits angular selectivity around the wavelength at which it was optimized, but its angular occurrence shifts with wavelength. More specifically, as the wavelength decreases, the peak of the absorptance shifts to larger

angles. Overall, with increasing number of layers, we observe an increase in angular selectivity and a decrease in the wavelength range of high absorptance at normal incidence.

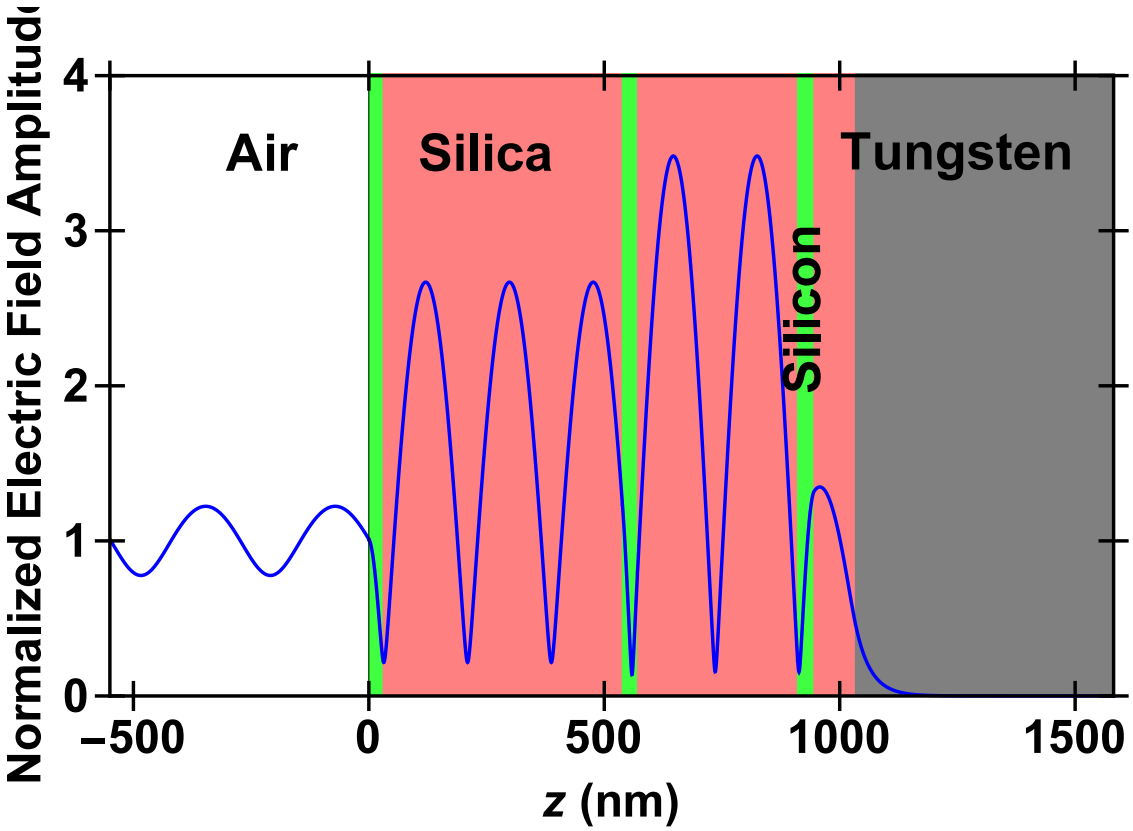

FIGURE 3.12: Profile of the electric field amplitude, normalized with respect to the field amplitude of the incident plane wave for the six-layer genetic-algorithm-optimized aperiodic structure described in Figure 3.8. The structure is excited by a normally incident plane wave at the wavelength of $\lambda_0 = 550$ nm. The ratio of the power absorbed inside each layer to the total power absorbed in the structure was calculated and from left to right, beginning with air, is: {0, .062, 0, .06, 0, .107, 0, .77}.

In Figure 3.12 and Figure 3.13 we show the profile of the electric field amplitude, normalized with respect to the field amplitude of the incident plane wave for both the six-layer and eight-layer genetic-algorithm-optimized, silicon-silica aperiodic structures. The structure is excited by a normally incident plane wave at $\lambda_0 = 550$ nm, the wavelength at which the structures are optimized. In the six-layer structure [Figure 3.12], we observe a large, resonant enhancement of the electric field toward the center of the structure. As a result, the majority ($\sim$77%) of the power is absorbed in the tungsten substrate. In the eight-layer structure

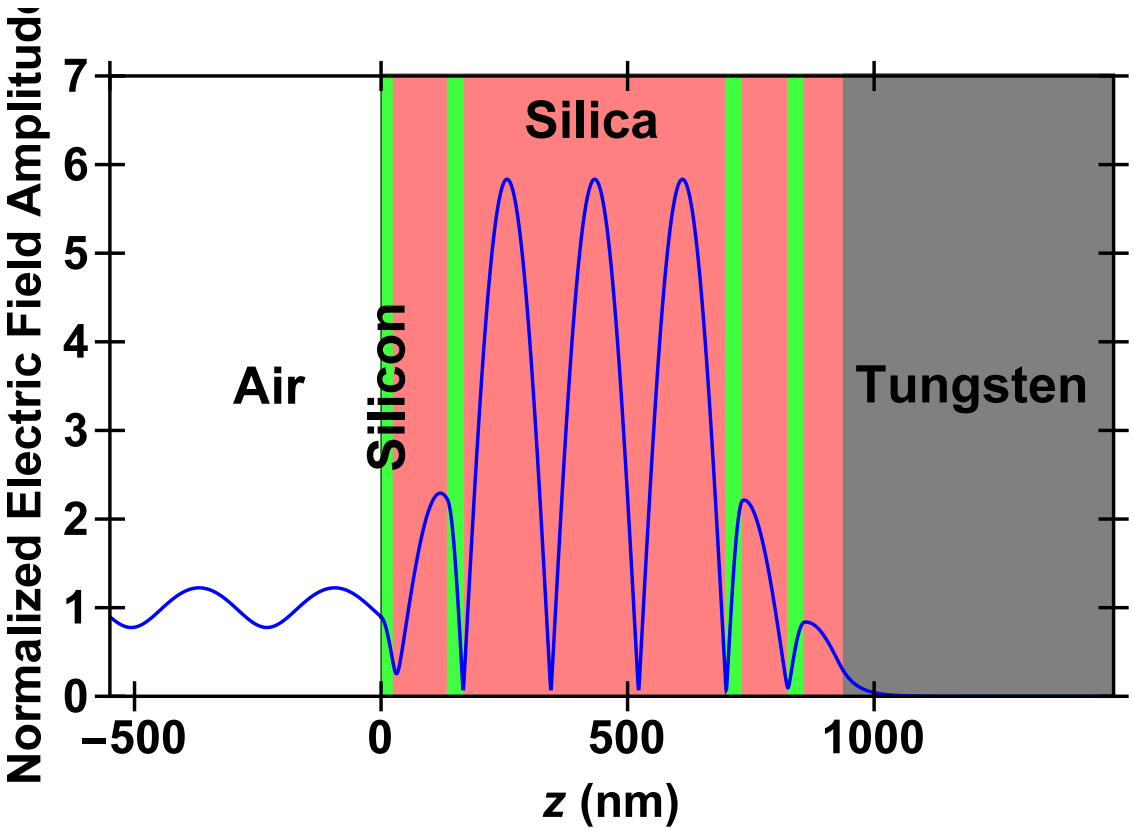

FIGURE 3.13: Profile of the electric field amplitude, normalized with respect to the field amplitude of the incident plane wave for the eight-layer genetic-algorithm-optimized aperiodic structure described in Figure 3.8. The structure is excited by a normally incident plane wave at the wavelength of $\lambda_0 = 550$ nm. The ratio of the power absorbed inside each layer to the total power absorbed in the structure was calculated and from left to right, beginning with air, is: {0, .048, 0, .29, 0, .318, 0, .046, 0, .3}. That is, ∼5% of the power is absorbed in the first silicon layer adjacent to air; while, ∼30% is absorbed in the tungsten substrate.

[Figure 3.13], the enhancement of the field is approximately twice the enhancement of the six-layer structure; however, the majority of the power is absorbed outside of the tungsten substrate. Less than one-third of the overall power is absorbed in the tungsten substrate. The two largest contributors to power absorbed for the eight-layer structure are the second and third silicon layers with the second silicon layer absorbing ∼29% and the third silicon layer absorbing ∼32% of the total power absorbed by the structure. Overall, we found that with increasing number of layers, the fraction of the power absorbed in the substrate decreases. We also found that, when the wavelength or the angle of incidence are shifted away from the resonance, the field enhancement rapidly decreases. This is consistent with the narrowband,

highly directional absorptance of the structure (Figure 3.8). Additionally, it is important to note that as the number of layers increases, the field enhancement drastically increases.

In short, unlike the structures containing tungsten, optimized, multilayer, silicon-silica structures exhibit high angular selectivity for absorptance at the wavelength at which they are optimized. However, we found that, for such optimized multilayer silicon-silica structures, as the angular FWHM, $\delta\theta_n$, decreases, the spectral FWHM, $\delta\lambda_n$, also decreases. In other words, as the angular selectivity in absorptance increases, the wavelength range of high angular selectivity decreases.

3.3.3 Multiple Material Structures

We also investigated optimizing the material composition of the multilayer structures in addition to optimizing the layer thicknesses. As before, we minimize the fitness function, $F(\lambda_0)$, [Equation (3.2)] subject to the constraint that the normal incidence absorptance at $\lambda_0 = 550$ nm, $A_{\text{Total}}(\lambda_0, \theta) \geq A_{\text{min}} = 0.95$. In doing so, we seek structures which provide narrow angular absorptance profile. More specifically, for each layer, the material was chosen among silicon, silica, tungsten, and silicon carbide. In each case, the genetic optimization algorithm searched for the optimal material composition as well as the optimal thickness of each layer. We considered structures consisting of four, six, eight, and sixteen layers. In all cases except for the four-layer structure, silicon carbide was found to be the optimal material for the first layer adjacent to air. In addition, none of the optimized multilayer structures contained tungsten. The fact that the optimal material composition of the multilayer structure does not contain tungsten is consistent with our conclusion in Subsection III.A that it is not possible to achieve angular selectivity in the absorptance with structures containing highly lossy materials such as tungsten.

Even though the optimized material composition was found to be, in general, different from the one of the silicon-silica multilayer structures, the improvement in angular selectivity with respect to silicon-silica structures with the same number of layers was marginal. More

specifically, for a given number of layers n, the angular FWHM, $\delta\theta_n$ of the structures with optimized material composition was no more than 2% decreased with respect to the silicon-silica multilayer structures with the same number of layers.

3.3.4 Bichromatic Absorber

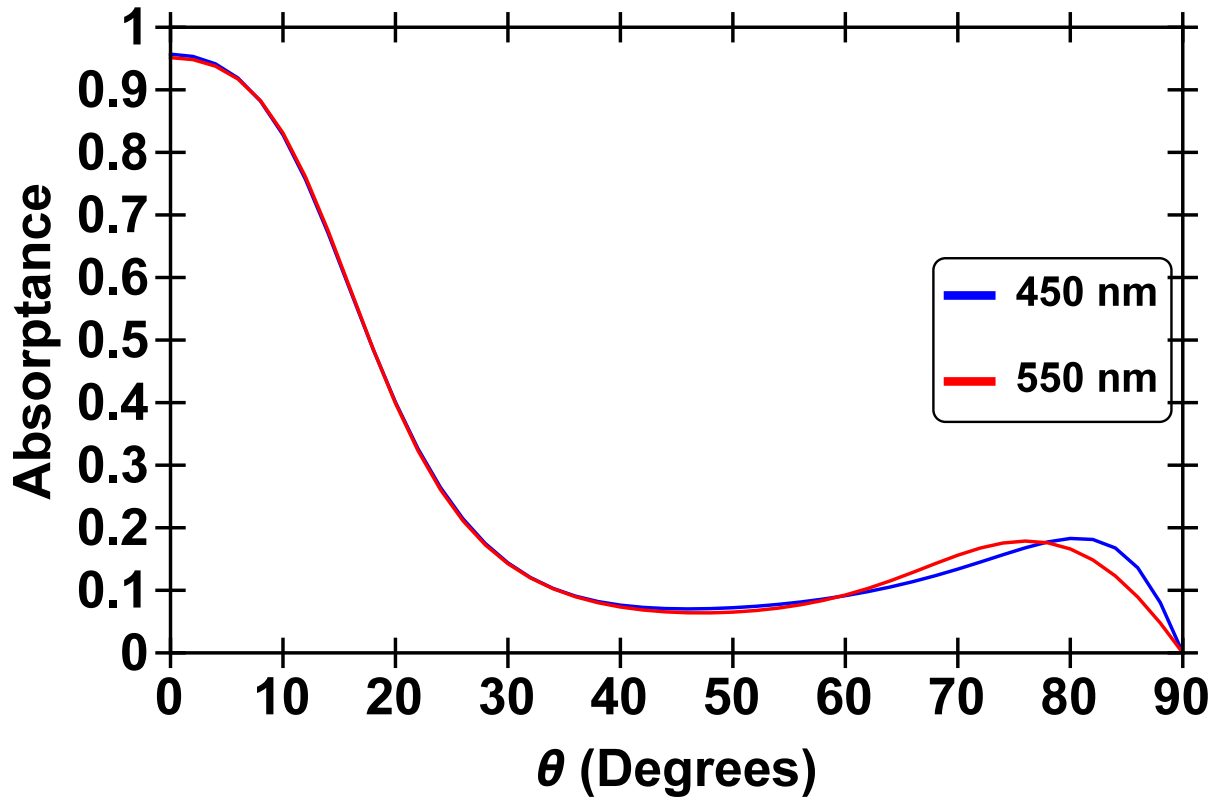

FIGURE 3.14: Absorptance versus angle of an aperiodic multilayer structure of eight alternating layers of silicon and silica over a semi-infinite tungsten substrate. The structure is optimized such that the integral of the sum of the absorptances at the wavelengths at which the structure was optimized over all angles, θ, is minimized subject to the constraint that the absorptance at normal incidence was at least $A_{\text{min}} = 0.95$ at all wavelengths considered. Simultaneously, we constrained the angle-average difference between the absorptances at the two wavelengths at which the structures were optimized to be less than 0.01. The layer thicknesses of the optimized silicon-silica structure (in units of nanometers) for the eight-layer structure are: {14, 300, 69, 248, 21, 127, 245, 463}.

As described in Subsection III.B, optimized silicon-silica multilayer structures exhibit high angular selectivity in absorptance when optimized at a single wavelength in the visible wavelength range. However, as the angular selectivity increases, wavelength selectivity also in-

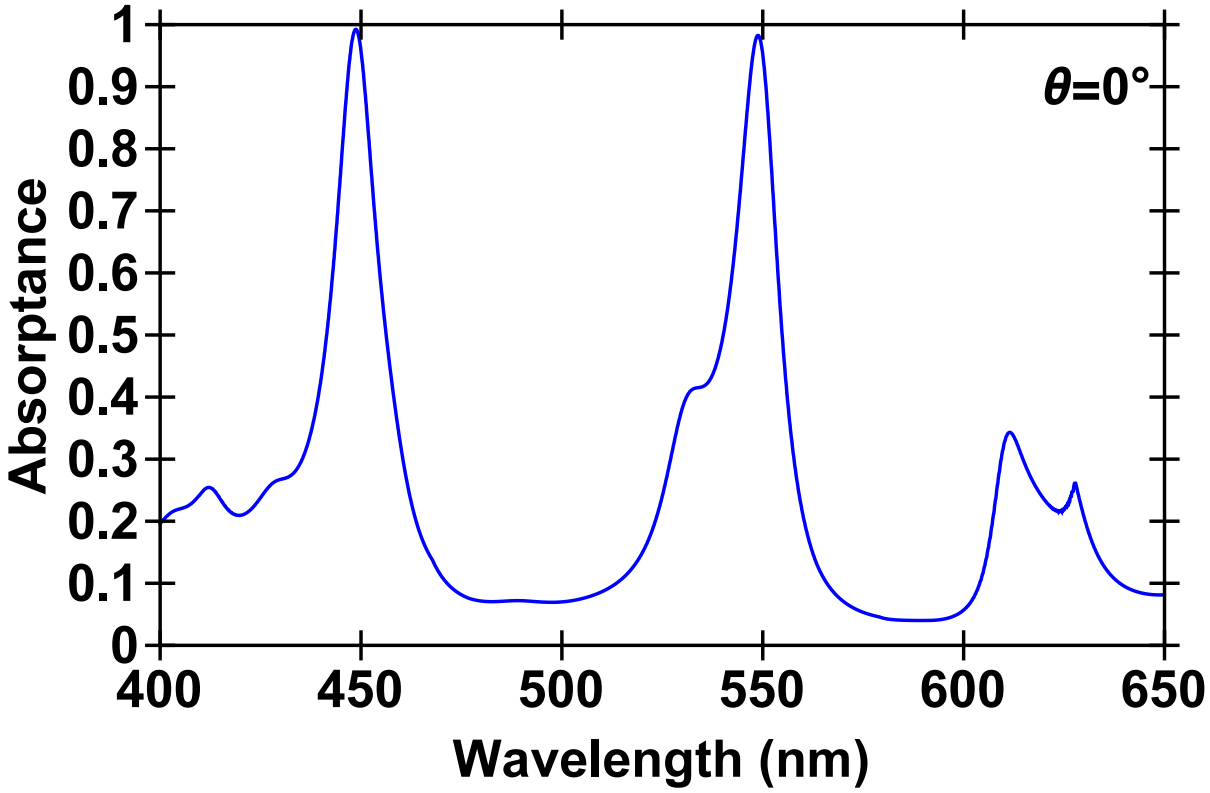

FIGURE 3.15: Absorptance versus wavelength of the same structure described in Figure 3.14 at normal incidence.

creases. In an attempt to increase the wavelength range of high angular selectivity in absorptance, we investigate optimizing the angular selectivity of multilayer structures at multiple wavelengths.

More specifically, we calculate the absorptance of each structure as a function of angle for $0° \leq \theta \leq 90°$ at two wavelengths, $\lambda_1 = 450$ nm and $\lambda_2 = 550$ nm in the visible wavelength range. Then we minimize the fitness function, $F_1(\lambda_1, \lambda_2)$,

$$F(\lambda_1, \lambda_2) = \int_0^{\frac{\pi}{2}} [A_{\text{Total}}(\lambda_1, \theta) + A_{\text{Total}}(\lambda_2, \theta)]\, d\theta, \tag{3.3}$$

subject to the constraints $A_{\text{Total}}(\lambda_i, \theta = 0°) \geq A_{\text{min}} = 0.95$, $i = 1, 2$. Here, $A_{\text{Total}}(\lambda_i, \theta) = [A_{\text{TE}}(\lambda_i, \theta) + A_{\text{TM}}(\lambda_i, \theta)]/2$.

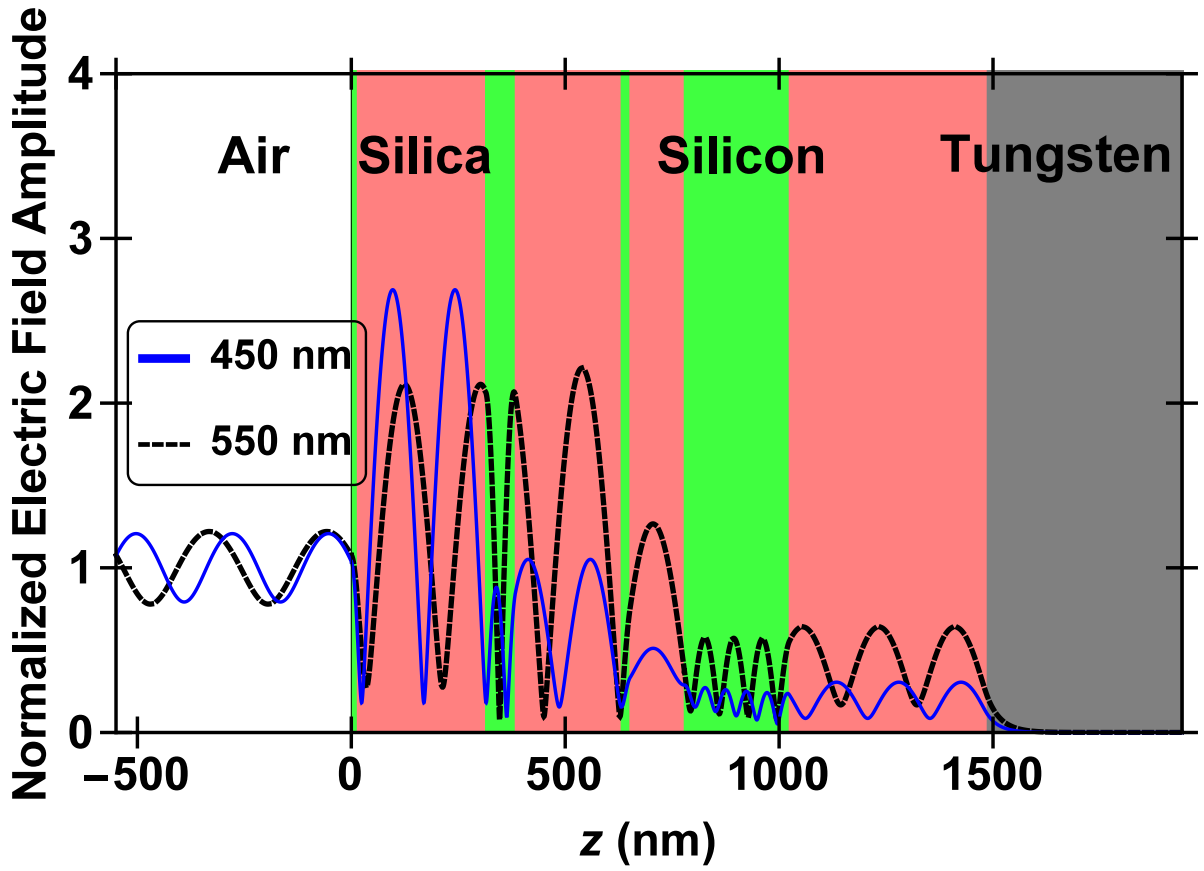

FIGURE 3.16: Profile of the electric field amplitude, normalized with respect to the field amplitude of the incident plane wave for the eight-layer, genetic-algorithm-optimized, aperiodic structure described in Figure 3.14. The structure is excited by a normally incident plane wave of $\lambda_1 = 450$ nm (blue) and $\lambda_2 = 550$ nm (black, dashed). The ratio of the power absorbed inside each layer to the total power absorbed in the structure was calculated and from left to right, beginning with air, is: {0, .217, 0, .519, 0, .025, 0, .196, 0, .04} for $\lambda_1 = 450$ nm, and {0, .053, 0, .596, 0, .021, 0, .155, 0, .17} for $\lambda_2 = 550$ nm. That is, for $\lambda_1 = 450$ nm, $\sim$22% of the power is absorbed in the first silicon layer adjacent to air; while, $\sim$4% is absorbed in the tungsten substrate.

That is, we calculate the integral of the sum of the absorptances at the wavelengths at which the structure is optimized over all angles, θ, and minimize it subject to the constraint that the absorptance at normal incidence is at least $A_{\min} = 0.95$ at all wavelengths considered. However, we found that with this optimization process, the absorptance response of the optimal structures was not unique. This is due to the fact that structures with identical fitness, $F_1(\lambda_1, \lambda_2)$ may exhibit different angular selectivity at the wavelengths at which the structures are optimized. As an example, we consider two distinct structures. One of the

structures exhibits higher angular selectivity at wavelength λ_1, $[\delta\theta(\lambda_1) < \delta\theta(\lambda_2)]$; the other one exhibits higher angular selectivity at λ_2 $[\delta\theta(\lambda_1) > \delta\theta(\lambda_2)]$, while both have the same fitness, $F_1(\lambda_1, \lambda_2)$.

To address this, we added one additional constraint in the optimization process:

$$F_2(\lambda_1, \lambda_2) = \frac{2}{\pi} \int_0^{\frac{\pi}{2}} |A_{\text{Total}}(\lambda_1, \theta) - A_{\text{Total}}(\lambda_2, \theta)| \; d\theta \leq \epsilon. \tag{3.4}$$

That is, we constrained the angle-average difference between the absorptances at the two wavelengths at which the structures were optimized to be less than ϵ. Here, we chose $\epsilon = 0.01$. In other words, the average difference in the angular absorptance profiles has to be less than 1%.

Here, we consider a structure composed of eight alternating layers of silicon and silica above a thick tungsten substrate. We found that at least eight layers are required in the silicon-silica structure in order to achieve high angular selectivity at the two wavelengths at which the absorptance of the structure was optimized. The structure provides relatively narrow-angular absorptance features at both of the wavelengths at which it was optimized, $\lambda_1 = 450$ nm and $\lambda_2 = 550$ nm. In fact, the angular absorptance spectra for the two wavelengths are nearly identical [Figure 3.14]. The absorptance of the optimized structure at normal incidence as a function of wavelength is shown in Figure 3.15. The structure absorbs the incident light almost completely at the two wavelengths at which it was optimized; however, similar to the structures optimized at a single wavelength (Subsection III.B), the wavelength range of high angularly selective absorptance is narrow (Table 3.4).

TABLE 3.4: Angular FWHM $\delta\theta_n$ and spectral FWHM $\delta\lambda_n$ of the structures described in Figure 3.14.

Wavelength	$\delta\theta$	$\delta\lambda$
$\lambda_1 = 450$ nm	36.7°	8.4 nm
$\lambda_2 = 550$ nm	36.6°	10.6 nm

In Figure 3.16, we show the profile of the electric field amplitude, normalized with respect to the field amplitude of the incident plane wave for the eight-layer, genetic-algorithm-optimized, aperiodic structure. The structure is excited by a normally incident plane wave at either $\lambda_1 = 450$ nm or $\lambda_2 = 550$ nm. While the wavelengths at which the structure was optimized have nearly identical angular spectra, the two absorptance mechanisms within the structure are different. The $\lambda_1 = 450$ nm light is absorbed mainly in the first two silicon layers, which account for over $\sim$70% of the structure's absorbed power. The tungsten substrate accounts for less than $\sim$5% of the overall power absorbed at $\lambda_1 = 450$ nm. The $\lambda_2 = 550$ nm light is absorbed mostly in the second silicon layer, which provides $\sim$60% of the overall absorption at this wavelength; the final silicon layer before the tungsten substrate and the substrate itself account for an additional $\sim$30% of the structure's absorbed power.

3.4 Conclusion

We investigated one-dimensional aperiodic multilayer structures for use as narrow-angular absorbers. We focused on structures which are highly absorbing for normally incident light and also exhibit highly directional absorptance. We optimized the layer thicknesses and materials using a genetic global optimization algorithm coupled to a transfer matrix code to maximize the angular selectivity in the absorptance at a single or multiple wavelengths.

We first considered structures composed of alternating layers of tungsten and silicon or silica over a tungsten substrate. We found that, due to the high absorption of tungsten, it is not possible to achieve angular selectivity in the absorptance with such structures. In addition, the absorptance of such tungsten-based structures is relatively broadband in nature, and is not associated with any strong resonances.

We next considered structures composed of alternating layers of silicon and silica. Unlike the tungsten-based multilayer structures, the optimized silicon-silica structures exhibit a resonance and high angular selectivity in absorptance at the wavelength at which they are optimized. The resonance is associated with large field enhancement in the structures. We

also found that there is a trend of increasing angular selectivity as the number of layers increases. However, as the angular selectivity in absorptance increases, the wavelength range of high angular selectivity decreases.

We then considered optimizing the material composition of the multilayer structures, in addition to optimizing the layer thicknesses. For each layer, the material was chosen among silicon, silica, tungsten, and silicon carbide. Even though the optimized material composition was found to be, in general, different from the one of the silicon-silica multilayer structures, the improvement in angular selectivity with respect to silicon-silica structures with the same number of layers was marginal.

Finally, we investigated optimizing the absorptance of the multilayer structures at multiple wavelengths. We found that this approach leads to structures exhibiting almost perfect absorptance at normal incidence and narrow angular width in absorptance at these wavelengths. However, similar to the structures optimized at a single wavelength, the wavelength range of high angularly selective absorptance is narrow.

As final remarks, we note that due to the wavelength dependence of the dielectric permittivity of the materials utilized in the design, one cannot simply scale the layer thicknesses by a factor to scale the operating wavelength by that same factor. In other words, the optimized designs are not scale invariant, so the optimization process must be carried out at the new desired wavelength. It is also important to note that the optimized designs for the tungsten-silica and tungsten-silicon multilayer structures are non-unique. In other words, there are multiple designs which achieve the minimum fitness. On the other hand, the optimized designs for the silicon-silica multilayer structures are unique. In addition, we note that it is possible to design silicon-silica multilayer structures which exhibit high angular selectivity in absorptance at visible wavelengths without the tungsten substrate. In these structures the light is absorbed in the silicon layers, since silicon is a lossy material in the visible.

It should also be noted that at the wavelength of $\lambda = 550$ nm the real part of the dielectric permittivity of tungsten is positive. Thus, at this wavelength tungsten behaves as an extremely lossy dielectric rather than as a plasmonic metal. The very high absorption of tungsten broadens all resonances both in angle and wavelength. In fact, we found that, if one assumes that tungsten is lossless [by setting $\epsilon_{\text{tungsten}} = \text{Re}(\epsilon_{\text{tungsten}})$ and neglecting the imaginary part $\text{Im}(\epsilon_{\text{tungsten}})$], then it is possible to design multilayer structures containing this artificially lossless tungsten which exhibit high angular selectivity in absorptance.

In addition, we note that angular selectivity in absorptance can also be achieved by a structure consisting of a quarter-wave one-dimensional photonic crystal placed over a perfect mirror with an absorbing material included in the defect layer formed by the photonic crystal and the mirror. In the one-dimensional photonic crystal structure the number of layers in the photonic crystal has to be adjusted in order to get unity absorptance at the resonance [24]. However, once the number of layers of the photonic crystal is chosen, the angular width of the absorptance cannot be tuned. Compared to such a structure, our proposed structures have many more degrees of freedom. Thus, it is possible to simultaneously obtain perfect absorptance on resonance and also tune the angular width of the absorptance. Our proposed aperiodic multilayer structures can achieve much narrower angular width than the one-dimensional photonic crystal structures. In addition, with the proposed aperiodic structures it is possible to achieve perfect absorptance at normal incidence and narrow angular width in absorptance at multiple closely-spaced tunable wavelengths. Such an absorptance response cannot be achieved with the one-dimensional photonic crystal structures.

This research was supported by the National Science Foundation (Award Nos. 1102301, 1263236, 1403105), and a Fund for Innovation in Engineering Research (FIER) grant from the Louisiana State University College of Engineering. Jonathan P. Dowling wishes to also acknowledge support from the Air Force Office of Scientific Research and the Army Research Office.

Chapter 4

How to Build a Better Lightbulb — Exploiting Optimization Algorithms to Decrease Incandescent Lightbulb Power Consumption by Nearly 50 %

In this chapter, we present optimized aperiodic structures for use as broadband, broad-angle thermal emitters which are capable of increasing the emittance by nearly a factor of two over the visible wavelength range when compared to bulk tungsten. These aperiodic multilayer structures designed with alternating layers of tungsten and air or tungsten and silicon carbide on top of a tungsten substrate exhibit high emittance in a broad wavelength range peaked around the center of the visible. We optimize the layer thicknesses using a hybrid optimization algorithm coupled to a transfer matrix code to maximize the power emitted in the visible wavelength range in the normal direction. We investigate the properties of these structures for use as lightbulb filaments, and compare their performance with conventional lightbulbs. We find that these structures greatly enhance the emittance over the visible wavelength range, while also increasing the overall efficiency of the bulb. These structures could lead to a decrease in incandescent lightbulb power consumption by nearly 50 %.

4.1 Introduction

Conventional incandescent lightbulbs (ILB) are composed of a tungsten filament inside a bulb which is filled with inert gas. These devices are less than 10 percent efficient [73, 74] due to the fact that most of the applied power is radiated as heat and not as visible light. There has been much recent work in an attempt to improve the efficiency of household and commercial lighting. Compact fluorescent lamps (CFLs), the curled bulbs, improve efficiency slightly, but have issues with slow turn on time, higher cost, degradation of performance over CFL lifetime, and most significantly, these bulbs contain mercury and pose an environmental hazard if broken or disposed in a landfill. The most efficient lighting commercially available

is the light-emitting diode (LED) which possesses efficiencies between 25 and 35 percent. LEDs, however, are extremely expensive (due to fabrication costs) which puts them out of reach of users in emergent countries. Hence, incandescent bulbs still account for the vast majority of home lighting in developing countries; while, in the United States, the ILB has been phased out to be replaced with CFL or LED lighting.

In this chapter, we propose one-dimensional multilayer aperiodic structures for use as incandescent lightbulb filaments. It has been shown that multilayer structures can tailor the emittance spectra of bulk materials and may provide properties similar to that of more complex and harder-to-fabricate two- or three-dimensional structures [40, 19, 21, 42, 23, 25, 26, 45, 46, 48, 49, 57, 58, 59, 60]. Here, we optimize the layer thicknesses using a hybrid optimization algorithm coupled to a transfer matrix code to maximize the power emitted in the visible wavelength range in the normal direction. First, we consider a tungsten-air structure above a tungsten substrate as a proof of concept. We next consider a tungsten and silicon-carbide structure for possible use as a filament in an incandescent lightbulb.

4.2 Theory

We model a structure composed of infinite slabs of material of varying aperiodic thicknesses as depicted in Figure 4.1. Utilizing the transfer matrix method, [34] we calculate the transmittance, reflectance, and absorptance of the structure for both TE and TM polarized light. Light is incident from air at an angle θ to the structure. We make use of experimental data for the wavelength-dependent indexes of refraction, both real and imaginary parts, for silicon carbide and tungsten [35] in all calculations done in this chapter. We choose silicon carbide and tungsten due to their high melting point, which is necessary for use in a lightbulb filament application. Since the tungsten substrate is taken to be semi-infinite, the transmittance is identically zero, so that:

$$A_{\mathrm{TE/TM}}(\lambda,\theta) = 1 - R_{\mathrm{TE/TM}}(\lambda,\theta), \tag{4.1}$$

where $A_{\mathrm{TE/TM}}$ is the TE/TM absorptance, $R_{\mathrm{TE/TM}}$ is the TE/TM reflectance, and λ is the

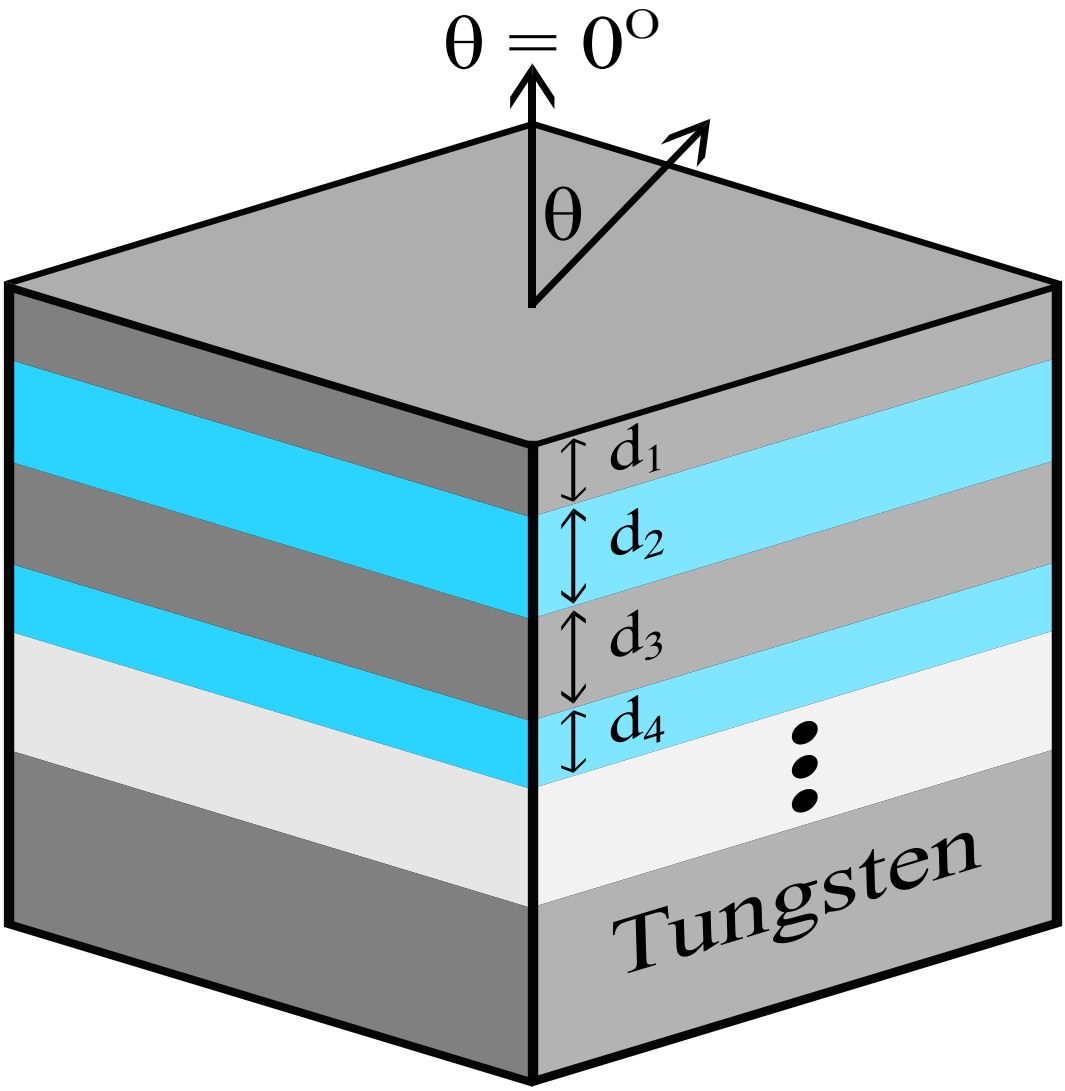

FIGURE 4.1: Schematic of the structure optimized. It consists of alternating layers of tungsten and air or tungsten and silicon carbide above a semi-infinite tungsten substrate.

wavelength. While we only calculate absorptance, reflectance, and, in principle, transmittance, we make use of Kirchhoff's second law and conservation of energy to equate absorptance ($A_{\mathrm{TE/TM}}$) and emittance ($\epsilon_{\mathrm{TE/TM}}$) under thermal equilibrium [36] .

More specifically, the power radiated per unit area and wavelength is given by the Planck blackbody spectrum (in units of Watt per square meter per nanometer): $B(\lambda, T) = \frac{2hc^2}{\lambda^5}(e^{\frac{hc}{\lambda k_B T}} - 1)^{-1}$, where h is Planck's constant, c is the speed of light, λ is the wavelength, T is the temperature, and k_B is the Boltzmann constant. We define the normalized power radiated per unit area and unit wavelength by a given structure, $\bar{\mu}(\lambda, \theta)$ as the ratio of the power emitted

per unit area and wavelength by the structure to the maximum emitted by a blackbody

$$\bar{\mu}(\lambda,\theta) = \frac{\epsilon_{\text{Total}}(\lambda,\theta)B(\lambda,T=2700K)}{\max\limits_{\lambda}[B(\lambda,T=2700K)]}. \tag{4.2}$$

Here, $\epsilon_{\text{Total}}(\lambda,\theta) = [\epsilon_{\text{TE}}(\lambda,\theta) + \epsilon_{\text{TM}}(\lambda,\theta)]/2$. We choose an operating temperature of 2700 K, below the melting point of silicon carbide and tungsten and near the operating temperature of modern incandescent lightbulbs [75].

Conventional incandescent lightbulbs are made by drawing tungsten into a thin wire and running a current through the wire. This process, via the resistance of the wire, heats the wire to a temperature between 2500 K and 3000 K and produces light over broad wavelength range. Due to the operating temperature of the filament as well as the emittance spectra of bulk tungsten, this process is inefficient and produces both a large amount of waste heat and light which is not in the visible wavelength range.

In a traditional incandescent lightbulb, in excess of 90% of the power which enters the bulb is released as heat. Additionally, of the approximately 10% of the power which is released as radiation, only a small percentage of the light is emitted in the visible wavelength range (Figure 4.2). We define the efficiency of a given structure as the ratio of the normalized power emitted in the visible wavelength range ($\lambda_1 = 400$ nm to $\lambda_2 = 700$ nm) to the total power emitted

$$\eta = \frac{\int\limits_{\lambda_1}^{\lambda_2} \bar{\mu}(\lambda,\theta=0^\circ)\,d\lambda}{\int\limits_{0}^{\infty} \bar{\mu}(\lambda,\theta=0^\circ)\,d\lambda}. \tag{4.3}$$

Using Equation (4.3), we find that for a bulk tungsten filament operating at T = 2700K, only $\sim 11.55\%$ of the power radiated lies in the visible wavelength range and is therefore useful for indoor lighting. The combination of these effects leads to an extremely low efficiency for conventional incandescent tungsten filament lightbulbs.

Another factor which contributes to the overall low efficiency of conventional tungsten filaments is the fact that tungsten is highly reflective over the visible wavelength range.

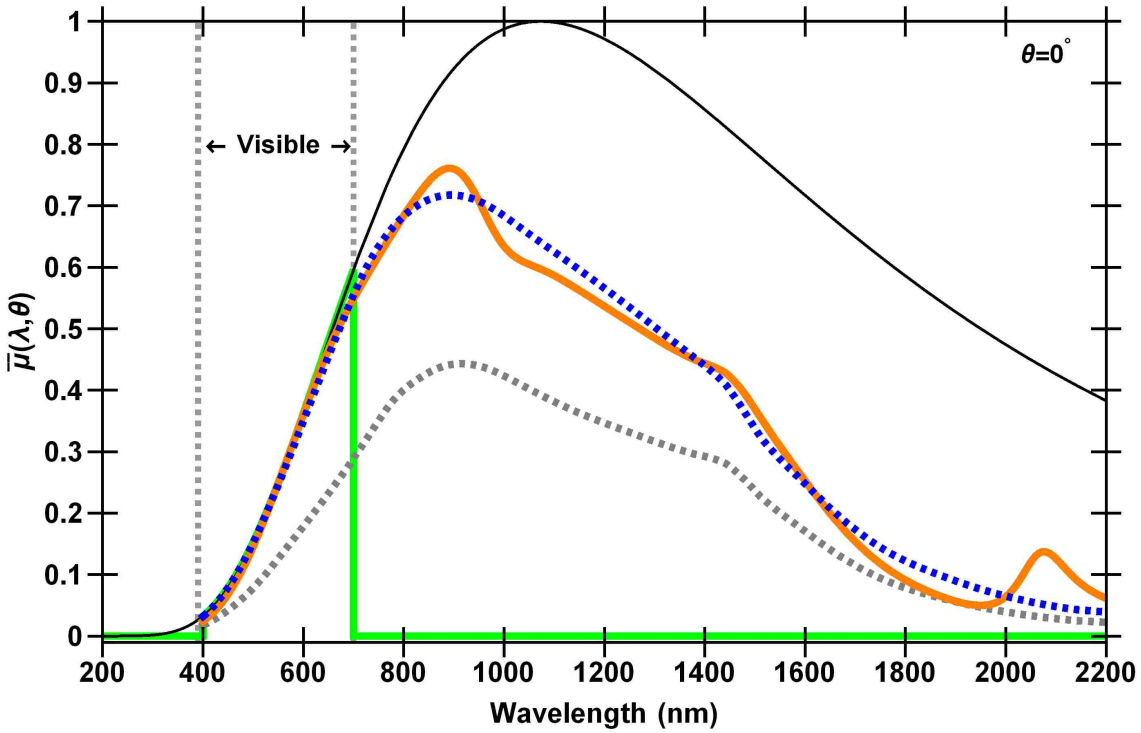

FIGURE 4.2: Normalized power emitted per unit area and unit wavelength, at normal incidence, $\bar{\mu}(\lambda, \theta)$, as a function of wavelength for the optimized structures compared to both a perfect blackbody at the same temperature as well as a conventional bulk-tungsten filament. The solid black line depicts a perfect blackbody at 2700 K. The solid green line shows the performance of an ideal filament operating at 2700 K. The dashed gray line shows the performance of a bulk tungsten lightbulb filament. The solid orange and dashed blue lines show the performance of the optimized TSiC and TA structures, respectively. The layer thicknesses of the optimized structures, in units of nanometers, beginning with the tungsten layer bordering air are: {3.4, 90, 163, 500} for the TA structure and {0, 39, 66, 319} for the TSiC structure.

Tungsten is a relatively poor emitter, with an average emittance over the visible spectrum of approximately 50%. We define the enhancement factor Q of a given structure as the ratio of the total power emitted in the visible by the structure at T = 2700 K to the power emitted by a bulk tungsten filament heated to the same temperature:

$$Q = \frac{\int_{\lambda_1}^{\lambda_2} \bar{\mu}(\lambda, \theta = 0°)\, d\lambda}{\int_{\lambda_1}^{\lambda_2} \bar{\mu}_{\mathrm{Bulk}}(\lambda, \theta = 0°)\, d\lambda}. \tag{4.4}$$

We are interested in finding structures which exhibit a plateau-like emittance over the visible wavelength range. That is, we seek a structure which possesses $\epsilon = 1.0$ in the visible wavelength range ($\lambda_1 \leq \lambda \leq \lambda_2$) and $\epsilon = 0.0$ elsewhere (corresponding to the solid green line in Figure 4.2) in an effort to maximize the power emitted by the structure in the visible while maximizing its efficiency.

We use a hybrid optimization method consisting of a micro-genetic global optimization algorithm [14, 13, 15, 17, 18, 76] coupled to a local optimization algorithm [12, 16] to determine the best dimensions for four-layer structures. The genetic algorithm is an iterative optimization procedure which starts with a randomly selected population of potential solutions and evolves toward improved solutions; once the population converges, the local optimization algorithm finds the local optimum. The process retains the best structure found and is iteratively repeated.

Specifically, we first maximize the fitness function F_1 where

$$F_1 = \int_{\lambda_1}^{\lambda_2} \bar{\mu}(\lambda, \theta = 0^\circ)\, d\lambda. \tag{4.5}$$

This process is carried out to enhance the emittance in the visible when compared to that of bulk tungsten.

We then seek to maximize the efficiency of the structure [Equation (4.3)] without significantly decreasing the enhancement of the power emitted in the visible compared to bulk tungsten [Equation (4.4)]. Due to the operating temperature of the structure, T = 2700 K, any radiation occurring at $\lambda \leq 400$nm can be treated as negligible. Thus, we minimize the normalized power emitted by the structure for $\lambda \geq 700$ nm, F_2,

$$F_2 = \int_{\lambda_2}^{\infty} \bar{\mu}(\lambda, \theta = 0^\circ)\, d\lambda, \tag{4.6}$$

subject to the constraint that the fitness function F_1 for the structure is at least 98 % of the previously calculated maximum F_1.

4.3 Results

We consider structures of four layers composed of alternating layers of tungsten and air (henceforth referred to as the TA structures) or alternating layers of tungsten and silicon carbide (henceforth referred to as the TSiC structures). We optimize the emittance of the structures using the process outlined above [Equations (4.5) and (4.6)]. Both of the optimized structures show drastically improved emittance (by nearly a factor of two) over the visible wavelength range when compared to bulk tungsten (Figure 4.2). Thus, these structures could lead to a decrease in incandescent lightbulb power consumption by nearly 50 %. More specifically, a lightbulb consuming 30 W of power using our design would radiate approximately the same energy in the visible as a conventional incandescent bulb which consumed 60 W of power. A detailed comparison of the optimized structures presented here and current lightbulb technology can be found in Figure 4.2. The emittance of the optimized structures approaches the one of a perfect blackbody. By comparing the bulk tungsten's (Figures 4.3(a) & 4.3(b) and 4.6(a) & 4.6(b)) emittance and normalized power emitted per unit area and unit wavelength $\bar{\mu}$ to that of both TA (Figures 4.4(a) & 4.4(b) and 4.6(c) & 4.6(d)) and TSiC structures (Figures 4.5(a) & 4.5(b) and 4.6(e) & 4.6(f)), we observe that the optimized structures provide greatly enhanced emittance over the visible wavelength range when compared to bulk tungsten. As a result, the optimized structures also greatly enhance the power emitted by the structures in the visible. A detailed comparison of the enhancement factor Q and the efficiency η of the different structures can be found in Table 4.1.

TABLE 4.1: Comparison of the enhancement, Q, and the efficiency, η, using bulk tungsten as a reference point, of the optimized structures described in Figure 4.2..

Structure	Q	η
Tungsten	1.0	11.55%
W-Air	1.927	13.62%
W-SiC	1.854	13.77%

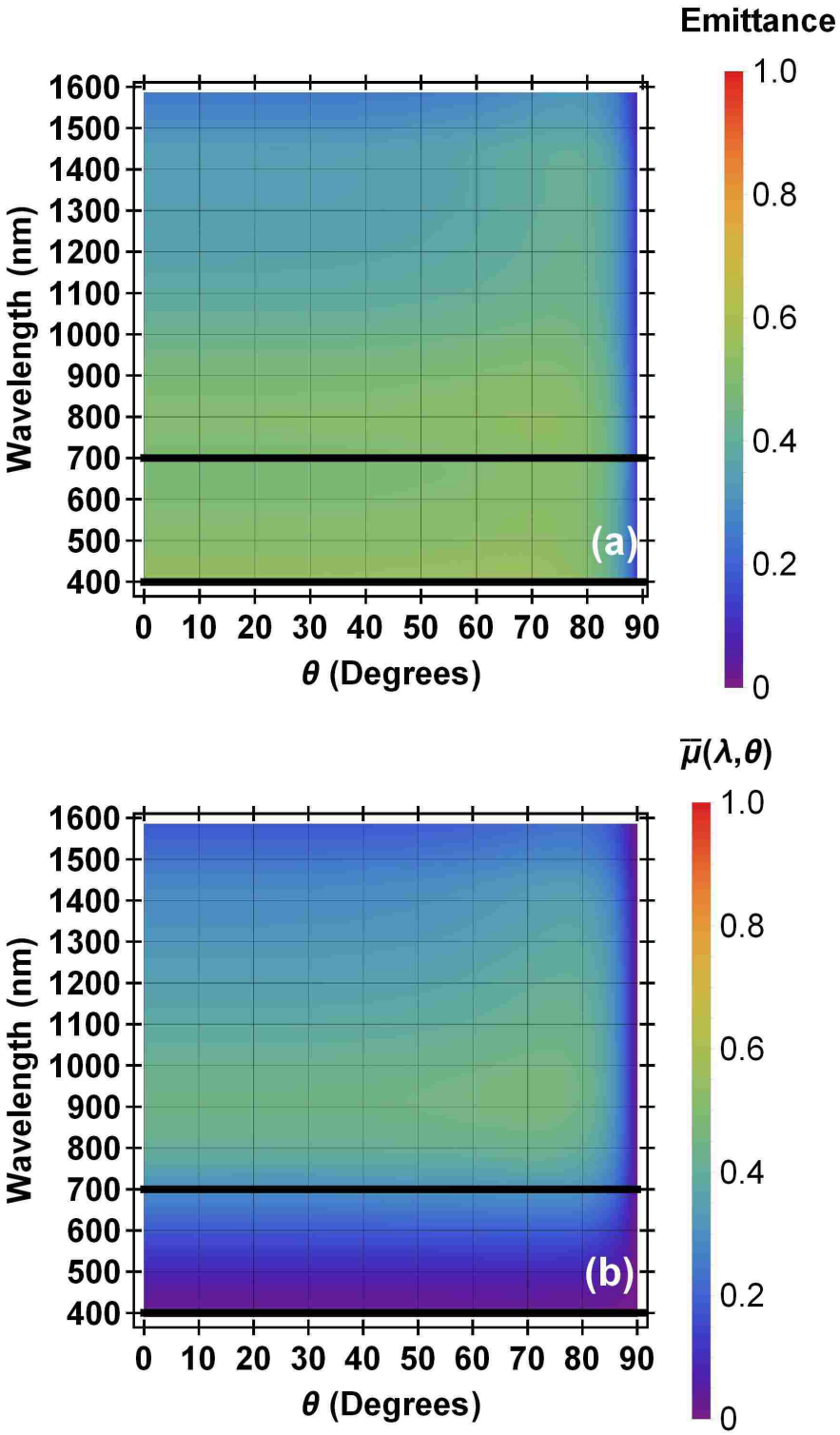

FIGURE 4.3: (a, b) Emittance and normalized power emitted per unit area and unit wavelength $\bar{\mu}(\lambda, \theta)$ of bulk tungsten as a function of wavelength and angle.The layer thicknesses of the optimized structures are given in Figure 4.2.

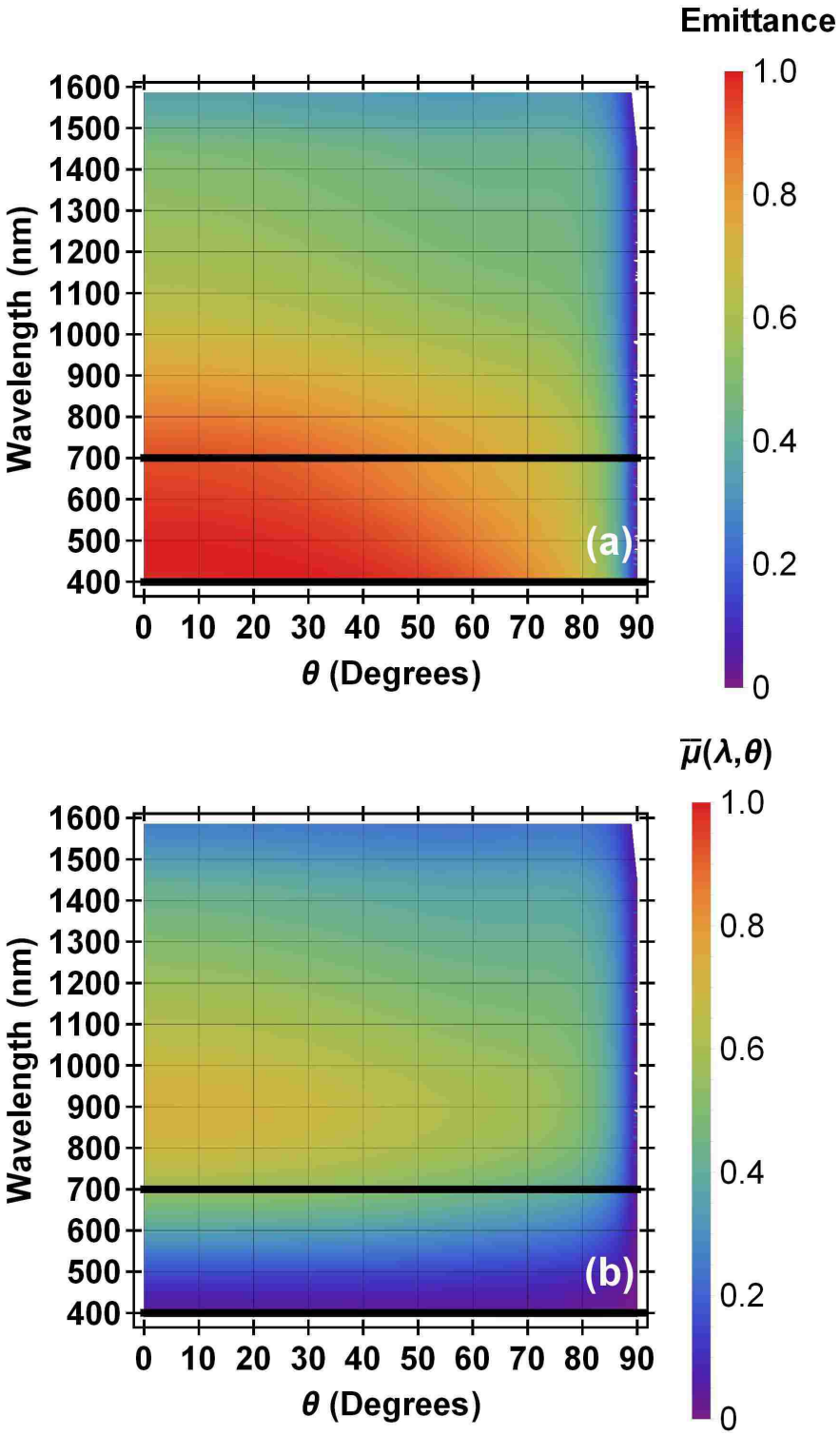

FIGURE 4.4: (a, b) Emittance and normalized power emitted per unit area and unit wavelength $\bar{\mu}(\lambda, \theta)$ for the optimized TA structure as a function of wavelength and angle. The layer thicknesses of the optimized structures are given in Figure 4.2.

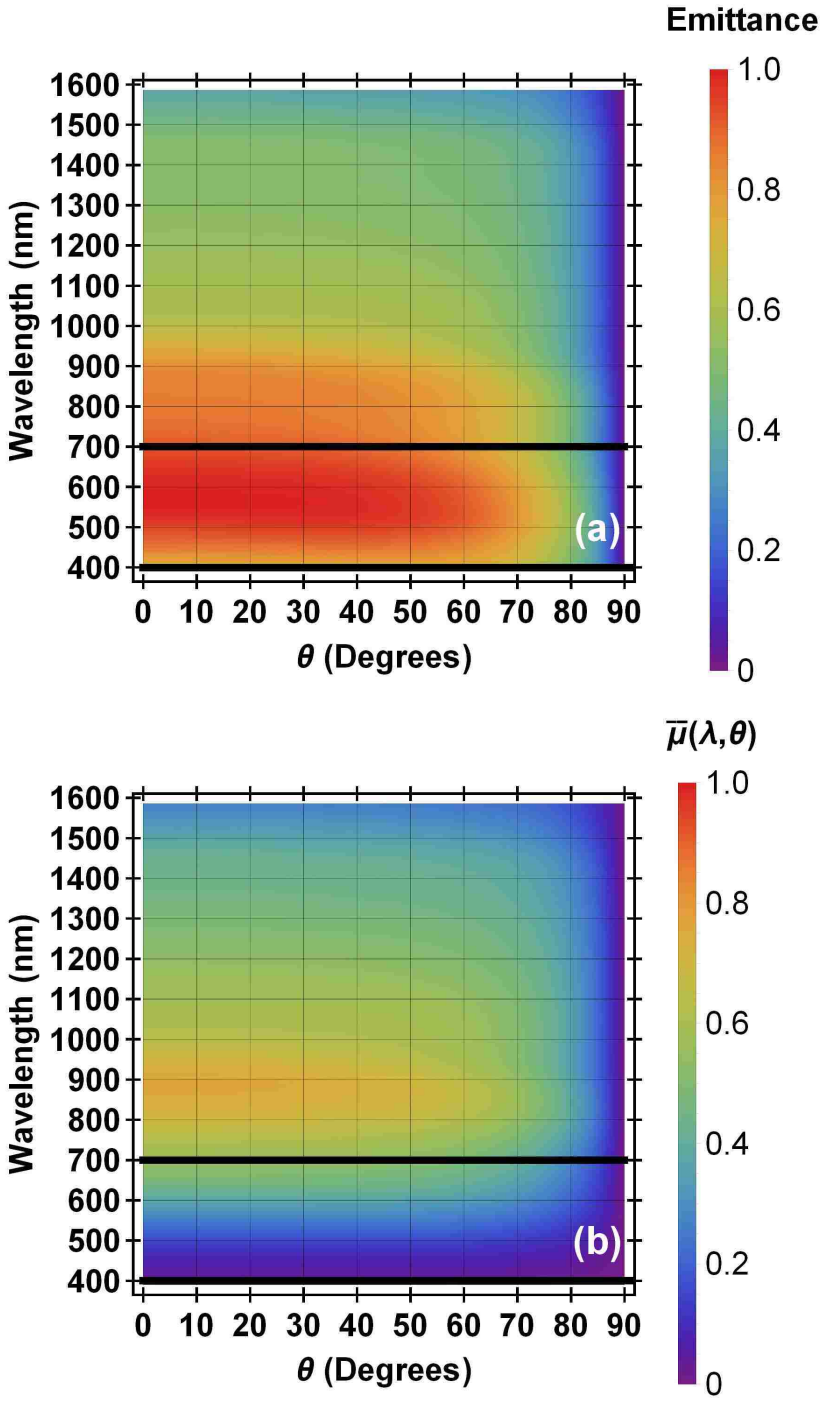

FIGURE 4.5: (a, b) Emittance and normalized power emitted per unit area and unit wavelength $\bar{\mu}(\lambda, \theta)$ for the optimized TSiC structure as a function of wavelength and angle. The layer thicknesses of the optimized structures are given in Figure 4.2.

In Figures 4.7 & 4.8, we show the profile of the electric field amplitude normalized with respect to the field amplitude of the incident plane wave for the optimized TA and TSiC

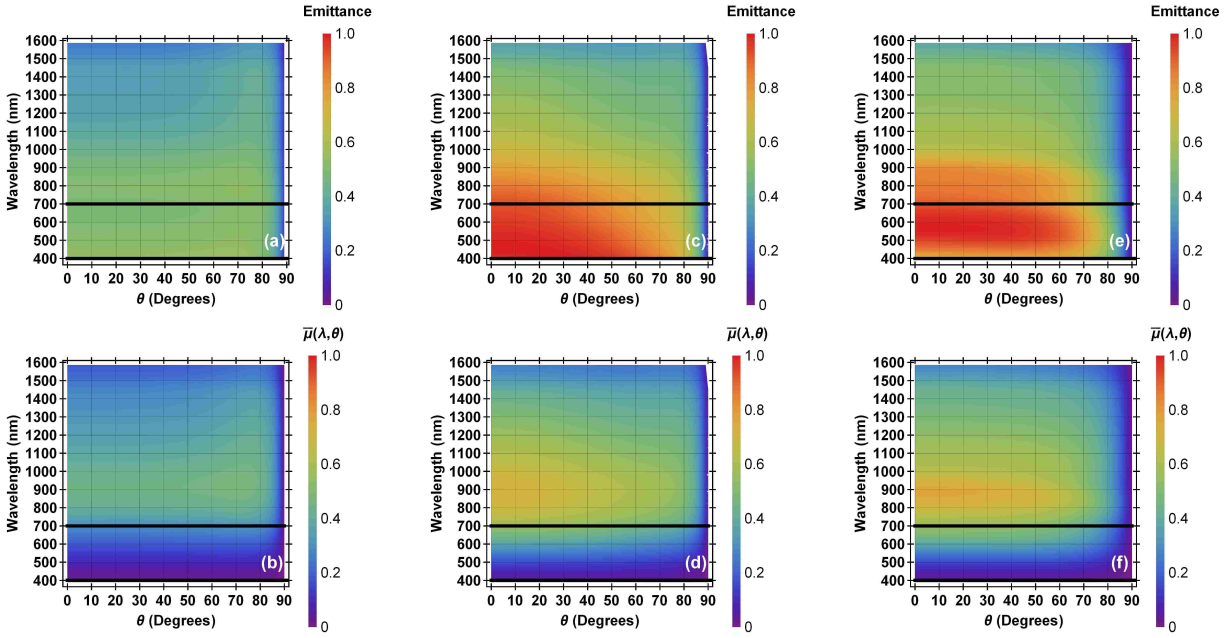

FIGURE 4.6: (a, b) Emittance and normalized power emitted per unit area and unit wavelength $\bar{\mu}(\lambda, \theta)$ of bulk tungsten as a function of wavelength and angle. (c, d) Emittance and normalized power emitted per unit area and unit wavelength $\bar{\mu}(\lambda, \theta)$ for the optimized TA structure as a function of wavelength and angle. (e, f) Emittance and normalized power emitted per unit area and unit wavelength $\bar{\mu}(\lambda, \theta)$ for the optimized TSiC structure as a function of wavelength and angle. The layer thicknesses of the optimized structures are given in Figure 4.2.

structures, respectively. Each structure is excited by a normally incident plane wave at the center of the visible spectrum, $\lambda = 550$ nm. We observe that both structures are nearly perfectly impedance-matched to air, as only $\sim 10\%$ of the incident power is reflected. In addition, there is no field enhancement in the structures. We therefore conclude that the high emittance is not associated with any strong resonances. This is consistent with the broad-angle and wideband emittance of the structures (Figure 4.6).

We found that in the optimized TA structure the 500 nm thick air layer [Figure 4.7 is not critical, since in a structure without this layer the emittance in the normal direction is smaller by no more than $\sim 0.5\%$. Thus, the optimized TA structure consists essentially of a 3.4 nm thick tungsten layer separated from the tungsten substrate by a 90 nm thick air gap. One can think of such a structure as a Fabry-Perot [77, 78] resonator as evidenced by the

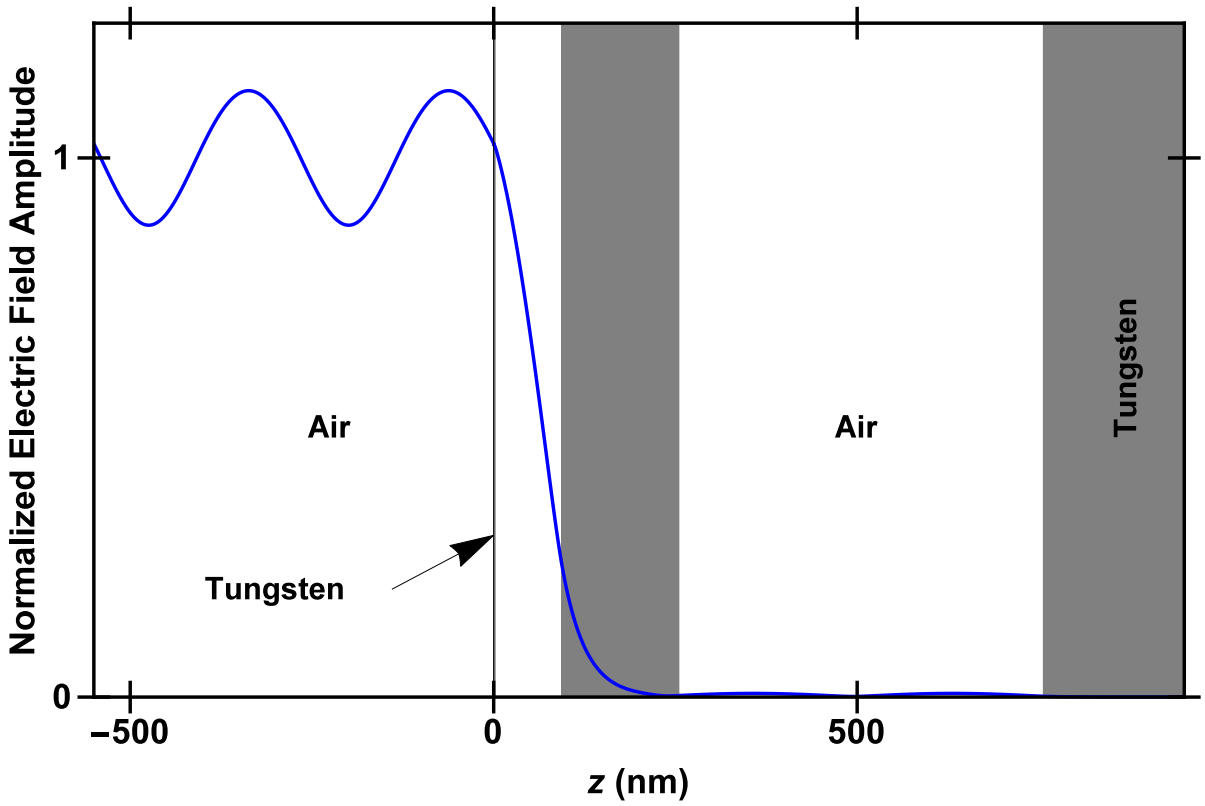

FIGURE 4.7: Profile of the electric field amplitude, normalized with respect to the field amplitude of the incident plane wave for the TA abd TSiC optimized structures described in Figure 4.2. The structures are excited by a normally incident plane wave at the wavelength of $\lambda_0 = 550$ nm, near the center of the visible wavelength range. For the TA structure, the ratio of the power absorbed inside each layer to the total power absorbed in the structure was calculated and from left to right, beginning with tungsten, is: {0.79, 0, 0.21, 0, 0}. That is, ∼79% of the power is absorbed in the first tungsten layer adjacent to air.

response of the structure's emittance to changing the width of the first two layers [Figure 4.9(a) & 4.9(b)]. Even though, as expected, the optimum air gap thickness to maximize the absorption in the 3.4 nm thick tungsten layer is wavelength dependent, we found that a structure with a 90 nm thick air gap leads to at least 73.5% absorption in the tungsten layer in the whole visible wavelength range. The mechanism which leads to broadband high emittance in the optimized TSiC structure is similar. In this case the optimized three layer structure above the tungsten substrate [Figure 4.7] leads to greatly enhanced absorption in the 66 nm thick tungsten layer in the whole visible wavelength range.

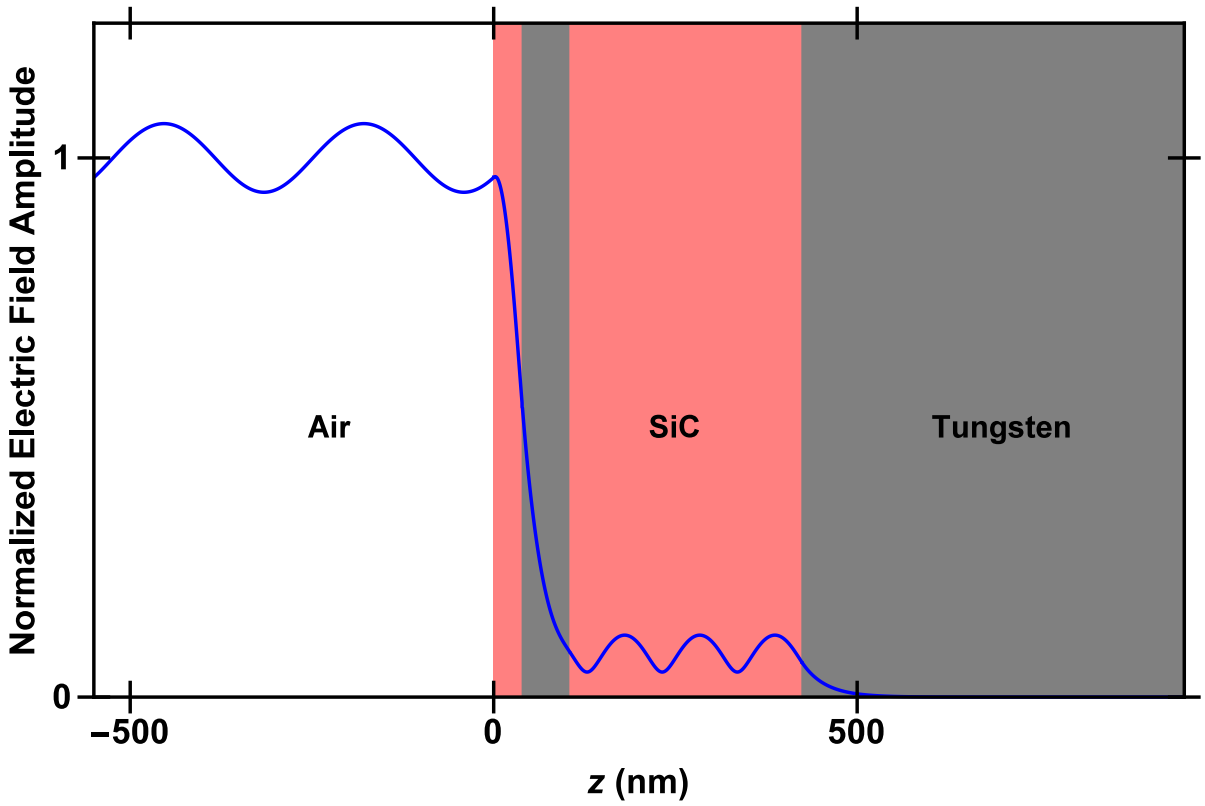

FIGURE 4.8: Profile of the electric field amplitude, normalized with respect to the field amplitude of the incident plane wave for the TA abd TSiC optimized structures described in Figure 4.2. The structures are excited by a normally incident plane wave at the wavelength of $\lambda_0 = 550$ nm, near the center of the visible wavelength range. For the TSiC aperiodic structure, the thickness of the first tungsten layer is zero; thus, the layer adjacent to air is silicon carbide. The ratio of the power absorbed inside each layer to the total power absorbed in the structure from left to right, beginning with SiC, is: {0, .99, 0, 0.01}. That is, ∼99% of the power is absorbed in the first tungsten layer

TABLE 4.2: Comparison of the wattage required to produce the same lumens as a bulk tungsten incandescent bulb as well as several common commercial bulbs [79].

Bulb Type	Watts Required	$\frac{\text{Lumens}}{\text{Watt}}$	Lumens
W Incandescent	60	15	900
Halogen	43	17.4	750
CFL Halogen	15	53	800
CFL	13	63.5	825
Smart LED	13	61.5	800
W-Air	31.1	28.9	900
W-SiC	32.4	27.8	900

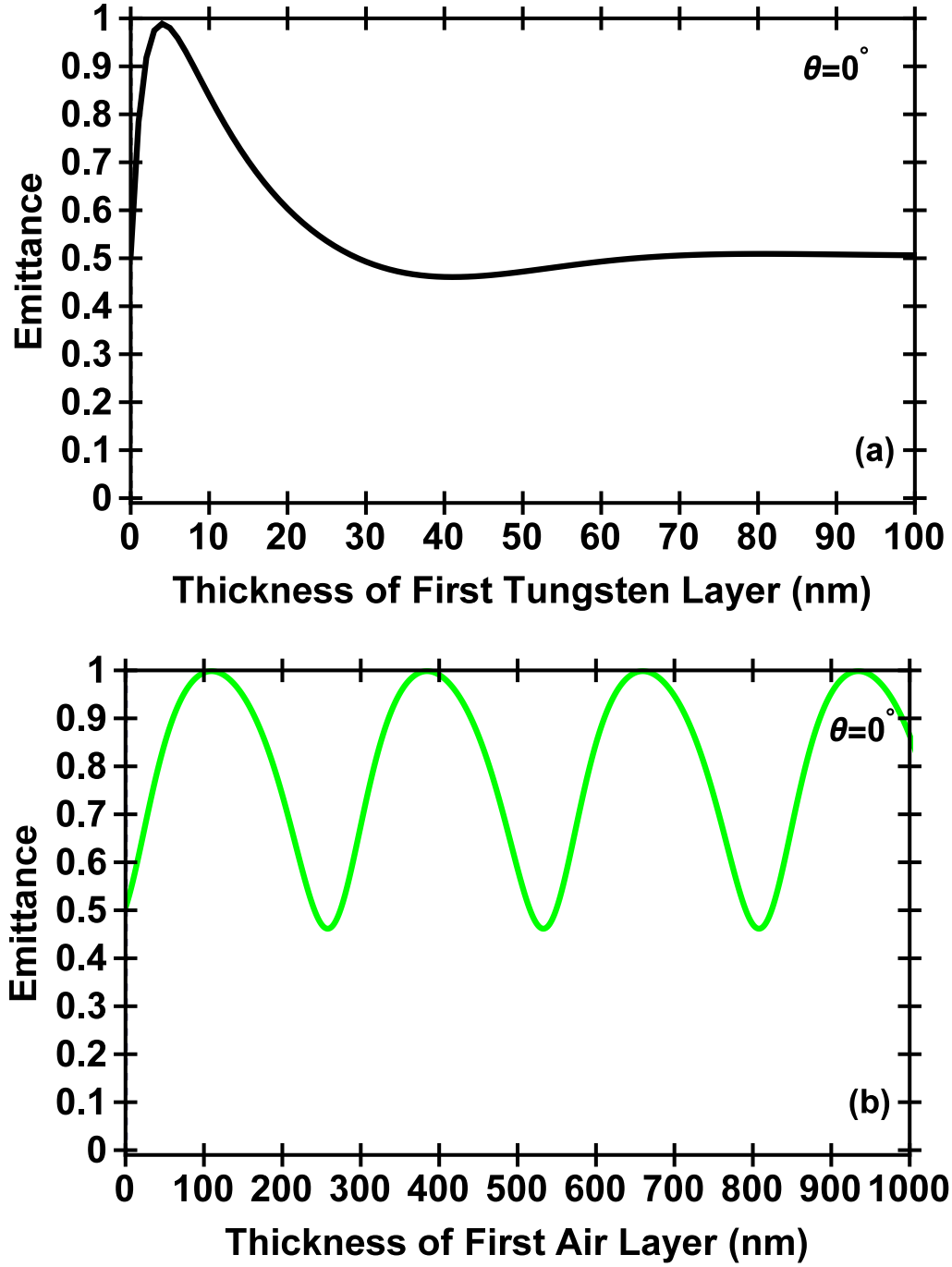

FIGURE 4.9: Here, we plot the emittance at normal incidence for $\lambda = 550$ nm of the overall optimized Tungsten-Air structure while altering individual layer thicknesses of the first and second layer. (a) Emittance of the Tungsten-Air structure as a function of thickness of the first Tungsten layer bordering air on the left hand side of the structure as shown in Figure 4.7. (b) Emittance of the Tungsten-Air structure as a function of thickness of the first Air layer inside the structure shown in Figure 4.7.

To implement our proposed lighting scheme we propose manufacturing sheets of the material inside of a transparent chamber filled with an inert gas (or evacuated) with current running through the tungsten substrate to provide the heating needed for thermal emission. To replace an incandescent light bulb we propose simply taking the usual solid tungsten filament, which is a cylinder with a ~ 5 μm diameter and coating it with the multi-layered structure proposed here. This can be done by vapor deposition or molecular beam epitaxy. Given that the layers are on the scale of nanometers, the curvature of the filament is negligible; therefore, the planar 1D calculation still holds quantitatively. To reduce evaporation effects, one might wish to reduce the surface area to volume ratio and go to 2D or 3D structures (where an air-tungsten structure is feasible to fabricate via, for example, ion etching or a modified silicon layering process) [41]. More work needs to be done to model and optimize such structures, but our results in this work indicate qualitatively, via the John-Wang model, that similar emissivity (or better) is possible. In the John-Wang model, one assumes a 3D structure that has a perfectly spherical Brillouin zone that is the same for both the TE and TM modes. In such a model the structure is effectively 1D and our results here should hold qualitatively [80, 81] .

This research was supported by the National Science Foundation (Award Nos. 1102301, 1254934, 1263236, 0968895), and a Fund for Innovation in Engineering Research (FIER) grant from the Louisiana State University College of Engineering. Jonathan P. Dowling wishes to also acknowledge support from the Air Force Office of Scientific Research and the Army Research Office.

Chapter 5
Conclusions

In Chapter 1 of this dissertation, we began with a brief introduction to nanophotonics. We provided a discussion of the theory of computational electricity and magnetism, and, specifically, calculating the absorptance and transmittance of a multilayer structure using the transfer-matrix method. We discussed the principles which motivated the design and analysis of multilayer structures. Specifically, we reviewed thermal emission, thermodynamics, Planck's blackbody distribution, Kirchoff's law, and resulting applications in solar thermophotovoltaics. In particular, a detailed discussion of the efficiency and possible implications of realizing a solar thermophotovolatic device were discussed. We also presented a brief discussion of the computer-based optimization used. Specifically, we use an in-house genetic algorithm which may be coupled to a local optimization algorithm for increased optimization of structure parameters.

Chapter 2 discussed aperiodic multilayer structures which were optimized by a genetic algorithm to provide both narrowband and narrow-angle thermal emission for selected wavelengths in the infrared wavelength range. This chapter provided a detailed comparison of the performance of aperiodic multilayer structures with the more widely researched periodic multilayer structures and analyzed the physical mechanisms which helped to achieve this emission profile via an investigation of the electromagnetic field profile. Chapter 2 also investigated the use of aperiodic multilayer structures optimized for narrow-angle and narrow band emission at the Wein Wavelength for a near-maximum operating temperature for silicon and silica. Finally, Chapter 2 discussed the application of an aperiodic genetic algorithm optimized emitter for use as a carbon monoxide detector in an absorption spectroscopy de-

vice. The work presented in this chapter could have implications in creating inexpensive, easy-to-fabricate, tunable infrared thermal emitters.

In Chapter 3, we focused on the development of aperiodic multilayer structures for use as narrow-angle absorbers utilizing a genetic optimization algorithm in the visible wavelength range. First, we examined the properties of two tungsten based emitters, one which paired tungsten with silicon and another which paired tungsten with silica. We found that structures did not provide narrow-angle absorptance profiles due to the fact that non-resonant impedance matching was the cause of these structure's high absorptance around $\lambda = 550$nm. We then examined the properties of aperiodic multilayer structures containing alternating layers of silicon and silica and found that these structures provided both a narrow angle and narrow band absorptance profile. We also investigated the properties of structures found when the genetic algorithm was allowed to choose the layer composition and found no sizable improvement over the silicon-silica structured when compared on an equal-layer basis. Finally, we showed that structures with near-perfect absorptance at two wavelengths for normally incident light can be achieved using these methods.

Chapter 4 presented optimized aperiodic structures which could be used as broadband and broad-angle thermal emitters. By using a hybrid optimization algorithm coupled to a transfer-matrix code, we maximized the power emitted in the visible wavelength range in the normal direction and then, while holding that constant, maximized the efficiency of these structures as thermal emitters in the visible wavelength range. We investigated structures consisting of alternating layers of tungsten and air and tungsten and silicon carbide, respectively. We found that both optimized structures could increase emittance in the visible wavelength range by nearly a factor of two when compared to bulk tungsten. By investigating the electromagnetic field profiles, we present the mechanisms present in these optimized structures which allow them to possess properties which could lead to a decrease in incandescent lightbulb power consumption by nearly 50%.

Bibliography

[1] S. C. Hagness A. Taflove, editor. *Computational Electrodynamics: The Finite-Difference Time-Domain Method*. Artech House, Inc, 3rd edition, 2005.

[2] J. Joannopoulos, R. Meade, and J. Winn. *Photonic Crystals: Molding the Flow of Light*. Princeton University Press, 1st edition, 1995.

[3] J. D. Jackson. *Classical Electrodynamics*. John Wiley and Sons, Inc., 3rd edition, 1999.

[4] A. Zangwill, editor. *Modern Electrodynamics*. Cambridge University Press, 1st edition, 2013.

[5] D. J. Griffiths, editor. *Introduction to Electrodynamics*. Prentice Hall, 3rd edition, 1999.

[6] D. V. Schroeder. *An Introduction to Thermal Physics*. Addison Wesley Longman, 1st edition, 2000.

[7] M. Kardar, editor. *Statistical Physics of Particles*. Cambridge University Press, 3rd edition, 2007.

[8] M. Florescu, H. Lee, I. Puscasu, M. Pralle, L. Florescu, D. Z. Ting, and J. P. Dowling. Improving solar cell efficiency using photonic band-gap materials. *Sol. Energy Mater. Sol. Cells*, 91:1599, 2007.

[9] M. Florescu, H. Lee, I. Puscasu, M. Pralle, D. Ting L. Florescu, and J. P. Dowling. Improving solar cell efficiency using photonic band-gap materials. *Sol. Energy Mater. Sol. Cells*, 91:1599, 2007.

[10] D. H. Werner R. L. Haupt, editor. *Genetic Algorithms in Electromagnetics*. Wiley-IEEE Press, 1st edition, 2007.

[11] E. Michielssen Y. Rahmat-Samii, editor. *Electromagnetic Optimization by Genetic Algorithms*. John Wiley and Sons, Inc., 1st edition, 1999.

[12] S. G. Johnson. The nlopt nonlinear-optimization package, 2008.

[13] D. E. Goldberg and K. Deb. *Fundamentals of Statistical and Thermal Physics*. Morgan Kaufmann, 1965.

[14] K. Krishnakumar. Micro-genetic algorithms for stationary and non-stationary function optimization. *Proc. SPIE*, 1196:289, 1989.

[15] K. Deb and S. Agrawal. Understanding interactions among genetic algorithm parameters. In *Fundamentals of Statistical and Thermal Physics*, pages 268–269. Morgan Kaufmann, 1999.

[16] M. J. D. Powell. A direct search optimization method that models the objective and constraint functions by linear interpolation. In S. Gomez and J. P. Hennart, editors, *Advances in Optimization and Numerical Analysis*, pages 51–67. Kluwer Academic: Dordrecht, 1994.

[17] D. E. Goldberg, K. Deb, and J. H. Clark. Genetic algorithms, noise, and the sizing of populations. *Complex Systems*, 6:333–362, 1991.

[18] J. M. Johnson and Y. Rahmat-Samii. Genetic algorithms in electromagnetics. *Proc. Int. Symp. IEEE Antennas Propagation*, 6:1480–1483, 1996.

[19] M. Ghebrebrhan, P. Bermel, Y. X. Yeng, I. Celanovic, M. Soljačić, and J. D. Joannopoulos. Tailoring thermal emission via q matching of photonic crystal resonances. *Phys. Rev. A*, 83:033810, 2011.

[20] E. Rephaeli and S. Fan. Absorber and emitter for solar thermo-photovoltaic systems to achieve efficiency exceeding the shockley-queisser limit. *Opt. Express*, 17:15145, 2009.

[21] J. J. Greffet, K. Joulain R. Carminati, S. Mainguy J. P. Mulet, and Y. Chen. Resonant transmission through a metallic film due to coupled modes. *Nature (London)*, 416:61, 2002.

[22] D. Chan, M. Soljačić, and J. D. Joannopoulos. Thermal emission and design in 2d-periodic metallic photonic crystal slabs. *Opt. Express*, 14:8785, 2006.

[23] J. G. Fleming, S. Y. Lin, I. El-Kady, R. Biswas, and K.M. Ho. All-metallic three-dimensional photonic crystals with a large infrared bandgap. *Nature (London)*, 417:52, 2002.

[24] I. Celanovic, D. Perreault, and J. Kassakian. Resonant-cavity enhanced thermal emission. *Phys. Rev. B*, 72:075127, 2005.

[25] D. L. C. Chan, M. Soljačić, and J. D. Joannopoulos. Thermal emission and design in one-dimensional periodic metallic photonic crystal slabs. *Phys. Rev. E*, 74:016609, 2006.

[26] C. Arnold, F. Marquier, F. Pardo M. Garin, S. Collin, N. Bardou, J. L. Pelouard, and J. J. Greffet. Coherent thermal infrared emission by two-dimensional silicon carbide gratings. *Phys. Rev. B*, 86:035316, 2012.

[27] M. Laroche, C. Arnold, F. Marquier, R. Carminati, J. Greffet, S. Collin, N. Bardou, and J. Pelouard. Highly directional radiation generated by a tungsten thermal source. *Opt. Lett.*, 30:2623, 2005.

[28] S. Han and D. Norris. Beaming thermal emission from hot metallic bull's eyes. *Opt. Express*, 18:4829, 2010.

[29] G. Biener, N. Dahan, A. Niv, V. Kleiner, and E. Hasman. Highly coherent theremal emission obtained by plasmonic bandgap structures. *Appl. Phys. Lett.*, 92:081913, 2008.

[30] N. Mattiucci, G. D'Aguanno, A. Alú, C. Argryopoulos, J. Foreman, and M. J. Bloemer. Taming the thermal emissivity of metals: a metamaterial approach. *Appl. Phys. Lett.*, 100:201109, 2012.

[31] E. J. Reed, M. Soljačić, and J. D. Joannopoulos. Maxwell equation simulations of coherent optical photon emission from shock waves in crystals. *Phys. Rev. E*, 75:056611, 2007.

[32] E. J. Reed, M. Soljačić, R. Gee, and J. D. Joannopoulos. Molecular dynamics simulations of coherent optical photon emission from shock waves in crystals. *Phys. Rev. B*, 75:174302, 2007.

[33] G. Liang, P. Han, and H. Wang. Narrow frequency and sharp angular defect mode in one-dimensional photonic crystals from a photonic heterostructure. *Opt. Lett.*, 29:192, 2004.

[34] C. M. Cornelius and J. P. Dowling. Modification of planck blackbody radiation by photonic band-gap structures. *Phys. Rev. A*, 59:4736, 1999.

[35] D. R. Lide. *CRC Handbook of Chemistry and Physics*. CRC Press, 2007.

[36] E. U. Condon. *Fundamentals of Statistical and Thermal Physics*. McGraw-Hill, 1965.

[37] N. Tessler, S. Burns, H. Becker, and R. H. Friend. Omnidirectional emission from top-emitting organic light-emitting devices with microstructured cavity. *Appl. Phys. Lett.*, 70:556, 1997.

[38] A. L. Smith. *The Coblentz Society Desk Book of Infrared Spectra*. The Coblentz Society, 1982.

[39] Y. X. Yeng, M. Ghebrebrhan, P. Bermel, W. R. Chan, J. D. Joannopoulos, M. Soljačić, and I. Celanovic. Enabling high-temperature nanophotonics for energy applications. *PNAS*, 109:2280, 2012.

[40] W. Wang, Y. Cui, Y. He, Y. Hao, Y. Lin, X. Tian, T. Ji, and S. He. Efficient multiband absorber based on one-dimensional periodic metal-dielectric photonic crystal with a reflective substrate. *Opt. Lett.*, 39:331, 2014.

[41] S. Y. Lin, J. Moreno, and J. G. Fleming. Three-dimensional photonic-crystal emitter for thermal photovoltaic power generation. *App. Phys. Lett*, 83:380, 2003.

[42] E. Rephaeli and S. Fan. Tungsten black absorber for solar light with wide angular operation range. *Appl. Phys. Lett.*, 92:211107, 2008.

[43] N. Mattiucci, G. D'Aguanno, A. Alù, C. Argyropoulos, J. V. Foreman, and M. J. Bloemer. Taming the thermal emissivity of metals: A metamaterial approach. *Appl. Phys. Lett.*, 100:201109, 2009.

[44] J.-J. Greffet, R. Carminati, K. Joulain, J.-P. Mulet, S. Mainguy, and Y. Chen. Coherent emission of light by thermal sources. *Nature*, 416:61, 2002.

[45] Y. X. Yeng, J. B. Chou, V. Rinnerbauer, Y. Shen, S.-G. Kim, J. D. Joannopoulos, and M. Soljacic andI. Čelanović. Global optimization of omnidirectional wavelength selective emitters/absorbers based on dielectric-filled anti-reflection coated two-dimensional metallic photonic crystals. *Opt. Express*, 22:21711, 2014.

[46] G. Veronis, R. W. Dutton, and S. Fan. Metallic photonic crystals with strong broadband absorption at optical frequencies over wide angular range. *J. Appl. Phys.*, 97:093104, 2005.

[47] G. C. R. Devarapu and S. Foteinopoulou. Mid-ir near-perfect absorption with a sic photonic crystal with angle-controlled polarization selectivity. *Opt. Express*, 20:13040, 2012.

[48] T. Søndergaard and S. I. Bozhevolnyi. Theoretical analysis of plasmonic black gold: periodic arrays of ultra-sharp grooves. *New J. Phys.*, 15:013034, 2013.

[49] J. A. Schuller, T. Taubner, and M. L. Brongersma. Optical antenna thermal emitters. *Nature Photon.*, 3:658, 2009.

[50] O. Stenzel, A. Stendal, K. Voigtsberger, and C. von Borczyskowski. Enhancement of the photovoltaic conversion efficiency of copper phthalocyanine thin film devices by incorporation of metal clusters. *Sol. Energy Mater. Sol. Cells*, 37:337, 1995.

[51] M. Westphalen, U. Kreibig, J. Rostalski, and H. Lüth andD. Meissner. Metal cluster enhanced organic solar cells. *Sol. Energy Mater. Sol. Cells*, 61:97, 2000.

[52] S. Y. Lin, J. Moreno, and J. G. Fleming. Three-dimensional photonic-crystal emitter for thermal photovoltaic power generation. *Appl. Phys. Lett.*, 83:380, 2003.

[53] S. Y. Lin, J. G. Fleming, Z. Y. Li, I. El-Kady, R. Biswas, and K. M. Ho. Origin of absorption enhancement in a tungsten, three-dimensional photonic crystal. *J. Opt. Soc. Am. B*, 20:1538, 2003.

[54] A. K. Sharma, S. H. Zaidi, P. C. Logofatu, and S. R. J. Brueck. Optical and electrical properties of nanostructured metal-silicon-metal photodetectors. *J. Opt. Soc. Am. B*, 38:1651, 2002.

[55] H. Huang, Y. Huang, X. Wang, Q. Wang, and X. Ren. Long wavelength resonant cavity photodetector based on inp/air-gap bragg reflectors. *IEEE Photonics Technol. Lett.*, 16:245, 2004.

[56] A. Tittl, P. Mai, R. Taubert, D. Dregely, N. Liu, and H. Giessen. Palladium-based plasmonic perfect absorber in the visible wavelength range and its application to hydrogen sensing. *Nano Lett.*, 11:4366, 2011.

[57] N. Liu, M. Mesch, T. Weiss, M. Hentschel, and H. Giessen. Infrared perfect absorber and its application as plasmonic sensor. *Nano Lett.*, 10:2342, 2010.

[58] M. Diem, T. Koschny, and C. M. Soukoulis. Wide-angle perfect absorber/thermal emitter in the terahertz regime. *Phys. Rev. B*, 79:033101, 2009.

[59] J. Hendrickson, J. Guo, B. Zhang, W. Buchwald, and R. Soref. Wideband perfect light absorber at midwave infrared using multiplexed metal structures. *Opt. Lett.*, 37:371, 2012.

[60] C. Hu, Z. Zhao, X. Chen, and X. Luo. Realizing near-perfect absorption at visible frequencies. *Opt. Express*, 17:11039, 2009.

[61] T. V. Teperik, F. J. Garcia de Abajo, A. G. Borisov, M. Abdelsalam, P. N. Bartlett, Y. Sugawara, and J. J. Baumberg. Omnidirectional absorption in nanostructured metal surfaces. *Opt. Express*, 2:299, 2008.

[62] K. Aydin, V. E. Ferry, R. M. Briggs, and H. A. Atwater. Broadband polarization-independent resonant light absorption using ultrathin plasmonic super absorbers. *Nat. Commun.*, 2:517, 2011.

[63] M. K. Hedayati, M. Javaherirahim, B. Mozooni, R. Abdelaziz, A. Tavassolizadeh, V. S. K. Chakravadhanula, V. Zaporojtchenko, T. Strunkus, F. Faupel, and M. Elbahri. Design of a perfect black absorber at visible frequencies using plasmonic metamaterials. *Adv. Mater.*, 23:5410, 2011.

[64] Y. Cui, K. H. Fung, H. Ma J. Xu, Y. Jin, S. He, and N. X. Fang. Ultrabroadband light absorption by a sawtooth anisotropic metamaterial slab. *Nano Lett.*, 12:1443, 2012.

[65] T. Søndergaard, S. M. Novikov, T. Holmgaard, R. L. Eriksen, J. Beermann, Z. Han, K. Pedersen, and S. I. Bozhevolnyi. Plasmonic black gold by adiabatic nanofocusing and absorption of light in ultra-sharp convex grooves. *Nat. Commun.*, 3:969, 2012.

[66] G. C. R. Devarapu and S. Foteinopoulou. Broadband mid-ir superabsorption with aperiodic polaritonic photonic crystals. *J. Europ. Opt. Soc. Rap. Public.*, 9:14012, 2014.

[67] C. Argyropoulos, K. Q. Le, G. D'Aguanno N. Mattiucci and, and A. Alù. Broadband absorbers and selective emitters based on plasmonic brewster metasurfaces. *Phys. Rev. B*, 87:205112, 2013.

[68] Y. Shen, D. Ye, Z. Wang, L. Wang, I. Čelanović, L. Ran, J. D. Joannopoulos, and M. Soljačić. Metamaterial broadband angular selectivity. *Phys. Rev. B*, 90:125422, 2014.

[69] P. Bermel, M. Ghebrebrhan, M. Harradon, Y. X. Yeng, I. Čelanović, J. D. Joannopoulos, and M. Soljačić. Tailoring photonic metamaterial resonances for thermal radiation. *Nanoscale Res. Lett.*, 6:549, 2011.

[70] Y. Shen, D. Ye, I. Celanovic, S. G. Johnson, J. D. Joannopoulos, and M. Soljačić. Optical broadband angular selectivity. *Science*, 343:1499, 2014.

[71] C. H. Granier, F. O. Afzal, C. Min, J. P. Dowling, and G. Veronis. Optimized aperiodic highly directional narrowband infrared emitters. *J. Opt. Soc. Am. B*, 31:1316, 2014.

[72] D. E. Goldberg, K. Deb, and J. H. Clark. Genetic algorithms, noise, and the sizing of populations. *Complex Systems*, 6:333–362, 1991.

[73] J. Toedt, D. Koza, and K. V. Cleef-Toedt. *Chemical Composition of Everyday Products*. Greenwood Press, 2005.

[74] J. M. Berd. *Environmental Chemistry in Society*. CRC Press, 2nd edition, 2014.

[75] L. A. Bloomfield. *How Things Work: The Physics of Everyday Life*. John Wiley & Sons, Inc., 4 edition, 2009.

[76] C. H. Granier, F. O. Afzal, Jr. S. G. Lorenzo an M. Reyes, J. P. Dowling, and G. Veronis. Optimized aperiodic multilayer structures for use as narrow-angular absorbers. *J. Appl. Phys*, 116:243101, 2014.

[77] A. Yariv and P. Yeh, editors. *Photonics: Optical Electronics in Modern Communications*. Oxford University Press, 6th edition, 2007.

[78] B. E. A. Saleh and M. C. Teich, editors. *Fundamentals of Photonics*. John Wiley and Sons, Inc., 1st edition, 1991.

[79] General Electric. Find the right general electric light bulbs, 2015.

[80] S. John and J. Wang. Quantum electrodynamics near a photonic band gap: Photon bound states and dressed atoms. *Phys. Rev. Lett.*, 64:2418, 1990.

[81] S. John and J. Wang. Quantum optics of localized light in a photonic band gap. *Phys. Rev. B*, 43:12772, 1991.

Appendix: Permission to Use Publications

The following are the copyright policies of the Journal of Optical Society of America B and American Institute of Physics (AIP) from:

- https://www.osapublishing.org/josab/submit/review/copyright_permissions.cfm#posting

Author Posting Policy: Transfer of copyright does not prevent an author from subsequently reproducing his or her article. OSA's Copyright Transfer Agreement gives authors the right to publish the Author Accepted version of the article or chapter in a compilation of the author's own works or reproduce the article for teaching purposes on a short-term basis.

- http://publishing.aip.org/authors/copyright-reuse

Q: May I include my AIP article in my thesis or dissertation?

AIP permits authors to include their published articles in a thesis or dissertation. It is understood that the thesis or dissertation may be published in print and/or electronic form and offered for sale, as well as included in a university's repository. Formal permission from AIP is not needed. If the university requires written permission, however, we are happy to supply it.

Vita

Christopher H. Granier was born in 1987 in Baton Rouge, Louisiana. He majored in physics with a mathematics minor at Louisiana State University and graduated in May, 2010. He continued his education by entering graduate school at LSU in June 2010 and received his Masters of Science in Physics in May 2014. He is currently a candidate for the degree of Doctor of Philosophy in Physics, which is to be awarded in August, 2015.